

**Investigation of the relationship between solar radiation and cloud cover using a Total  
Sky Imager**

by

**Elison Soul Ganya**

**Submitted in fulfilment of the academic requirements for the degree of**

**Master of Science in the School of Chemistry and Physics,**

**University of KwaZulu-Natal, Durban**

**March 2017**



# Abstract

Solar radiometric studies have been done in South Africa, but no research studies have been performed to understand how the cloud fraction ( $CF$ ) affects the amount of solar radiation received by radiometers. This work focused on studying the relationship between radiometry readings and cloud fraction at the University of Kwa-Zulu Natal (UKZN) at Howard College in Durban. This study used a pyrhelimeter to measure beam irradiance ( $DNI$ ), a shaded pyranometer to measure diffuse irradiance ( $DHI$ ), an unshaded pyranometer to measure global irradiance ( $GHI$ ) and a Total Sky Imager to give  $CF$  percentage. When we studied 1-minute data of radiometric profiles versus  $CF$  with respect to time, we found that an increase in  $CF$  resulted in a decrease in  $DNI$  except for the rare moments when the clouds did not obstruct the sun. An increase in  $CF$  resulted in an increase in  $DHI$  only if the sky was not overcast. For an overcast sky, there is no simple relationship between  $CF$  and  $DHI$ . When we studied centred moving averages of  $DNI$  against clearness fraction ( $1 - CF$ ) as a function of time for different time-averaging scales, it was found that  $DNI$  had strong linear correlation with  $1 - CF$ . When we studied centred moving averages of  $DHI$  and  $CF$  as a function of time for different averaging scales, it was found that  $DHI$  increased as  $CF$  increased but only if the sky was not overcast. Scatter plots of different clearness indices against  $CF$  for different averaging scales were studied and it was found that linear correlation increased with averaging scale, and beam-related clearness indices had a strong linear relationship with  $CF$  at a time-averaging scale of 4 hours.

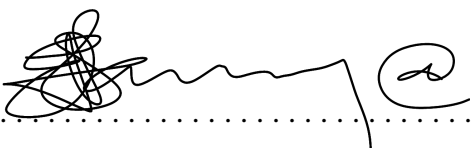
# Preface

The experimental work described in this dissertation was carried out in the School of Chemistry and Physics, University of KwaZulu-Natal, Westville, Durban, from January 2013 to April 2015, under the supervision of Dr. A.P. Matthews and Professor Sivakumar Venkataraman. These studies represent original work by the author and have not otherwise been submitted in any form for any degree or diploma to any tertiary institution. Where use has been made of the work of others, it is duly acknowledged in the text.

# Declaration-Plagiarism

I, Elison S. Ganya declare that

1. The research reported in this thesis, except where otherwise indicated, is my original research.
2. This thesis has not been submitted for any degree or examination at any other university.
3. This thesis does not contain other persons' data, pictures, graphs or other information, unless specifically acknowledged as being sourced from other persons.
4. This thesis does not contain other persons' writing, unless specifically acknowledged as being sourced from other researchers. Where other written sources have been quoted, then:
  - (a) Their words have been re-written but the general information attributed to them has been referenced.
  - (b) Where their exact words have been used, then their writing has been placed in italics and inside quotation marks, and referenced.
5. This thesis does not contain text, graphics or tables copied and pasted from the Internet, unless specifically acknowledged, and the source being detailed in the thesis and in the Bibliography section.

Signed: 

# Acknowledgements

Firstly, I would like to thank my supervisor Dr A.P Matthews for his unwavering support, motivation and kind supervision during the entire period of my research. You so understood and were patient with me. I would like to thank my co-supervisor Professor Sivakumar Venkataraman for his advice during the course of this research project.

I am also indebted to thank the Principal Technician, Enock Chekure for his support and assistance throughout the entire period of my research. I am grateful for your help and patience when dealing with my requests. Special thanks to my colleague Paulene Govender for her assistance, advice and unwavering support in making this project successful.

To the staff at Howard College, Mike Brooks and his team, I would like to thank you for your assistance in maintaining the radiometry and TSI equipment.

Great thanks to my friend Dr Mhlambululi Mafu for his support and guidance during the course of this research project.

Lastly, I would like to thank my wife and family for all their encouragement and unconditional support.

# Table of Contents

Abstract.....	ii
Preface.....	iii
Declaration-Plagiarism .....	iv
Acknowledgements.....	v
List of Figures .....	ix
List of Tables .....	xiii
Chapter 1.....	1
Introduction.....	1
1.1    Research aim .....	5
1.2    Research question.....	5
1.3    Brief history of Sky Imagers (SIs) .....	5
1.4    Literature review .....	6
1.5    Summary of chapters.....	21
Chapter 2.....	22
Solar Radiation.....	22
2.1    Interaction of solar radiation with the atmosphere.....	23
2.2    Sun-Earth geometry.....	33
Chapter 3.....	37
Solar radiometry instruments and the Total Sky Imager .....	37
3.1    Pyrheliometers.....	38
3.1.1    Kipp and Zonen Normal Incidence Pyrheliometer (NIP) .....	42
3.2    Pyranometers .....	43
3.2.1    Kipp and Zonen shaded and unshaded pyranometers.....	46
3.3    Sky Imagers (SI's).....	47
3.3.1    Total Sky Imager.....	49

3.3.2	TSI-440A Total Sky Imager .....	54
Chapter 4	.....	60
Methods and Data Quality	.....	60
4.1	Experimental set-up.....	60
4.2	Data acquisition.....	61
4.3	Data collected and how it will be analysed .....	62
Chapter 5	.....	69
Results	.....	69
5.1	Radiometric profiles and TSI images to show cloud fraction $CF$ .....	69
	Results for 14 <sup>th</sup> July 2014.....	69
5.2	Statistical Results .....	89
5.2.1	Linear regression plots for 1 minute data. ....	89
5.2.2	Linear regression plots for 15 minutes-averaging data.....	94
5.2.3	Linear regression plots for 1 hour-averaging data. ....	99
5.2.4	Linear regression plots for 4 hours-averaging data.....	105
Chapter 6	.....	111
Discussion of Results	.....	111
6.1	Radiometric profiles and TSI images to show cloud fraction $CF$ .....	111
6.2	Centred moving average $DNI$ and $I - CF$ vs $t$ for different time-averaging time-scales $\tau$ 10 September 2014.....	113
6.3	Centred moving average $DHI$ and $CF$ vs $t$ for different time-averaging time-scales $\tau$ 10 September 2014.....	113
6.4	Linear regression plots for 1 minute data.....	114
6.5	Linear regression plots for 15 minutes, 1 hour and 4 hours average data.....	114
Chapter 7	.....	116
Conclusion and recommendations	.....	116
7.1	Conclusion.....	116

7.2 Considerations for future work .....	117
Appendix A.....	128
Nomenclature.....	128
Appendix B.....	129
SAURAN Station Details: KZH University of KwaZulu-Natal, Howard College Campus, Durban, South Africa.....	129
Appendix C.....	132
Matlab code for averaging .....	132
Appendix D.....	133
Extra graphs of plots not used in the main text.....	133

# List of Figures

Figure 1.1: Average daily <i>DNI</i> for South Africa for the entire year .....	3
Figure 2.1: Structure of the sun .....	22
Figure 2.2: The atmosphere affects the amount and distribution of solar radiation reaching the ground .....	24
Figure 2.3: Interaction of incoming Solar Radiation with the atmosphere and ground .....	25
Figure 2.4: Sketches of the angular pattern of the scattered intensity from particles of various sizes .....	27
Figure 2.5: AM: Air Mass index .....	28
Figure 2.6: Scattering of the direct-beam photons from the sun by the atmosphere produces diffuse radiation that varies with AM .....	29
Figure 2.7: Radiation balance of the atmosphere .....	30
Figure 2.8: Scattering of the direct-beam photons from the sun by the atmosphere .....	31
Figure 2.9: Position of the equinoxes, solstices, aphelion, and perihelion relative to the Earth's orbit around the Sun .....	34
Figure 3.1: Angström pyrheliometer (a) external view, (b) schematic of the instrument, ( $G_1$ ) and ( $G_2$ ) galvanometers, (R) rheostat regulating the strength of the compensation current ...	39
Figure 3.2: Silver-disk pyrheliometer .....	40
Figure 3.3: Cross section of the Eppley NIP .....	41
Figure 3.4: Pyrheliometer mounted onto the Solys 2 tracker measures the <i>DNI</i> component..	43
Figure 3.5: Thermo-electric pyranometer .....	44
Figure 3.6: Bimetallic pyranograph .....	45
Figure 3.7: Shaded and unshaded pyranometers mounted on a stationary plate on top of the Solys 2 tracker.....	46
Figure 3.8: Clear-Sky Image (left end), Corresponding Relative Red/Blue Ratio Image, (second from left end), Separated Blue (second from right end), and Red (right end) Pixel Value Amount Images. ....	51
Figure 3.9: Cloud Detection Image Corresponding to Fig 3.3. Black denotes masking. Green outlines denote areas where separate cloud/clear pixel counts are included in the sky cover	

retrieval output files. Cloud detection color scheme is clear (blue), thin cloud (gray) and opaque cloud (white) .....	52
Figure 3.10: Cloudy-Sky Image (left end), Corresponding Relative Red/Blue Ratio Image (second from left end), Separated Blue (second from right end), and Separated Red (right end) Pixel Value Amount Images .....	53
Figure 3.11: Cloud Detection Image Corresponding to Fig 3.5. Black denotes masking. Green outlines denote areas where separate cloud/clear pixel counts are included in the sky cover retrieval output files. Cloud detection color scheme is clear (blue), thin cloud (gray) and opaque cloud (white) .....	53
Figure 3.12: Model TSI-440 Total Sky Imager as mounted on Desmond Clarence Building, at UKZN Howard College Campus, Durban. ....	55
Figure 3.13: Processed image (left) and Raw sky image (right) at time 10:52 on the 01 <sup>st</sup> of October 2014.....	56
Figure 3.14: Processed image (left) and Raw sky image (right) at 11:45 on 14 <sup>th</sup> of July 2014. The <i>CF</i> was 41% and the sky condition was sunny.....	57
Figure 4.1: Instrument setup at the test site of the radiometric instruments (pyrheliometer and shaded and unshaded pyranometers) and TSI connected to CR1000 data logger. ....	61
Figure 4.2: Plot of diffuse fraction $k_d$ against clearness index $k_t$ for 1-minute data at Eugene . ....	63
Figure 4.3: Graph of the $k_d$ against clearness index $k_t$ for 1-minute data of the entire dataset. ....	64
Figure 4.4: Plot of $k_b$ versus $k_t$ for 1-minute data at Eugene .....	65
Figure 4.5: Graph of $k_b$ vs $k_t$ for 1-minute data of the entire data.....	65
Figure 4.6: Graph of clear sky and actual radiometric readings for 04 December 2014. ....	67
Figure 5.1: Raw sky image (a) and processed image (b) at 11:09 on 14 <sup>th</sup> of July 2014. The <i>CF</i> was 4% and the sun was not obstructed by clouds. ....	70
Figure 5.2: Plot of <i>CF</i> and solar irradiance against time between 06:00 and 18:00 on 14 <sup>th</sup> of July 2014.....	70
Figure 5.3: Raw TSI image (a) and processed TSI image (b) at 11:45 on 14 <sup>th</sup> of July 2014. The <i>CF</i> was 41% and the sun was not obstructed.....	71
Figure 5.4: Raw sky image (a) Processed image (b) and at 12:00 on 27 <sup>th</sup> of January 2015. The <i>CF</i> was 100% and the sun was obstructed by clouds. ....	72
Figure 5.5: Plot of <i>CF</i> and solar irradiance against time between 06:00 and 18:00 on 27 <sup>th</sup> of January 2015. ....	73

Figure 5.6: Raw sky image (a) and processed image (b) at 13:03. The $CF$ was 100% and the sky condition was not sunny. ....	74
Figure 5.7: Raw sky image (a) Processed image (b) and at 11:38 on 30 <sup>th</sup> of January 2015. The $CF$ was 53% and the sun was obstructed by clouds. ....	75
Figure 5.8: Plot of $CF$ and solar irradiance against time between 06:00 and 18:00 on 30 <sup>th</sup> of January 2015. ....	76
Figure 5.9: Plot of $CF$ and solar irradiance against time between 06:00 and 18:00 on 30 <sup>th</sup> of January 2015. ....	76
Figure 5.10: Raw sky image (a) and processed image (b) at 08:25. The $CF$ was 98% and the sky condition was sunny. ....	77
Figure 5.11: Plot of $CF$ and solar irradiance against time between 11:00 and 13:00 on 30 <sup>th</sup> of January 2015. ....	78
Figure 5.12: Raw sky image (a) and processed image (b) and at 08:25. The $CF$ was 71% and the sky condition was sunny. ....	79
Figure 5.13: Raw TSI image at (a) 10:00 (b) 11:00 and (c) 12:00. Processed TSI image at (d) 10:00 (e) 11:00 and (f) 12:00. ....	79
Figure 5.14: Plot of $CF$ and solar irradiance against time between 06:00 and 18:00 on 10 <sup>th</sup> of September 2014. ....	80
Figure 5.15: Plot of $CF$ and solar irradiance against time between 10:00 and 12:00 on 10 <sup>th</sup> of September 2014. ....	81
Figure 5.16: Processed 1-minute images between 10:16 to 10:30 (from left to right on the top row and down row also from left to right). The $CF$ increased from 71% at 10:16 to 100% at 10:30. The temporal variation of images shows cloud evaluation from South East direction. ....	82
Figure 5.17: Raw sky image (a) and processed image (b) at 11:56. The $CF$ was 97% and the sun was not obstructed. ....	83
Figure 5.18: Plot of centred moving average $DNI$ and $I - CF$ against time for different time-averaging time-scales $\tau$ ....	86
Figure 5.19: Plot of centred moving average $DHI$ and $CF$ against time for different time-averaging time-scales $\tau$ ....	88
Figure 5.20: Scatter plot of $k_t$ as a function of the total $CF$ for the entire 1 minute dataset. ....	90
Figure 5.21: Scatter plot of $k_c$ as a function of the total $CF$ for the entire 1 minute dataset. ....	91
Figure 5.22: Scatter plot of $k_b$ against $CF$ for the entire 1 minute dataset. ....	92
Figure 5.23: Scatter plot of $DNI/DNI_c$ as a function of the total $CF$ for the entire 1 minute dataset. ....	93

Figure 5.24: Scatter plot $DHI/DHI_c$ as a function of the total $CF$ for the entire 1 minute dataset. ....	94
Figure 5.25: Scatter plot of $k_t$ as a function of the total $CF$ for the entire dataset. ....	95
Figure 5.26: Scatter plot of $k_c$ as a function of the total $CF$ for the entire dataset.....	96
Figure 5.27: Scatter plot of $k_b$ as a function of the total $CF$ for the entire dataset.....	97
Figure 5.28: Scatter plot of $DNI/DNI_c$ as a function of the total $CF$ for the entire dataset.....	98
Figure 5.29: Scatter plot of $DHI/DHI_c$ as a function of the total $CF$ for the entire dataset. ....	99
Figure 5.30: Scatter plot of $k_t$ as a function of the total $CF$ for the entire dataset. ....	100
Figure 5.31: Scatter plot of $k_c$ as a function of the total $CF$ for the entire dataset.....	101
Figure 5.32: Scatter plot of $k_b$ as a function of the total $CF$ for the entire dataset.....	102
Figure 5.33: Scatter plot of $DNI/DNI_c$ as a function of the total $CF$ for the entire dataset....	103
Figure 5.34: Scatter plot of $DHI/DHI_c$ as a function of the total $CF$ for the entire dataset. ..	104
Figure 5.35: Scatter plot of $k_t$ as a function of the total $CF$ for the entire dataset. ....	105
Figure 5.36: Scatter plot of $k_c$ as a function of the total $CF$ for the entire dataset.....	106
Figure 5.37: Scatter plot of $k_b$ as a function of the total $CF$ for the entire dataset.....	107
Figure 5.38: Scatter plot of $DNI/DNI_c$ as a function of the total $CF$ for the entire dataset....	108
Figure 5.39: Scatter plots of $DHI/DHI_c$ as a function of the total $CF$ for the entire dataset..	109
Figure B.1: KZH station details. ....	131
Figure D.1: Scatter plots for 30 minutes average .....	133
Figure D.2: Scatter plots for 2 hours average .....	134
Figure D.3: Scatter plots for 3 hour average.....	135

# List of Tables

Table 2.1: The day $N$ corresponding to the $i$ -th day of the month.....	35
Table 6.1: Correlation coefficient and coefficient of determination for clearness indices against $CF$ .....	115
Table A.1: Nomenclature.....	128

# Chapter 1

## Introduction

The world still depends much on the carbon sources of energy which are having negative environmental impact such as global warming. The burning of fossil fuels emits greenhouse gases such as CO<sub>2</sub> and methane (CH<sub>4</sub>) which absorb long-wave solar radiation, preventing it from leaving the earth's atmosphere and entering into space. This results in excess thermal energy being trapped in the atmosphere because the greenhouse gases emit the absorbed long-wave radiation raising the temperature of the earth. This process is known as global warming (Kalogirou, 2004). In order to reduce the effects of global warming, there must be a decrease in the pollution created by power plants and automobiles that involve burning of fossil fuels and more environmentally friendly energy alternatives have to be utilised. Apart from the negative environmental impact, the rate at which the carbon sources are depleted is of great concern since it is not renewable. This gave birth to the idea of utilising free renewable energy sources. Environmentally friendly energy sources include solar, wind, hydro, biofuel and geothermal.

Solar energy stands out as the most abundant energy resource on Earth. However, harnessing this form of energy optimally is still a challenge. Solar energy is used in photovoltaics (PV) and solar thermal system (STS) which are concentrating or non-concentrating. These two are primary forms of electricity generation. Sunlight is the fuel for all PV's and STS's generation technologies. The performance of the PV's and STS's at any place depends on the available insolation as well as other meteorological parameters. Insolation is the measure of solar radiation that is received at a specific location and time, commonly expressed as average irradiance in W/m<sup>2</sup> (Rudd, 2011). Proper understanding and thorough knowledge of the available insolation reaching a site is important for accurate analysis of system performance and financial viability of a project on a site ( Stoffel, et al., 2010).

South Africa has an average annual Direct Normal Irradiation (*DNI*) of more than 2500 kWh/m<sup>2</sup> which fortunately makes it one of the best solar resourced countries in the world (Edkins, Winkler, & Marquard, 2009). Direct Normal Irradiance (*DNI*) is the amount of solar radiation received per unit area by a surface that is always held perpendicular (or normal) to the rays that come in a straight line from the direction of the sun at its current position in the sky (solargis). The high average *DNI* for South Africa make it an ideal location for implementing solar powered technologies. Fig 1.1 illustrates the *DNI* distribution for South Africa. KwaZulu-Natal province is one of the areas with the lowest annual average *DNI* of less than 6.0 kWh/m<sup>2</sup>/d. The Northern Cape has the highest *DNI* of more than 7.0 kWh/m<sup>2</sup>/d, which make it an appropriate location for implementing concentrated solar power (CSP) technologies (Fluri, 2009).

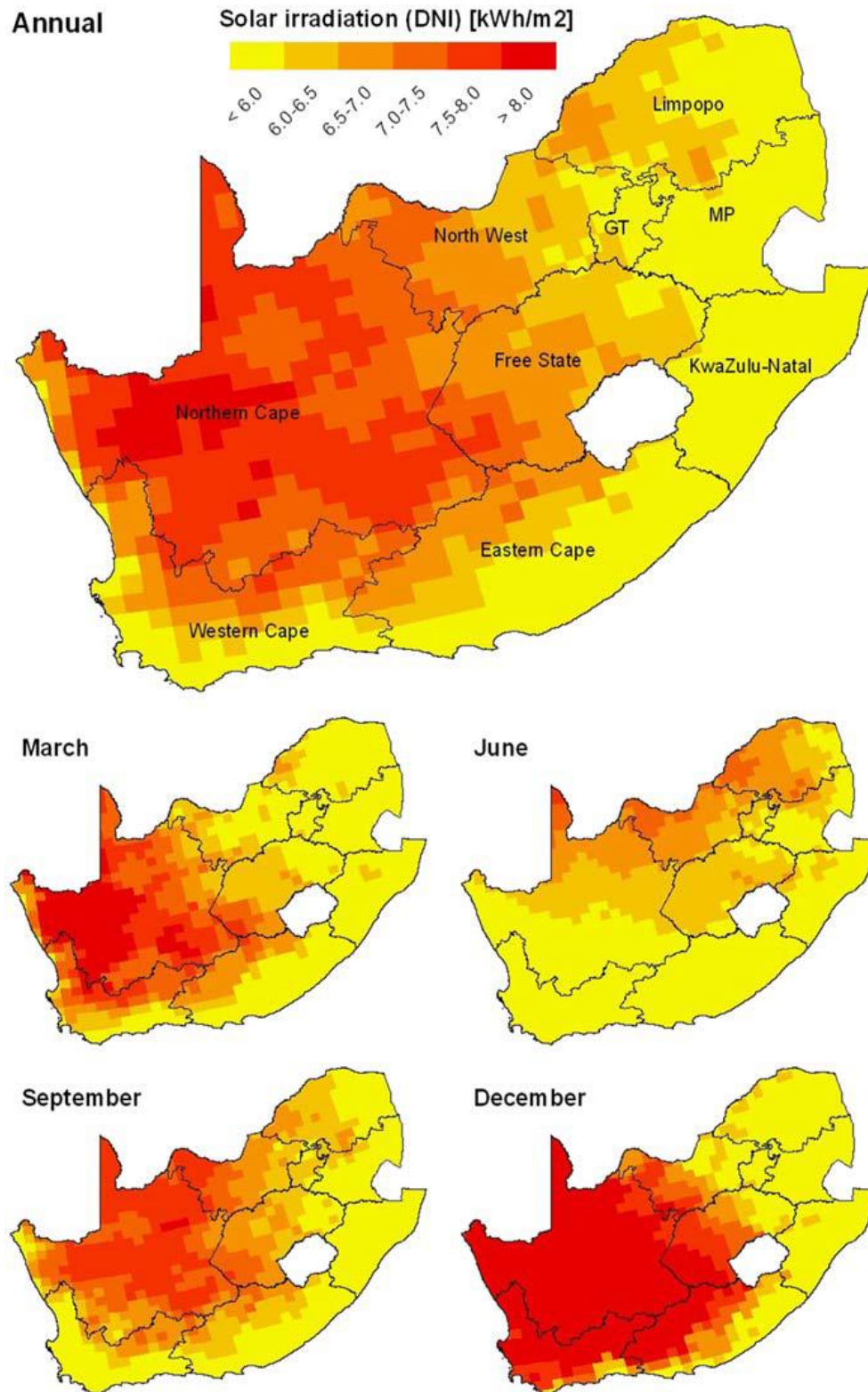


Figure 1.1: Average daily DNI for South Africa for the entire year (Fluri, 2009).

Clouds have an effect on the radiation received at the earth's surface and this knowledge is vital for a radiative energy budget. Amongst other factors, clouds are the primary source of solar radiation fluctuation (Peng, Yoo, Yu, Huang, Kalb, & Heiser, 2014). Clouds are believed to reduce the available received radiation on the ground especially under overcast conditions (Josefsson & Landelius, 2000) (Renaud, Staehelin, Fröhlich, Philipona, & Heimo, 2000). However, they are also believed to cause radiation levels exceeding the expected clear-sky value (also referred to as enhancements) on the received radiation on the earth's surface if they are thin clouds (Pfister, McKenzie, Liley, Thomas, Forgan, & Long, 2003) (Sabburg & Wong, The effects of clouds on enhancing UVB irradiance at the Earth's surface: A one year study., 2000a) (Estupiñán, Raman, Crescenti, Streicher, & Barnard, 1996) (Weihs, Webb, Hutchinson, & Middleton, 2000) (Schafer, Saxena, Wenny, Barnard, & DeLuisi, 1996). Enhancements may be due to both thick clouds (that scatter radiation) and due to thin clouds (that obscure the direct radiation). Thick clouds absorb radiation, but they can also scatter radiation from their sides, so that some extra radiation gets to the radiometers resulting in enhancement. Thin clouds will scatter the radiation so that much of it becomes diffuse rather than direct and this effect results in enhancement. Cloud fraction (*CF*) is the fraction of the sky covered by clouds. The term cloud cover, cloud fraction and sky cover are being used interchangeably in this text since sky cover is also the fraction of cloud cover provided as a fraction between 0 and 1 (Parisi, Sabburg, Turner, & Dunn, 2007). As mentioned above, cloud cover is a macro-physical aspect, but it is not the only aspect that affects the solar radiation, but micro-physical properties also do affect the solar radiation. However, in this section, we will focus more on how the cloud cover affects the solar radiation reaching the earth's surface of the Durban area.

A Total Sky Imager (TSI) is an instrument that is used to map and measure cloud cover. This instrument can be used in conjunction with the pyranometer and pyrliometer in order to predict the relationship between the cloud cover and the available solar radiation reaching the ground. A pyrliometer is an instrument that is used to measure the direct normal irradiance (*DNI*) or direct solar radiation flux at normal incidence (Garg & Garg, 1993). A pyranometer is used to measure the global horizontal irradiance (*GHI*) and diffuse horizontal irradiance (*DHI*) that is

incident on them within the solid angle (Garg & Garg, 1993). Diffuse horizontal irradiance (*DHI*) is defined as the solar radiation received from the sun after its direction has been changed by scattering by the atmospheric constituents (Duffie & Beckman, 2013). Generally it is the scattered solar radiation from the sky dome (not including *DNI*). Global horizontal irradiance (*GHI*) is the geometric sum of the *DNI* and *DHI* (total hemispheric irradiance). The term “global” is associated with the fact that the solar radiation is received from the entire  $2\pi$  solid angles of the sky vault (Paulescu, Paulescu, Gravila, & Badescu, 2013).

## **1.1 Research aim**

The aim of this research is:

- To explain how cloud cover affects solar radiation measurements using a Total Sky Imager and radiometers in the Durban area.

## **1.2 Research question**

- To what extent are direct and diffuse radiation a function of cloud cover, and over what time period?

## **1.3 Brief history of Sky Imagers (SIs)**

Traditionally, the sky conditions were reported by specially trained human observers resulting in significant discrepancies due to the subjectivity in observations (Silva & Echer, 2013). Human observers were costly to maintain hence the manufacture of radiometry instruments (Long, Sabburg, Calbo, & Pages, Retrieving cloud characteristics from ground-based daytime color all-sky images, 2006). There are many devices that can be used to automatically detect and quantify cloud amount and classify their type optically as in thin, thick or opaque. Satellite information can be used to get cloud information, but because of their weakness in quantifying small and/or low cloud features due to their limited spatial and temporal resolution they are rarely used (Long, Sabburg, Calbo, & Pages, Retrieving cloud characteristics from ground-based daytime color all-sky images, 2006). In order to obtain continuous information on cloud cover, sky-imaging devices are used. Due to improvements in technology in recent years, there has been an increased development of ground-based sky imagers (Long, Sabburg, Calbo, & Pages, Retrieving cloud characteristics from ground-based daytime color all-sky images., 2006). However a Total Sky

Imager is the most common sky imager used in the research industry. More information on the Sky imagers is given in Chapter 3.

## 1.4 Literature review

There are mostly two methodologies that are commonly used for analysing cloud impacts which are namely hypothetical and experimental (Calbo, Pages , & Gonzalez , 2005). Hypothetical methodologies include the utilisation and improvement of radiative exchange hypothesis representing the impact of cloud particles on UV. Bead size dispersion and thickness or optical thickness and effective radius are then again the most critical physical variables that are utilised to depict water mists. Observational methodologies utilise a technique to recreate cloudless radiation and recognize the cloud impact by looking at the contrasts between measured radiation in overcast conditions and the assessed radiation in cloudless condition. Cloud impacts are concluded from the deliberate radiation in overcast conditions when contrasted with the cloudless model in which cloud impacts cannot be clarified like decreases and upgrades (Calbo, Pages , & Gonzalez , 2005). Calbo *et al.* (2005) investigated the exact phenomenon of cloud impacts on UV radiation over Spain. They particularly investigated the relationship between measured UV radiations in shady condition by fundamentally looking at the accompanying two strategies (Calbo, Pages , & Gonzalez , 2005):

- Techniques that include perception of cloud amount by people or using sky cameras.
- Techniques that utilize radiometric estimations as a substitute for cloud perceptions.

The cloud adjustment variable (CMF) is the proportion between the deliberate UV irradiance in overcast sky conditions and an expected cloudless UV irradiance (Staiger, den Outer, Bais, Feister, Johnsen, & Vuilleumier, 2008). Calbo *et al.* (2005) thought about after-effects of various works through figuring of CMF, which changes from 0.3 to 0.7 for cloudy skies relying upon cloud type and attributes. Cloud impact on UV radiation is 15 to 45% lower than on the total solar radiation. It was found that generally clouds have a reducing effect, whereas sometimes it has an enhancing effect on the downwelling radiation. Downwelling radiation is defined as the component of radiation directed toward the Earth's surface from the sun or the atmosphere (Pfister, McKenzie, Liley, Thomas, Forgan, & Long, 2003).

Pfister *et al.* (2003) noticed enhancements in global irradiance for the most part happen on brief time scales; they tend not to be seen in information streams for which the mean irradiance is ascertained utilising a transient window of more than a couple of minutes (Pfister, McKenzie, Liley, Thomas, Forgan, & Long, 2003). In their work, they found that the enhancements in the global irradiance are connected with practically zero decrease in the beam irradiance and an expansion in the diffuse component part. The cloud fields in charge of enhanced surface irradiance do not basically lessen the beam irradiance but they increase scattering thereby increasing the diffuse component (Pfister, McKenzie, Liley, Thomas, Forgan, & Long, 2003). In spite of the fact that the cloud fraction is a predominant component impacting the downwelling radiation, it is additionally clear that data about the cloud scope alone, significantly together with the distinguishing proof of whether the sun is obscured, is not adequate to clarify the real radiation field, particularly if short time variations are considered (Janjai & Tosing, 2000) (Pfister, McKenzie, Liley, Thomas, Forgan, & Long, 2003). The spatial appropriation of mists and their optical properties together have a combined effect on the cloud impact. Parameters from all-sky imaging give a supportive wellspring of data for examining the impact of clouds in the radiation field and that all-sky cameras are reasonable instruments to perform long haul estimations of neighbourhood cloud scope with high transient determination (Pfister, McKenzie, Liley, Thomas, Forgan, & Long, 2003).

Josephson and Landelius (2000) found out that clouds decrease the irradiance received by the surface under overcast conditions (Josefsson & Landelius, 2000). Nevertheless, if there are broken clouds in the sky, then it was noted by Sabburg and Wong (2000) that irradiance enhancements of up to 25% can occur (Sabburg & Wong, The effects of clouds on enhancing UVB irradiance at the Earth's surface: A one year study., 2000a). McKenzie (2001) found out that the same enhancements may occur due to the reflections from cloud decks below high-altitude observation sites such as Mauna Loa Observatory (McKenzie, Johnston, Smile, Bodhaine, & Madronich, 2001). The cloud fraction may be very large, but if the clouds do not directly obscure the beam, then reduction in irradiance reaching the surface may be small. Hence Schwander *et al.* (2002) deduced that even though the cloud fraction is higher it is of utmost importance to check if the Sun is obscured or not (Schwander, Koepke, Kaifel, & Seckmeyer, 2002). Seckmeyer *et al.* (1996) discovered a bimodal distribution when they have related cloud

transmission as a function of cloud amount with a lower peak corresponding to the condition when the sun is obscured by clouds and a higher peak for non-obscured sun (Seckmeyer, Erb, & Albold, 1996). The fact that the sun can be obscured for small cloud fraction and be unobscured for large cloud fraction creates problems as far as quantification of cloud effects is concerned. Complications may also arise when scattering of radiation by clouds increase the chances of absorption by ozone as noted by Krotkov *et al.* (1998) (Krotkov, Bhartia, Herman, Fioletov, & Kerr, 1998) or increases chances of scattering by aerosols within the cloud as noted by Erlick *et al.* (1998) (Erlick & Frederick, 1998).

Sabburg and Wong (2000) noted that ground-based measurements of cloud cover are commonly done now through the use of automated all-sky imagery (Sabburg & Wong, Evaluation of sky/cloud formula for estimating UV-B irradiance under cloudy skies, 2000b). Most of the sky imagers still encounter challenges in distinguishing high thin clouds, but nonetheless, these continuous records of the spatial distribution of clouds being used in conjunction with radiometric measurements offer the potential to accurately quantify the cloud effects.

Calbo *et al.* (2008) carried out a similar research whereby they were looking at the cloud effects on UV radiation at two opposing hemispheric sites. They quantitatively assessed the effect of clouds on UV reaching the ground through the use of Cloud Modification Factors (CMF) (Calbo, Sabburg, Badosa, & Gonzalez, 2008). Their CMF behaviour was derived from two different sites which are Girona in Spain and Toowoomba in Australia. They had sky cameras and UV radiometers that took images and measurements respectively for 5 years. However the UV measurements were averaged in 15-minute intervals. Their whole sky images were used to derive cloud fraction and establish cloud type where cloud was classified into five different categories namely clear, cumuliform, layered, cirriform and molted (Calbo, Sabburg, Badosa, & Gonzalez, 2008). The cloud fraction was therefore an average for the 15-minute interval used. They used these measurements to compute the CMF depending on the cloud fraction and for different cloud types. Their results were in agreement with the previous findings, which are as follows (Calbo, Sabburg, Badosa, & Gonzalez, 2008):

- Cloud effects are in general significant for cloud fraction larger than 0.7,

- Similar cloud fractions produce a large range of CMF values, partly due to different cloud types,
- Cloud effects result sometimes in an enhancement of UV radiation.

This research is similar to the present study except that we are measuring solar radiation rather than UV radiation.

Sunlight based radiation conduct can best be comprehended by physical displaying and measurable sun oriented climatology. Physical demonstrating implies here that the physical procedures happening in the environment and impacts solar radiation. As said above in the literature, the radiation at the surface relies on atmospheric absorption and scattering processes. The physical model is only in light of physical contemplations, permitting radiant energy trade to happen inside the earth-atmosphere framework. This approach governs models that account for the simulated solar radiation at the ground in terms of a certain number of physical parameters, for example, clouds, cloud sorts, water vapour substance, dust and mist concentrates, etc. Statistical solar climatology modelling has become a tool mainly to produce quick solutions in solar energy conversion and most researchers have grown much interest in it. Statistical solar climatology displaying can be subdivided into the accompanying approaches (Tovar-Prencador, 2008):

- Descriptive factual examination, for every spot and time of the year, of the fundamental amounts of interest, (for example, hourly or day by day global, diffuse or pillar sun powered light) and measurable displaying of the observed empirical frequency distributions;
- Investigation of the factual relationship among the primary sun based radiation parts from one viewpoint (for example diffuse versus worldwide illumination) and the spatial connection between concurrent sunlight based information at better places on the other;
- Research on the factual interrelationship between the primary sun based illumination segments and other accessible meteorological parameters, for example, daylight length, shaded area, temperature, etc;

- Forecasting of sun powered radiation values at a given place or time taking into account recorded information. The factual estimating models regularly constitute a strategy utilized as a part of atmosphere forecast. It is additionally a suitable philosophy to gauge the plausible future conduct of a framework in view of its recorded estimations.

The fundamental favourable position offered by the physical techniques, in contrast with the measurable ones, is their spatial autonomy. They additionally do not require solar radiation information measured at the earth's surface. Be that as it may, the physical technique needs integral meteorological information to describe the associations of sun based radiation with the environment. Nevertheless, the physical and measurable techniques are identified with each other. The parameters that administer a physical model take values, which fluctuate as per the adjustments in the meteorological conditions. Consequently, in the event that we are occupied with utilising a physical model as part of a request to gauge information in a decided site, measurements must be presented at the level of the model parameters. However, any measurable investigation which does not deliberately pick the right amounts by checking their central physical and meteorological connections, is strongly criticised to give inconsequential results (Tovar-Prescador, 2008). A considerable measure of exploration has been in progress utilising the physical and factual demonstrating.

Liu and Jordan (1960) studied the interrelationship and characteristic distribution of direct, diffuse and total solar radiation. In their study, they looked at relationships between beam and diffuse radiation on clear and cloudy days in isolation and did a comparison of the two different weather conditions. Their discussion was based on dimensionless transmission coefficients of direct and diffuse solar radiation and clearness index and diffuse fraction. According to Liu and Jordan (1960), the transmission coefficient for direct solar radiation is given as follows (Liu & Jordan, 1960):

$$\tau_D = \frac{I_{Dh}}{I_{oh}} \quad (1.1)$$

where  $I_{Dh}$  is intensity of direct radiation incident upon a horizontal surface and  $I_{oh}$  intensity of solar radiation incident upon a horizontal surface upon outside the atmosphere of the earth. Liu

and Jordan (1960) expressed the transmission coefficient for diffuse solar radiation as follows (Liu & Jordan, 1960):

$$\tau_d = \frac{I_{dh}}{I_{oh}} \quad (1.2)$$

where  $I_{dh}$  is intensity of diffused radiation incident upon a horizontal surface and  $I_{oh}$  intensity of solar radiation incident upon a horizontal surface upon outside the atmosphere of the earth. The relationship between transmission coefficient for direct and diffuse solar radiation was established. In studying the relationship between daily diffuse and daily total radiation on cloudy days they introduced the concept of clearness index and diffuse fraction. Liu and Jordan (1960) expressed clearness index as follows (Liu & Jordan, 1960):

$$K_T = \frac{H}{H_0} \quad (1.3)$$

where  $H$  is the daily average global radiation received on a horizontal surface and  $H_0$  is the extraterrestrial daily insolation received on a horizontal surface. Liu and Jordan (1960) refers to clearness index as the cloudiness index also, which mean that they believed that variation in the clearness index is only influenced by the cloud cover. Wong and Chong (2001) expressed the clearness index as in equation (1.1), which uses the notation in Appendix A (see Table A1), is given by (Wong & Chow, 2001):

$$k_t = \frac{I_t}{I_o} \quad (1.4)$$

where  $I_t$  is the hourly global solar irradiance on a horizontal surface and  $I_o$  is the hourly extraterrestrial irradiance. Carrol (1984) referred to  $K_T$  as the global transmissivity but expressed the same manner as Liu and Jordan (1960. Carrol (1984) expressed the clearness index as in equation (1.1), which uses the notation in Appendix A (see Table A1), is given by (Carrol, 1984):

$$K_t = \frac{G}{I_o \cos z} \quad (1.5)$$

where  $G$  is the total global horizontal radiation,  $I_o$  is the extraterrestrial beam values and  $z$  is the solar zenith angle

Liu and Jordan (1960) expressed the diffuse fraction as follows (Liu & Jordan, 1960):

$$\text{Diffuse fraction} = \frac{D}{H} \quad (1.6)$$

where  $D$  is the daily diffuse radiation on a horizontal surface and  $H$  is the daily global radiation on a horizontal surface. However, Wong and Chow (2001) expressed the diffuse fraction as in equation (1.6), which, using the notation in Appendix A (see Table A1), (Wong & Chow, 2001):

$$k_d = \frac{I_d}{I_t} \quad (1.7)$$

where  $I_d$  is the hourly diffuse irradiance on a horizontal surface and  $I_t$  is the hourly global solar irradiance. Tsubo and Walker (2003) instead expressed the diffuse fraction as  $K$  (Tsubo & Walker, 2003). Liu and Jordan (1960) discovered that a firm relationship existed between the clearness index and the diffuse fraction. Liu and Jordan(1960) however got an inconsistency in the data for points with  $K_t$  near zero, they corrected it in such a way that when  $K_t$  values approaches zero the diffuse fraction have to approach the limit of one (Liu & Jordan, 1960). Instead of using daily averages, some authors correlated hourly diffuse fraction with hourly clearness index (Orgill & Hollands, 1977).

Wong and Chow (2001) further expressed the atmospheric diffuse coefficient,  $k_D$ , as follows:

$$k_D = \frac{I_d}{I_o} \quad (1.8)$$

where  $I_o$  is the hourly extraterrestrial irradiance. The diffuse fraction is close to one when it is cloudy since  $DHI$  and  $GHI$  are almost equal. Nevertheless, when  $GHI$  is large,  $DHI$  is small and the diffuse fraction is small. Nevertheless, Tsubo and Walker (2003) classified  $K$  with respect to  $K_t$  over the following ranges of  $K_t$ : low  $K_t$  class ( $0.0 \leq K_t < 2$ ), middle  $K_t$  class ( $0.2 \leq K_t \leq 0.8$ ) and high  $K_t$  class ( $0.8 < K_t \leq 1.0$ ) (Tsubo & Walker, 2003). A high  $K_t$  class represents a clear sky condition and or a high solar elevation, whereas a low  $K_t$  class represent an overcast condition and or a low solar elevation. It can be generalised that the diffuse fraction is small in

the high  $K_t$  class and big in the low  $K_t$  class (Tsubo & Walker, 2003). However, most of their diffuse fraction data was distributed over the middle class  $K_t$  class range.

A complementary relationship was given by Tovar-Pescador (2008) between  $GHI$  parameterized as the clearness index ( $k_t$ ) and the atmospheric transmittance for beam radiation for direct normal beam irradiance ( $k_b$ ) follows (Gueymard & Myers, 2008):

$$k_b = \frac{DNI}{DNI_{extraterrestrial}} \quad (1.9)$$

where  $DNI_{extraterrestrial}$  is the extraterrestrial direct normal irradiance. Wong and Chong expressed the clearness index as in equation (1.9), which, using the notation in Appendix A (see Table A1), is given by (Wong & Chow, 2001):

$$k_b = \frac{I_b}{I_o} \quad (1.10)$$

where  $I_b$  is the hourly beam irradiance on a horizontal surface and  $I_o$  is the hourly extraterrestrial radiation.

The following conditions may be tested to fulfil the data quality control requirements of the entire dataset before it is used. These conditions were listed by Jacovides *et al.* (2006) and proposed by the European Commission Daylight 1 in 1993 (Lanini, 2010). The conditions for reliable data to be used are as follows (Lanini, 2010):

$$I \geq 0 \quad (1.11)$$

$$\frac{I_d}{I} \leq 1.1 \quad (1.12)$$

$$\frac{I}{I_{o,h}} \leq 1.2 \quad (1.13)$$

$$I_b \leq I_{o,h} \quad (1.14)$$

where  $I$  is the global radiation,  $I_b$  is the horizontal direct radiation and  $I_d$  is the horizontal diffuse radiation and  $I_{o,h}$  is the horizontal extraterrestrial radiation.

Marquez *et al.* (2011) used sky cover indices to forecast global horizontal irradiance (Marquez, Gueorgulev, & Coimbra, 2011). The main goal of their research was to correlate TSI cloud cover measurements, Infrared Radiation (IR) and Solar Radiation (SR) at the earth's surface and use this information as input for modelling and forecasting of the solar radiation. As part of their work they considered the effects of cloud cover on *GHI*. In order to remove the dependence of *GHI* on the solar zenith angle, to isolate the cloud effects on *GHI* and to compare with sky cover indices based on the TSI and IR measured values, they used the clearness index  $K_g$  which is given as follows (Marquez, Gueorgulev, & Coimbra, 2011):

$$K_g = \frac{GHI}{GHI_{clear}} \quad (1.15)$$

Where *GHI* is global horizontal irradiance and  $GHI_{clear}$  ( $GHI_c$ ), is the global horizontal irradiance for a clear sky. In order to estimate their  $GHI_{clear}$ , they used selected clear days to benchmark their estimate.  $K_g = 1$  for clear days and for cloudy days it is a very small value depending on the total cloud cover. They defined the sky cover variability based on *GHI* to be as follows (Marquez, Gueorgulev, & Coimbra, 2011):

$$SC_{GHI} = 1 - \frac{GHI}{GHI_{clear}} = 1 - K_g \quad (1.16)$$

In other words, the above equation can be used to determine the cloud fraction which is directly measured by the TSI.

Black (1956) (as cited in Janjai and Tosing (2000)) used data from many parts of the world and established a quadratic model relating cloud cover to global radiation. Janjai and Tosing (2000) developed a new model for calculating global radiation from cloud cover data for Thailand (Janjai & Tosing, 2000). Development of this particular model involved correlating the ratio of daily global ( $\bar{H}$ ) to daily extraterrestrial radiation ( $\bar{H}_0$ ) as  $(\frac{\bar{H}}{\bar{H}_0})$  and cloud cover ( $C$ ) for cities in Thailand and quadratic best fit curves were obtained and the lowest coefficient of determination ( $R^2$ ) of 0.3028 was obtained. To reduce the number of values far away from the linearity they computed monthly average of daily global to monthly average daily extraterrestrial radiation and adopted them against monthly average daily cloud cover. They fitted a quadratic curve of best fit

and found that the  $R^2$  values improved. However, they plotted the long-term (4 year period) monthly average daily global to monthly average extraterrestrial radiation ( $\frac{\bar{H}}{\bar{H}_0}$ ) against the long-term monthly average of daily cloud cover ( $\bar{C}$ ) and their plots were best-fitted by a straight line and had a correlation coefficient ( $R$ ) higher than 0.93. The correlation coefficient was higher than 0.93 for all their stations for long-term basis whilst for short-term basis the correlation coefficient was as low as 0.3028 (Janjai & Tosong, 2000). As previously mentioned, solar radiation is mainly affected by clouds, implying that the correlation coefficient of global to extraterrestrial radiation with clouds should be significantly higher. The long-term basis constituted values of the monthly average of daily global computed as a ratio daily extraterrestrial radiation to monthly averages. In their work they found out that indeed there is a relationship between global radiation and cloud cover, but it is more significant when you quantify it for long-term basis than for short term basis.

An approach for estimating average daily global solar radiation from cloud cover in Thailand was proposed again by the same author Janjai and Nimmuan (2011) (Nimmuan & Janjai, 2012). Basically, they used the same method as before, except that they were looking at 24 sites in Thailand. They integrated the 10-minute average irradiance from each station over a day to get their daily global radiation in MJ/m<sup>2</sup>. They removed all the data that violated the physical laws from their dataset. Their cloud covers from each station were obtained from visual observation from well-trained meteorologists. Their observations were done in three hours' time interval specifically at 07h00, 10h00, 13h00 and 16h00 of their local time. They used tenths of the sky to quantify their cloud cover of the sky covered by the clouds. Their solar radiation and cloud cover data used for their work is for a period of 4-8 years. Their data were classified into two groups of data sets, one set of 24 stations for the model formulation and the other 4 stations for testing the model. In their work, the ratio of global ( $\bar{H}_m$ ) to extraterrestrial radiation ( $\bar{H}_0$ ) is termed the normalized global radiation (also known as clearness index) and is correlated with cloud cover. The normalized global radiation is used so as to eliminate the effect of the variation of the sun-earth distance. The governing equation that was used in correlating the normalized global radiation,  $\frac{\bar{H}_m}{\bar{H}_0}$ , (clearness index) with the cloud cover,  $\bar{C}$ , (cloud fraction) is as follows:

$$\frac{\bar{H}_m}{\bar{H}_o} = a_0 + a_1 \bar{C} \quad (1.17)$$

where  $a_0$  and  $a_1$  are the y-intercept and slope, respectively. They have found a relationship between the normalized global radiation and cloud cover, with a correlation coefficient ranging from 0.76 to 0.98. (Nimnuan & Janjai, 2012).

In Lauder, Central Otago, New Zealand, a technique to evaluate the cloud effect that uses estimates for the clear-sky surface irradiance as a source of perspective and look at the proportion of measured to assessed clear-sky qualities was utilised by Pfister *et al.* (2003). In their work they utilised a hemispherical sky imaging method (for more data refer to Long and De Luisi (1998)) (Long & DeLuisi, Development of an automated hemispheric sky imager for cloud fraction retrievals., 1998). Measurements over a year of the cloud-fraction, global, direct and diffuse solar irradiance were utilised to examine the impact of the cloud fraction on the radiation field at the Earth's surface. To evaluate the cloud effect, the methodology utilised depends on the proportion of measured surface irradiance to expected clear-sky values. To gauge clear-sky information for assessing radiation levels under cloudless conditions as a component of the solar zenith angle they connected a non-linear least squares fit. Appraisals of clear-sky qualities can be deduced from radiative exchange simulations or from a parameterization of clear-sky irradiance. They utilised the last method utilising the solar zenith angle as the essential component to decide the downwelling sunlight based irradiance under clear-sky conditions. As a result of these different variables, a straightforward relationship between cloud portion and downwelling surface radiation does not exist (Pfister, McKenzie, Liley, Thomas, Forgan, & Long, 2003). While cloud cover data may be considered less desirable than sunshine as a parameter to be used in modelling solar radiation, some research indicated that accurate monthly predictions of the global solar radiation can be made using hourly cloud cover models (Turner & Mujahid, 1984).

Pfister *et al.* (2003) utilised two computerised all-sky imaging frameworks for cloud cover data and they have likewise recognised whether the clouds have obscured the sun or not. Their first instrument, introduced in April 1998, was called Allsky1 and was produced at the National Institute of Water and Atmospheric exploration (NIWA) in Lauder. Their second instrument, called Allsky2, which began operation in September 1999, is a total sky imager (TSI) produced

by Yankee Environmental Systems Inc. These two instruments were positioned 300 m apart to permit utilisation of pictures for stereographic investigation of cloud altitude (Pfister, McKenzie, Liley, Thomas, Forgan, & Long, 2003). They used the solar irradiance measurements from Lauder which are part of the International Baseline Surface radiation Network (BSRN). The Allsky2 sky imager system is approximately 5 m away from the radiation sensors which are located on the roof of Laboratory buildings in Lauder. The radiation measurements taken from the BSRN were joined with the Allsky1 and Allsky2 cloud datasets to shape the premise for researching the relationship between cloud fraction and sunlight based surface irradiance.

Pfister *et al.* (2003) utilised evaluations for the clear-sky surface irradiance (*GHI*) as a source of perspective and looked at the proportion of measured to assessed clear-sky values as a technique to evaluate the cloud effect. The estimate for the clear-sky surface irradiance was inferred through parameterisation utilising the solar zenith angle as the essential variable to decide the downwelling sun oriented irradiance under clear-sky conditions. The formula used for calculating the clear-sky irradiance ( $I_{clear}$ ) is as follows (Pfister, McKenzie, Liley, Thomas, Forgan, & Long, 2003):

$$I_{clear} = a \cos(SZA)^b \quad (1.18)$$

where *SZA* is the solar zenith angle, and *a* and *b* are computed from the least squares fit. The used clear-sky data were chosen from the dataset by taking measurements when the corresponding cloud fraction reading was 0% from both imagers. Through use of this clear-sky information they figured the coefficients *a* and *b* which were observed to be as per the following  $a = 1125.4$  and  $b = 1.21$ . Solar zenith angles were confined to  $75^\circ$  or less for clear-sky gauges since nature of the fit gets to be poor if low rise sun edges are incorporated (Pfister, McKenzie, Liley, Thomas, Forgan, & Long, 2003).

Pfister *et al.* (2003) utilised the Long and Ackerman (2000) procedure to get evaluations of the *DNI* sun based irradiance since the measured-to-direct assessed clear-sky irradiance as well, which give data with respect to the cloud sway on the surface radiation (Long & Ackerman, Identification of clear skies from broadband pyranometer measurements and calculation of downwelling shortwave cloud effects., 2000). Their exact fit was precise to within  $\pm 10\%$  and

was autonomous of the two parameters utilised. Using the above equation 1.17, the fitting coefficients were observed to be,  $a = 1060$  and  $b = 0.20$  (Pfister, McKenzie, Liley, Thomas, Forgan, & Long, 2003). They performed the same procedure, but using *DHI* under the clear-sky. However, the agreement between the measured and estimated clear-sky information was observed to be worse than that for *GHI* and *DNI*. This observation was caused by the measure of clear-sky diffuse radiation being small and strongly influenced by the variability in the air vaporised substances. The exactness of this fit was inside the scope of  $\pm 20\%$  (Pfister, McKenzie, Liley, Thomas, Forgan, & Long, 2003). In their plight to discover the relationship between cloud fraction and sun based radiation they correlated monthly mean radiation ratio ( $H/H_c$ ) and the monthly mean *CF* and found a correlation coefficient of  $R = -0.9$ . Khan *et al.* (2012) stated that  $H/H_c$  correlations give better results of correlation coefficient than the clearness index  $H/H_o$  (Khan & Ahmad, 2012).

Augustine and Nnabuchi (2009a) developed regression equations to predict the relationship between global solar radiation with a combination of one or more of the meteorological parameters (Augustine & Nnabuchi, Empirical models for the correlation of global solar radiation with meteorological data for Enugu, Nigeria., 2009a). The meteorological parameters are fraction of sunshine, maximum temperature, cloudiness index and relative humidity. In their method, they used the monthly mean daily cloud cover data for four selected cities mentioned above collected from the Nigerian Meteorological Agency, Federal Ministry of Aviation, Oshodi in Lagos. They collected their global solar radiation data courtesy of Renewable Energy for rural Industrialisation and Development in Nigeria. Their data covered a period of 17 years, ranging from 1990 to 2007. In their model they converted the measured global solar radiation data from  $\text{kWhm}^{-2}\text{day}^{-1}$  to  $\text{MJm}^{-2}\text{day}^{-1}$  by using a factor of 3.6 (Iqbal, 1983). Kimbal (cited in Augustine and Nnabuchi (2009a)) established that a relationship exists between insolation and the amount of sky covered by clouds (Augustine & Nnabuchi, Correlation of cloudiness index with clearness index for four selected cities in Nigeria., 2009b). Correlations were made for clearness index and individual meteorological parameters mentioned which is one variable for Enugu area only. The method was repeated for two variables up until all the meteorological parameters were correlated on one regression equation as above. By making use of the Statistical Package for the Social Sciences (SPSS) software program, the regression equation for Enugu was computed with the

same general formula as given in equation below (Augustine & Nnabuchi, Correlation of cloudiness index with clearness index for four selected cities in Nigeria., 2009b).

$$\frac{H_m}{H_o} = a + b \frac{\bar{n}}{\bar{N}} + c \bar{T}_m + d \frac{\bar{c}}{\bar{C}} + e \frac{R}{100} \quad (1.19)$$

where  $a$  is the y-intercept and  $b$ ,  $c$ ,  $d$  and  $e$  are the slopes,  $\bar{T}_m$  is the maximum temperature,  $\frac{\bar{c}}{\bar{C}}$  is the cloudiness index and  $R$  is the relative humidity. Here  $\bar{C} = 100$ .

Augustine and Nnabuchi (2009b) studied the relationship between the cloudiness index and the clearness index for the following four cities in Nigeria, Port Harcourt, Calabar, Warri and Uyo (Augustine & Nnabuchi, Correlation of cloudiness index with clearness index for four selected cities in Nigeria., 2009b). Extraterrestrial radiation ( $H_o$ ) is the maximum amount of solar radiation available to the earth at the top of the atmosphere and  $H$  being the actual amount of radiation available at the ground after interacting with the atmosphere and its components. It implies that the ratio  $H/H_o$  will be a measure of how transparent is the atmosphere to the solar radiation (Augustine & Nnabuchi, Correlation of cloudiness index with clearness index for four selected cities in Nigeria., 2009b). The ratio defines the coefficient of transmission or transmittance of the atmosphere. This ratio is termed the clearness index of the atmosphere and is used as a variable in solar radiation measurement (Liu & Jordan, 1960) (Babatunde & Aro, 1990). Augustine and Nnabuchi (2009b) also mentioned another important ratio, the cloudiness index which is also used as a variable in solar radiation measurement. The cloudiness index defines the cloudiness or turbidity of the atmosphere and is defined as the ratio of diffuse solar radiation  $H_d$  to global solar radiation  $H$  (Augustine & Nnabuchi, Correlation of cloudiness index with clearness index for four selected cities in Nigeria., 2009b).

Augustine and Nnabuchi (2009b) used the following regression equation to correlate the clearness index with the cloudiness index (Augustine & Nnabuchi, Correlation of cloudiness index with clearness index for four selected cities in Nigeria., 2009b):

$$\frac{H}{H_o} = a - b \frac{\bar{c}}{\bar{C}} \quad (1.20)$$

Where  $a$  and  $b$  are regression constants,  $\frac{H}{H_0}$  is the clearness index and  $\frac{\bar{c}}{\bar{C}}$  is the cloudiness index where  $\bar{c}$  is the cloud cover and  $\bar{C} = 100$ .

The measured global solar radiation and cloud cover was correlated using the SPSS computer software program for regression analysis. In their conclusions, they stated that correlations based on cloudiness index are less reliable than the corresponding sunshine correlation. They gave the following reasons for their argument based on Norris 1968 (Norris, 1968),

- Insolation and sunshine measurements involve taking readings for the entire day, whereas the mean cloud cover from the meteorologists is only average observations taken after every 3 hours.
- The cloud fraction percentage does not give the information as to which part of the sky is covered by the clouds. It is possible that one small cloud could keep on obstructing the sun for a long time as it traverses the sky.
- It is possible that the cloud obscuring the sun may have a hole that will allow radiation to pass through for even a long period of time. Also the reflection of solar radiation from the edges and sides of the clouds may increase the insolation to even more than that received above the atmosphere.

However, they suggested that by making use of the new variable opaque sky cover instead of total sky cover, it is possible to reduce the above disadvantages (Bennet, 1969).

However, since the current study is not about predicting any variable or forecasting, we shall correlate for:  $\frac{GHI}{GHI_0}$ ,  $\frac{GHI}{GHI_c}$ ,  $\frac{DNI}{DNI_0}$ ,  $\frac{DNI}{DNI_c}$ , and  $\frac{DHI}{DHI_c}$  versus cloud fraction  $CF$ . These correlations are important for the current study as they reveal the relationship between radiometric measurements and cloud cover which is the primary goal of this research. However, it should be noted that since this research is looking at short time-frames, it is expected that the correlation coefficient may not be so high according to Janjai and Tosing (2000) work (Janjai & Tosing, 2000). Nevertheless, shorter time-frames exhibit very well the behaviour of cloud effect on solar radiation such as solar enhancements and reductions.

## **1.5 Summary of chapters**

In Chapter One an introduction to this study is given and findings from previous research relating to this study are discussed.

Chapter Two describes the background physics relating to solar radiation being discussed.

Chapter Three gives an in depth information on the instruments that will be used to establish the relationship between the radiometers reading and TSI readings.

Chapter Four comprise of the methods that will be used in the study through describing in detail the data that will be collected, how the data will be analysed and the type of graphs to be expected.

In Chapter Five the results are presented and discussed. Descriptive and quantitative discussion of the results are presented in this chapter. It is in this chapter where the research question will be addressed.

Chapter Six comprises of the discussion of the main outcomes from the discussion of the results and how they compare with the earlier results from the previous research.

Chapter Seven is a conclusion that consists of a brief summary of the aims and outcomes of the research study.

# Chapter 2

## Solar Radiation

The sun is the source of solar radiation. The nature of the energy radiated by the sun is determined by its structure and its characteristics. The sun is spherical in shape and consists of extremely hot gaseous matter with a diameter of  $1.39 \times 10^9$  m and it is  $1.5 \times 10^{11}$  m from the earth. A schematic structure of the sun is shown in Fig 2.1. The effective blackbody temperature of the sun is approximately 5777 K whilst the central interior regions have temperatures that vary from  $8 \times 10^6$  to  $40 \times 10^6$  K and its density is about 100 times that of water.

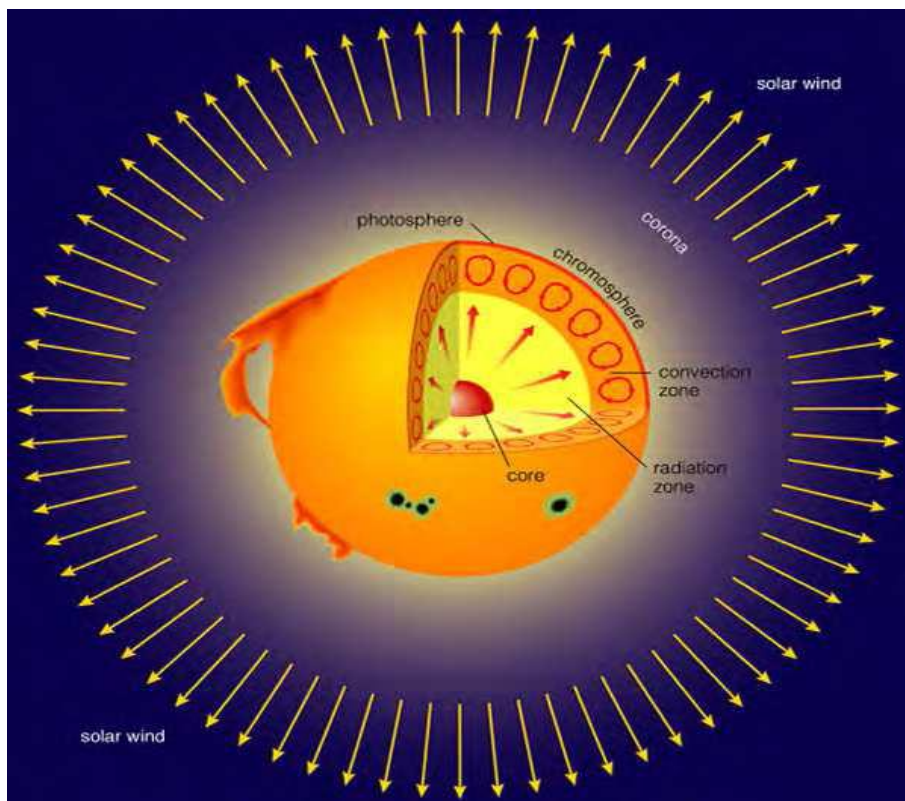


Figure 2.1: Structure of the sun (Falayi & Rabi, Solar radiation models and information for renewable energy applications, 2012).

The sun may be seen as a continuous fusion reactor having its constituent gases as the virtual containing vessel retained by gravitational forces. Energy is produced when hydrogen (i.e. four protons) combine to form helium (i.e. one helium nucleus) which ultimately has a mass less than that of four protons and the difference in mass relates to the produced energy according to Einstein's formula,  $E = mc^2$ . The produced energy in the sun's interior is transferred to its surface where it is radiated into the outer space. This chapter will look in detail how the solar radiation interacts with the atmospheric particles as it makes its way to the earth. The orientation of the sun and the earth will also be discussed, including an introduction of how we get *DNI*, *DHI* and *GHI*.

## **2.1 Interaction of solar radiation with the atmosphere**

It is a fact that any object with a temperature above absolute zero emits radiation. The sun has a temperature of about 6000 K therefore emits radiation. Radiation emitted by the sun ranges over a wide range of wavelengths. Solar radiation emitted by the sun consists of wavelength that ranges from 300 nm (gamma rays) to 3000 nm (microwaves) and carries electromagnetic energy. Radiation with shorter wavelength (high frequency) have high energy and that with longer wavelength (low frequency) have lower energy (Stoffel, et al., 2010). After screening by the layers of the atmosphere, visible light ( $380 \text{ nm} < \lambda < 780 \text{ nm}$ ) comes out unscattered and reaches the surface in abundance. However, there are some portions of the edges of the visible light that also reach the surface namely ultra-violet ( $\lambda < 380 \text{ nm}$ ) and infrared ( $\lambda > 780 \text{ nm}$ ) ranges (Govender, 2013). Ultraviolet consists of wavelengths that are too short whilst the infrared consist of wavelengths that are too long to be seen by the naked eye. The distribution of this electromagnetic radiation of different wavelengths forms the solar spectrum. The solar spectrum may be approximated to that of a blackbody at a temperature of 5800 K. However, due to the absorption of some parts of the spectrum, the resultant spectrum received at the earth's surface is significantly altered. Fig 2.2 shows the solar energy spectrum.

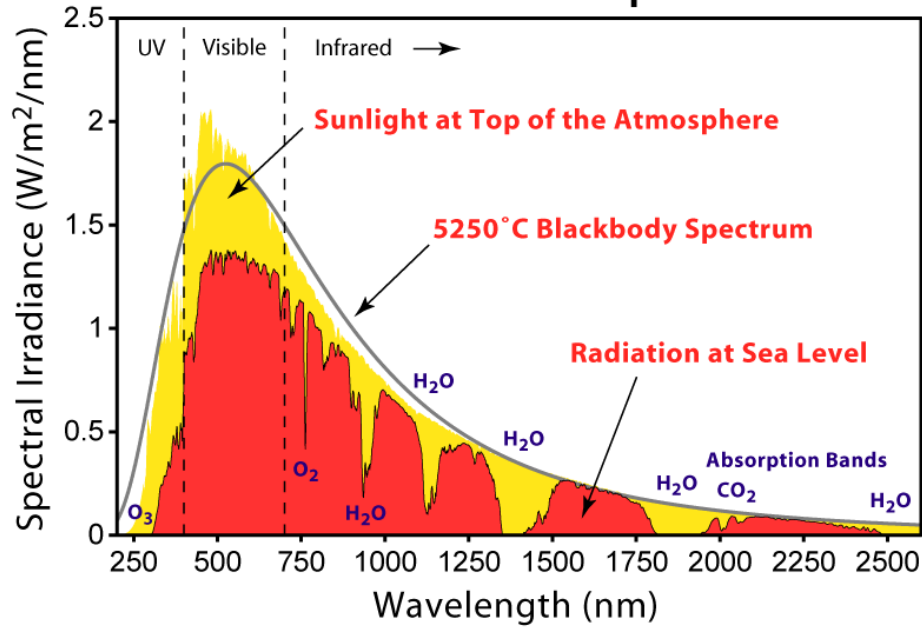


Figure 2.2: The atmosphere affects the amount and distribution of solar radiation reaching the ground (Stoffel, et al., 2010).

When sunlight makes its way through the earth's atmosphere, it can be absorbed, scattered or make its way unaffected to the surface of the earth. In the absorption of sunlight whether visible, infrared, or ultra-violet the following factors play a large role: water vapour, ozone, oxygen, and carbon dioxide (Falayi & Rabi, Solar radiation models and information for renewable energy applications, 2012). The biggest challenge to predict solar irradiance levels is the variability of meteorological and atmospheric conditions, or cloud cover. When radiation is passed through a medium it is normally weakened by its interaction with matter. This interaction is referred to as attenuation or extinction, which is best described as absorption and scattering. When light meets an obstacle its energy will be absorbed, the absorbed energy may be radiated back in all directions or in some instance, it may cause the atoms of that object to vibrate in their fixed positions resulting in an increase in thermal energy. When the light energy is radiated back in all directions this process is called re-radiation and when light energy is converted to thermal energy the process is called absorption. If the medium is non-scattering, then it absorbs the following fraction termed  $A_\lambda$  (<http://www.scratchapixel.com/lessons/3d-advanced-lessons/volume-rendering/volume-rendering-for-artists/>):

$$A_\lambda = 1 - T_\lambda \quad (2.1)$$

where  $A_\lambda$  is the absorptivity and  $T_\lambda$  is the transmissivity (spectral transmittance) and it gives an indication of how much light radiation is absorbed as a light rays pass through an absorbing material. The diagram in Fig 2.3 shows the interaction of solar radiation with the atmosphere and its components.

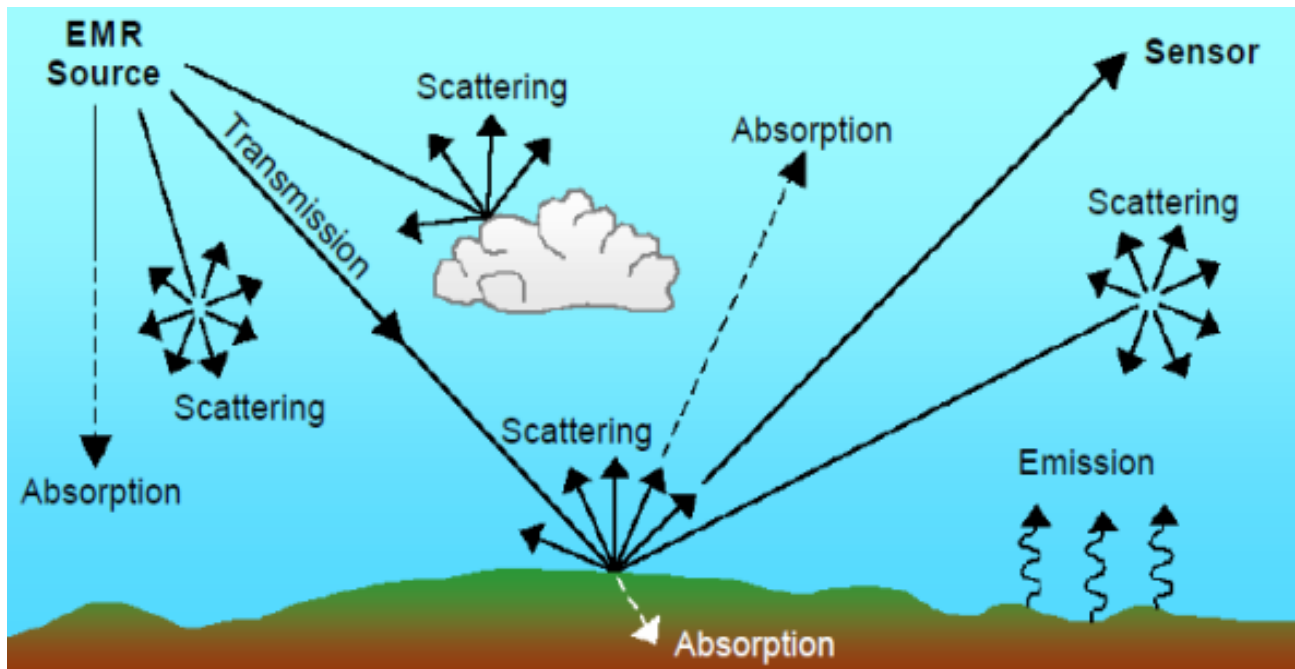


Figure 2.3: Interaction of incoming Solar Radiation with the atmosphere and ground (Remote sensing:Fundamental concepts+).

Scattering is the spreading of a stream of particles or a beam of rays of an electromagnetic wave in all directions as a result of collisions with other particles (or molecules). As scattering is taking place some incident radiation may be reflected back in the direction of the incident radiation. The reflected (backscattered) radiation expressed as a ratio to the incident intensity is called monochromatic reflectivity,  $R_\lambda$ . This lead to the following formula (<http://www.scratchapixel.com/lessons/3d-advanced-lessons/volume-rendering/volume-rendering-for-artists/>):

$$T_\lambda + A_\lambda + R_\lambda = 1 \quad (2.2)$$

In the atmosphere, the particles responsible for scattering range from gas molecules ( $\sim 10 \mu\text{m}$ ) to large raindrops and hail particles ( $\sim 100 \mu\text{m}$ ). The following categories may be distinguished (<http://www.scratchapixel.com/lessons/3d-advanced-lessons/volume-rendering/volume-rendering-for-artists/>):

- solid aerosols (0.1 to 1  $\mu\text{m}$ ), irregular shape, variable refractive index;
- haze water drops (0.1 to 1  $\mu\text{m}$ ), spherical, known refractive index;
- cloud water drops (1 to 10  $\mu\text{m}$ ), spherical, known refractive index;
- cloud ice particles (1 to 100  $\mu\text{m}$ ), irregular shape, known refractive index.

Based on the size of the scattering particles, we distinguish between

- Rayleigh scattering, particle diameter  $\ll$  wavelength of the incident beam
- Mie scattering, particle diameter  $\sim$  wavelength of the incident beam

The symmetry between forward and backward scattering characterizes Rayleigh scattering. Mie scattering therefore result when there is an increasing proportion of the incident radiation as a result of an increase in size of the particles. The sketch of the angular pattern of the scattered intensity of particles of different sizes is shown in Fig 2.4 (<http://www.scratchapixel.com/lessons/3d-advanced-lessons/volume-rendering/volume-rendering-for-artists/>).

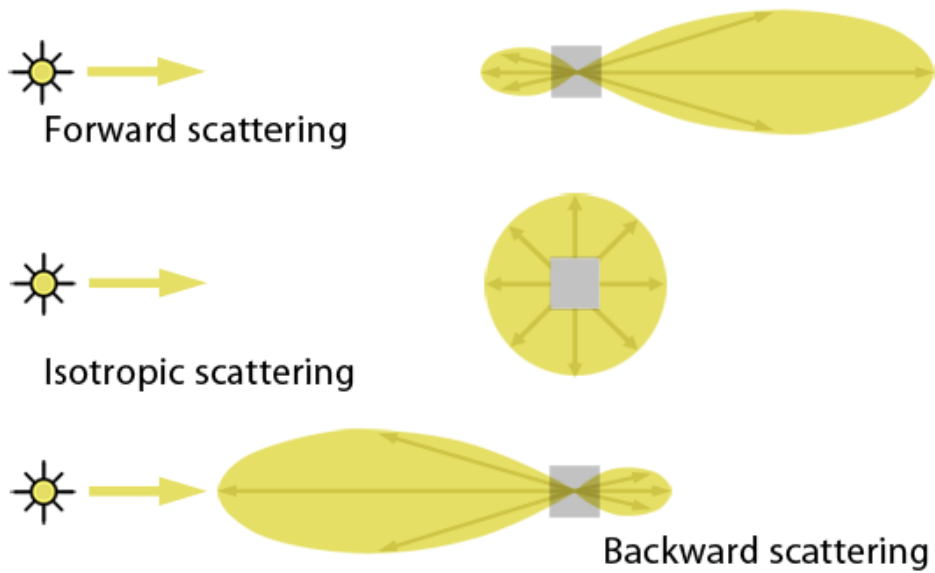


Figure 2.4: Sketches of angular pattern of the scattered intensity from particles of various sizes (<http://www.scratchapixel.com/lessons/3d-advanced-lessons/volume-rendering/volume-rendering-for-artists/>).

The ratio of the mass of the atmosphere through which beam radiation passes to the mass it would pass through if the sun was directly overhead (zenith) is called the air mass (Duffie & Beckman, 2013). The Air Mass (AM) may also be defined as the path length that is travelled by the light through the atmosphere which is normalized to the length when the sun is directly overhead. The AM gives information on how much light power is reduced as light pass through the atmosphere as shown in Fig 2.5. The light is reduced due to absorption by air and dust. The AM is given by the first order approximation that is valid at almost all times outside sunrise and sunset as follows:

$$AM = \frac{1}{\cos \theta} \quad (2.3)$$

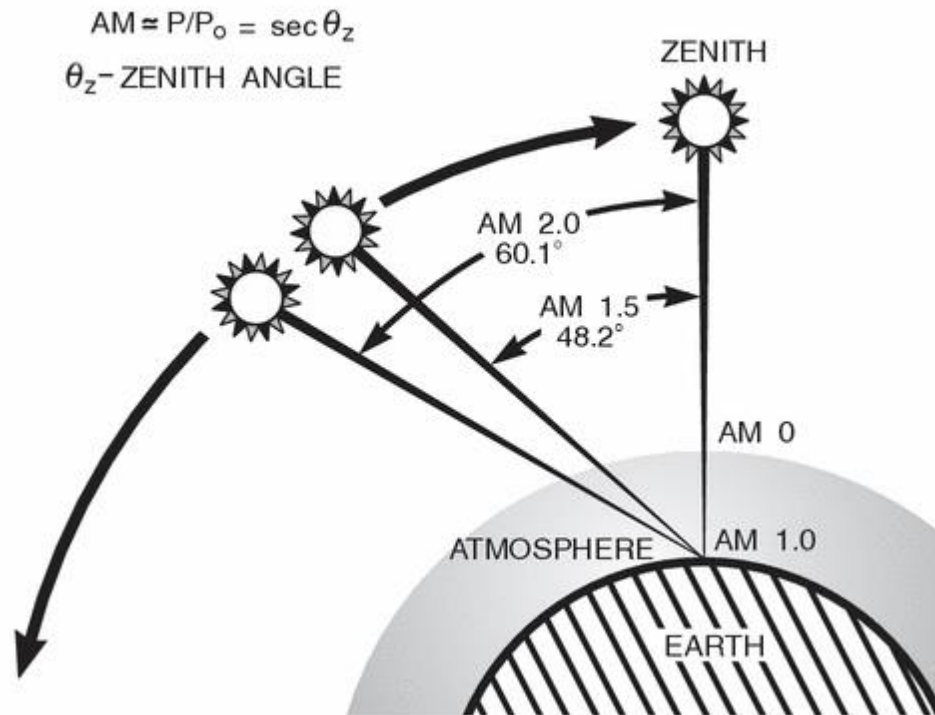


Figure 2.5: AM: Air Mass index (Newport, 2016).

The standard spectrum at the Earth's surface is called AM1.5G, where G represents global in the sense that it includes both direct and diffuse radiation. The standard spectrum outside the Earth's atmosphere is called AM0 meaning zero atmosphere. AM1 is defined as the spectrum after traversing through the atmosphere to the sea level having the sun directly overhead. AM1 may also be referred to as one atmosphere and the sunlight traverse the least possible amount of atmosphere and AM2 refers to a situation whereby sunlight has to traverse twice as much atmosphere as it does in AM1. AM2 is the atmospheric path length observed at a solar zenith angle of  $60^\circ$  (Duffie & Beckman, 2013). The AM1 intensity of solar radiation is approximated as  $1000 \text{ W/m}^2$  which is a reduction of about 30% of the intensity of the solar constant for earth which is  $1367 \text{ W/m}^2$  (Messenger & Ventre, 2010).

The solar irradiance available at the top of the atmosphere is called the extraterrestrial radiation (ETR). The solar ETR is continuously filtered by the earth's atmosphere as it passes through to

the surface. Fig 2.6 below shows absorption of solar radiation by ozone, oxygen, water vapour and carbon dioxide as it passes through the atmosphere ( Stoffel, et al., 2010). The major elements that modify the extraterrestrial solar radiation are weather systems that include clouds and storms. Nevertheless, even cloudless atmosphere may contain particles that reduce the ETR which are gaseous molecules, dust, aerosols and particulates. These systems reduce the radiation through absorption and scattering ( Stoffel, et al., 2010).

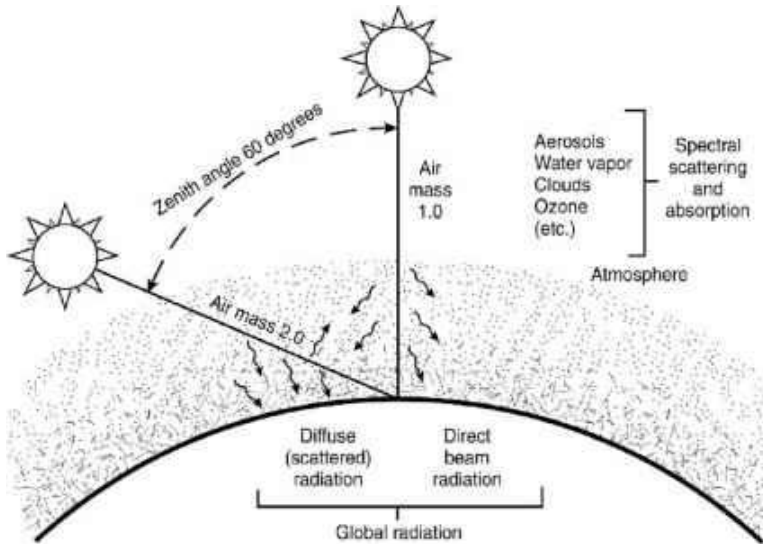


Figure 2.6: Scattering of the direct-beam photons from the sun by the atmosphere produces diffuse radiation that varies with AM ( Stoffel, et al., 2010).

Terrestrial radiation is the long-wave (wavelength is from 4 to 40  $\mu\text{m}$ ) electromagnetic energy emitted by the Earth's surface and by the gases, aerosols and clouds of the atmosphere; it is also partly absorbed within the atmosphere. The incoming extraterrestrial irradiation mainly interacts with the following atmospheric components as it passes through the atmosphere, the different gasses, (counting water vapour), the dense water beads and different mist concentrates which assimilate short wave radiant energy or disseminate it [63]. The association of approaching extraterrestrial radiation is shown in Fig 2.7. To be more exact the accompanying happens:

- Absorption by gas particles, pressurised canned products and dense water represents 20% of the energy loss resulting in warming of the environment.

- Rayleigh scattering joined with back reflection fundamentally from mists sends 26% of the approaching sun oriented vitality straightforwardly again into space.
- Just 54% of the primary incoming solar energy make its way to the ground.
- Beam radiation reaches the ground which is 30% of the incoming extraterrestrial energy.

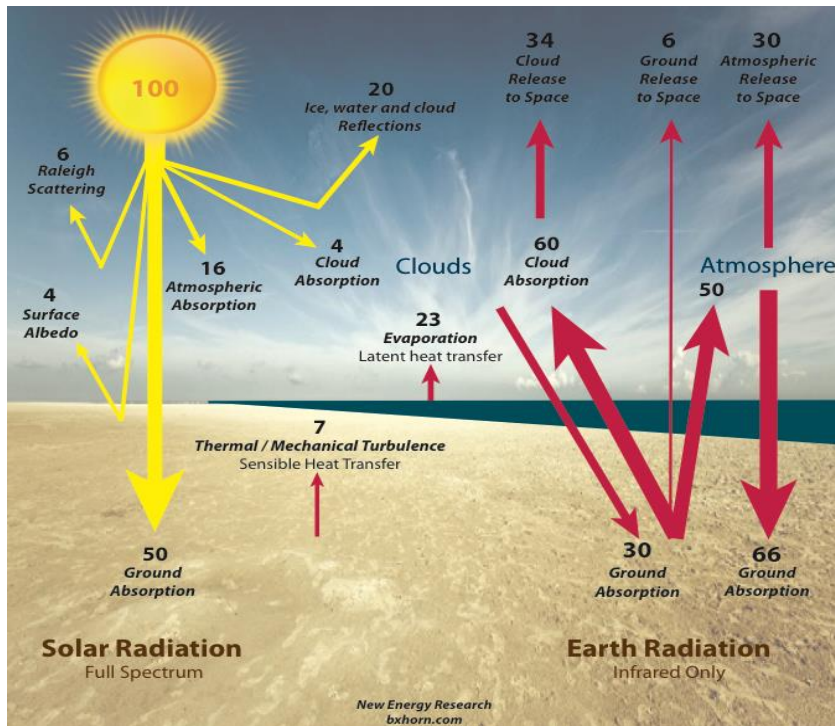


Figure 2.7: Radiation balance of the atmosphere (Falayi & Rabiou, Solar radiation models and information for renewable energy applications, 2012).

An increase in path length (AM) results in more scattering and more ingestion of solar radiation. Additionally, some portion of radiation that makes it to the ground is reflected back into the atmosphere. The real geometry and flux density of the reflected and scattered radiation is ascribed to the reflectivity and physical properties of the ground and constituents in the air (Stoffel, et al., 2010).

The short wave energy (wavelength of radiation extending from 0.1  $\mu\text{m}$  and 5.0  $\mu\text{m}$ ) that reaches the Earth's surface after absorption and dispersion have happened is known as global irradiation. It is impacted by the path length through the sky, clearness of the sky, overcast spread coefficient and cloud sort. The interaction of the sun based radiation and the air includes complex

procedures (Scharmer & Greif, 2000). Thus, to streamline comprehension of the part of the air, the energy balance between the atmosphere, the surface of the earth and approaching sun powered radiation can be isolated into three unique procedures (Scharmer & Greif, 2000):

- Absorption and scattering of incident radiation to the atmosphere before achieving the ground.
- Thermal radiation emanating from the ground and atmosphere.
- Non-radiative warmth and vitality transport forms in the climate and amongst ground and the environment.

Incident solar radiation can be transmitted, absorbed or scattered by varying amounts proportional to their wavelengths as shown in Fig 2.8. The sophisticated interaction of the solar radiation-atmosphere system results in three key broadband parts namely *DNI*, *DHI* and *GHI* (Stoffel, et al., 2010).

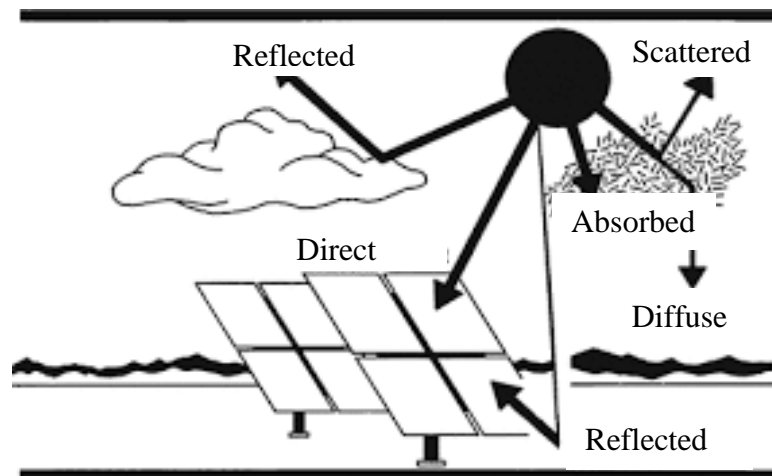


Figure 2.8: Scattering of the direct-beam photons from the sun by the atmosphere (Stoffel, et al., 2010)

*DNI* incorporates the forward-scattered radiation close to the solar disk. The impact of this scattering is not constant, but it varies depending on the composition of the atmosphere when it

is observed. The earth's surface and local clouds play a big role in reflecting part of the incident *DNI*. The optical properties of the surface determine the magnitude and direction of the reflected radiation. However, some of the incident radiation may be reflected upwards into the sky where reflection and scattering may take place again resulting in an increase in the diffuse radiation component ( Stoffel, et al., 2010).

If the sky is free of clouds, it assimilates and scatters radiation as the *DNI* enters the ground. Absorbed radiation is converted into internal energy, whereas the reflected radiation will be scattered in many other directions different to that of the beam radiation. The scattered radiation is known as the *DHI* ( Stoffel, et al., 2010). The horizontal global solar radiation is a total of the *DNI* at a solar zenith angle plus the *DHI* as follows ( Stoffel, et al., 2010):

$$GHI = DNI \cdot \cos(SZA) + DHI \quad (2.4)$$

*SZA* is the solar zenith angle at a particular area. This central condition is the premise of most sunlight based radiation estimation framework plans, information quality appraisals, and atmospheric radiative exchange models tending to the requirements for sun oriented asset information ( Stoffel, et al., 2010).

It is known that there are many factors that affect UV (100 nm – 400 nm) (Mateos, Bilbao, de Miguel, & Pérez-Burgos, 2010) radiation reaching the earth's surface. However, clouds are still outstanding in as much as influencing UV radiation reaching the surface is concerned. To be more precise, the degree by which the clouds scatter, reflect and absorb solar radiation depends on their size, shape and composition. Furthermore, their composition determines their optical thickness, which may lead to the warming or cooling effect caused by the clouds. However the way clouds regulate the amount of solar radiation reaching the ground is not as easy to interpret quantitatively as it seems due to the challenge in measuring their radiative properties either from the ground or satellites (Pfister, McKenzie, Liley, Thomas, Forgan, & Long, 2003). It is still a challenge to quantify the effects of clouds on solar radiation due to the scarcity of parameters that can be used to calculate this effect. These challenges seem to be unsolvable since clouds have a complex geometry that requires being specified sufficiently using 3-D model calculations ( Cebecauer, Skoczek, Betak, & Suri, 2011). Even though clouds may be of the same type they

attenuate solar radiation at different levels depending on their micro and macro-physical properties (Buch, Jr, Sun, & Thorne, 1995). The macro-physical properties include cloud cover and its geometry (Pfister, McKenzie, Liley, Thomas, Forgan, & Long, 2003) whereas the micro-physical properties include the amount of condensed water, the size and shape of the cloud particles and the phase of the particles (Curry, Rossow, Randall, & Schramm, 1996). This study focuses on the effect of clouds (as the main factor that attenuates solar radiation) on the radiometer measurements in the Durban area.

## **2.2 Sun-Earth geometry**

Taking the earth as the frame of reference, the sun rotates on its axis on average once every 4 weeks. However, its rotation is not that of a solid body, but different regions take a different period to complete the cycle of that particular rotation. The region on the equator takes about 27 days and the polar regions takes about 30 days for each rotation. When the earth is rotating it means it will be spinning on its axis. The earth's complete rotation takes exactly twenty four hours and is referred to as a mean solar day. It is these rotations that dictate the daily cycles of day and night. The apparent movement of the sun across the horizon is created by the earth's rotation. The orbit of the earth around the sun is called an earth revolution. A complete cycle of this celestial motion takes precisely 365.26 days. The actual path defined by this orbit is elliptical in shape as shown in Fig 2.9. It is because of this elliptical orbit that makes the sun-earth distance to vary over a year but not necessarily responsible for the earth's seasons. This variation in the earth-sun distance is also responsible for the variation in the solar radiation received on the earth's surface by 6% annually. Figure 2.9 shows the positions in the earth's revolution where the sun is closest and furthest away from the earth. The earth is closest to the sun on January 3, perihelion, when it is 147.3 million km. alternatively the earth is furthest from the sun on July 4, aphelion, when it is 152.1 million km. The average distance of the Earth from the Sun over a one-year period is about 149.6 million km (Pidwirny, 2006).

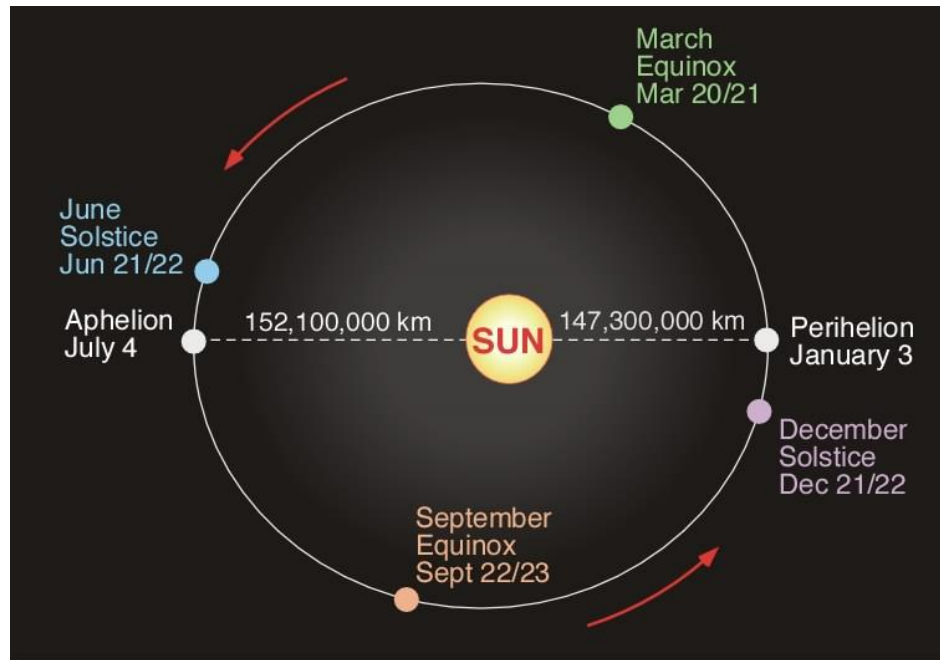


Figure 2.9: Position of the equinoxes, solstices, aphelion, and perihelion relative to the Earth's orbit around the Sun (Pidwirny, 2006).

On the off chance that data on sun based radiation in a particular area and time is required, it is fundamental to know about the geometrical parameters portraying the position of the sun as observed from the earth. The three essential parameters that are required to decide the position of the sun on the earth's point of view are as per the following (Scharmer & Greif, 2000):

- The latitude of site of perception.
- The Julian day number.
- The season of day communicated as an hour angle.

The Latitude of the site of observation is represented by  $\varphi$  and it can be defined as the angular location of the site, with positive for north and negative for south of the equator, ( $-90^\circ \leq \varphi \leq 90^\circ$ ) (Sahin & Sen, 2008). The key count contribution to create the sun oriented geometry is the declination. Augustine and Nnabuchi (2010) define the declination angle  $\delta$  as, "The edge between the Equatorial Plane and the line joining the focal point of the Earth's circle to the focal point of the sun based plate" (Aug10). The accompanying declination point recipe is utilised for figuring the declination edge  $\delta$  (Aug10):

$$\delta = 23.45 \sin \left[ \frac{360(N+284)}{365} \right] \quad (2.5)$$

where  $N$  is the day of the year.

The day number of the year was computed from the following equations (Scharmer & Greif, 2000):

Table 2.1: The day number  $N$  corresponding to the  $i$ -th day of the month

	$N$ for $i^{\text{th}}$ day of month	Leap year
January	$i$	
February	$31 + i$	
March	$59 + i$	(+1)
April	$90 + i$	(+1)
May	$120 + i$	(+1)
June	$151 + i$	(+1)
July	$181 + i$	(+1)
August	$212 + i$	(+1)
September	$243 + i$	(+1)
October	$273 + i$	(+1)
November	$304 + i$	(+1)
December	$334 + i$	(+1)

The hour angle,  $\omega$ , is the angular displacement of the sun east or west of the local meridian due to rotation of the earth on its axis at  $15^\circ$  per hour as morning negative and afternoon positive (Sahin & Sen, 2008). The time of day is used to calculate the hour angle  $\omega$  as follows (Scharmer & Greif, 2000), expressed as an hour angle from solar noon:

$$\omega = 15(t - 12) \text{ degrees} \quad (2.6)$$

where  $t$  is the time in hours on the 24 hour clock (using Local Apparent Time).

Sahin *et al.* (2008) define the solar constant ( $I_{sc}$ ) as, “An equivalent to the energy from the sun, per unit time, received on a unit area of a surface perpendicular to the direction of propagation of the radiation, at mean earth-sun distance, outside of the atmosphere” (Sahin & Sen, 2008). It has

been adopted as  $1367 \text{ W/m}^2$ . Recently this value is estimated at  $1366.1 \text{ W/m}^2$  that covers the solar spectrum between 0 and  $1000 \mu\text{m}$  (Sahin & Sen, 2008).

These parameters described above are important as they play an important role in computing the extraterrestrial radiation that will be used in determining the clearness index of a specific place. The values of the clearness index are used in correlating them with the values of the cloud cover so as to determine their correlation coefficient and correlation of determination. In this regard, the relationship between the radiometric measurements and cloud fraction in Durban will be established through correlating the clearness.

# Chapter 3

## Solar radiometry instruments and the Total Sky Imager

Radiometry is referred to as the science of electromagnetic radiation measurement (Paulescu, Paulescu, Gravila, & Badescu, 2013). In practice, radiometry is usually limited to the measurement of infrared, visible, and ultraviolet light using optical instruments (Ashdown). Radiometers generally used for observation are pyrheliometers and pyranometers that measure direct solar radiation and global solar radiation respectively. A radiometer uses its sensor to absorb solar radiation, which it transforms into heat and the resulting amount of heat gives an equivalent amount of solar radiation depending on its calibration. There are two methods of measuring heat. The first method of measuring heat involves taking out heat flux as a temperature change (using a water flow pyrheliometer, a silver-disk pyrheliometer or a bimetallic pyranograph) or as a thermo-electromotive force (using a thermo-electric pyrheliometer or a thermo-electric pyranometer) (Measurement of Sunshine Duration and Solar Radiation). Generally, the radiometer types that are in current operation are those that use a thermopile. To study the relationship between solar radiation and cloud cover, a TSI need to be used in conjunction with the radiometers.

In this chapter, a brief history and general information of the related instruments that were used is given. Furthermore, the information on the specific instruments that were used in this research work is explained immediately after the subsequent general information. The specific types of pyranometers and pyrheliometers that were used are explained, their internal structures and their principle of operation. Kipp and Zonen shaded and unshaded pyranometers and Kipp and Zonen Normal Incidence Pyrheliometer (NIP) were used and thus will be explained further. The TSI

440A was used for obtaining the cloud cover, hence its internal structure and principle of operation will be detailed in the subsection that is after the general information on Total Sky Imagers. The decision algorithm that is employed by the TSI 440A will also be explained in the subsection of TSI 440A.

### **3.1 Pyrheliometers**

As previously mentioned, a pyrheliometer is used to measure direct solar radiation from the sun and its marginal periphery. The orientation of its surface is such that it must be normal to the solar direction; hence it is normally mounted on a tracker to achieve this orientation. There are mainly three groups of pyrheliometers namely the Angstrom electrical compensation pyrheliometer, a silver-disk pyrheliometer and a thermo-electric pyrheliometer. Detailed information of the mentioned pyrheliometers is given below (Measurement of Sunshine Duration and Solar Radiation).

#### **Angstrom electrical compensation pyrheliometer**

The Angstrom electrical compensation pyrheliometer is viewed as a solid instrument (Garg & Garg, 1993) that can be utilised as a working standard despite the fact that its manual operation needs someone familiar with it (Measurement of Sunshine Duration and Solar Radiation). This pyrheliometer comprise of a rectangular gap, two manganese-strip sensors ( $20 \text{ mm} \times 2 \text{ mm} \times 0.02 \text{ mm}$ ) with many diaphragms (Measurement of Sunshine Duration and Solar Radiation), its diaphragms being similar to those of the other previously mentioned pyrheliometers. To ensure optimum uniform absorption of short-wave radiation its sensor surface is painted optical black. At the rear of each sensor strip there is a copper-constantan thermocouple attached and this thermocouple is likewise associated with a galvanometer. Heat is generated by the sensor strips when current moves through them since they likewise fill in as electric resistors. At the point when measuring sun based irradiance the little screen on the front face of the chamber obstruct one sensor from daylight, so that daylight just reaches one sensor and ingests solar radiation. Because of this impact, the resulting contrast in temperature delivers a thermo-electromotive power that is relative to this distinction which induces current through the galvanometer. This current heads to the cooler shaded sensor strip until the pointer of the galvanometer focuses zero

and subsequently this is the point whereby the temperature resulting from solar radiation is compensated by Joule heat. Through the instrument's calibration, a value for direct sun powered irradiance is obtained from changing over the compensated current at particular times. In the event that  $S$  is the intensity of direct sunlight based irradiance and  $i$  is the current, then (Measurement of Sunshine Duration and Solar Radiation):

$$S = Ki^2 \quad (3.1)$$

where  $K$  is the constant intrinsic to the instrument and is derived from the size and electric resistance of the sensor strips together with the absorption coefficients of their surfaces. The Angstrom electrical compensation pyrheliometer with its electrical schematic diagram is shown in Fig 3.1.

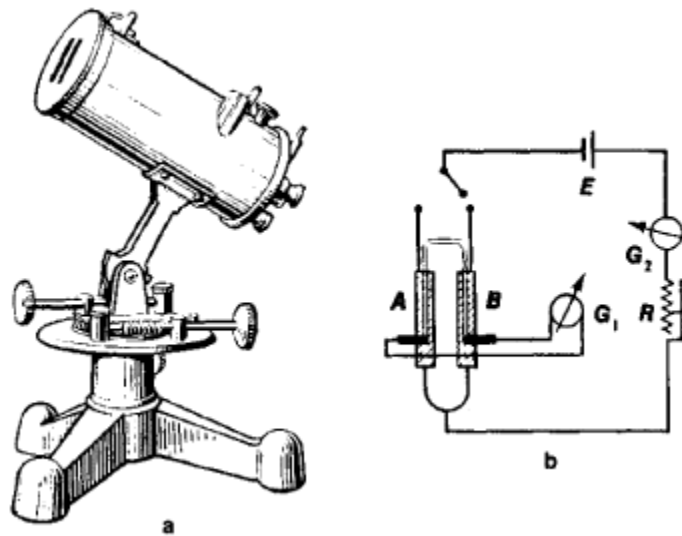


Figure 3.1: Angstrom pyrheliometer (a) external view, (b) schematic of the instrument, ( $G_1$ ) and ( $G_2$ ) galvanometers, ( $R$ ) rheostat regulating the strength of the compensation current (The Great Soviet Encyclopedia, 1970-1979)

### Silver-disk pyrheliometer

This instrument was designed by Abbot in 1902 at the Smithsonian Institution and was used as a secondary standard for radiation measurements (Garg & Garg, 1993). This instrument might be

viewed as a compact variant of a water stream pyrliometer which was the previous essential standard (Measurement of Sunshine Duration and Solar Radiation). This instrument detects utilising a silver plate having a diameter of 28 mm and a thickness of 7 mm. The side that receives radiation is painted in black colour. It has a gap from the periphery towards the centre that acts as housing for a knob of a high accuracy mercury-in-glass thermometer. This gap is loaded with a little measure of mercury in order to maintain good thermal contact between the circle and the globule. On the outside it is encased by a warmth protecting compartment. The stem of the thermometer is bowed at a right edge outside the wooden holder and upheld in a metallic defensive tube. To guarantee direct solar radiation falls onto the plate, a barrel with diaphragms inside is fitted into the wooden holder. To make sure that direct solar radiation falls onto the disk, a tube with diaphragms inside is fitted into the wooden container. To gauge the direct sun oriented radiation, the circle is warmed by sun based radiation and its temperature rises. The force of this radiation is found out by measuring the temperature difference of the circle between the estimation stage and the shading stage with the mercury-in-glass thermometer. Fig 3.2 shows a Silver-disk pyrliometer.

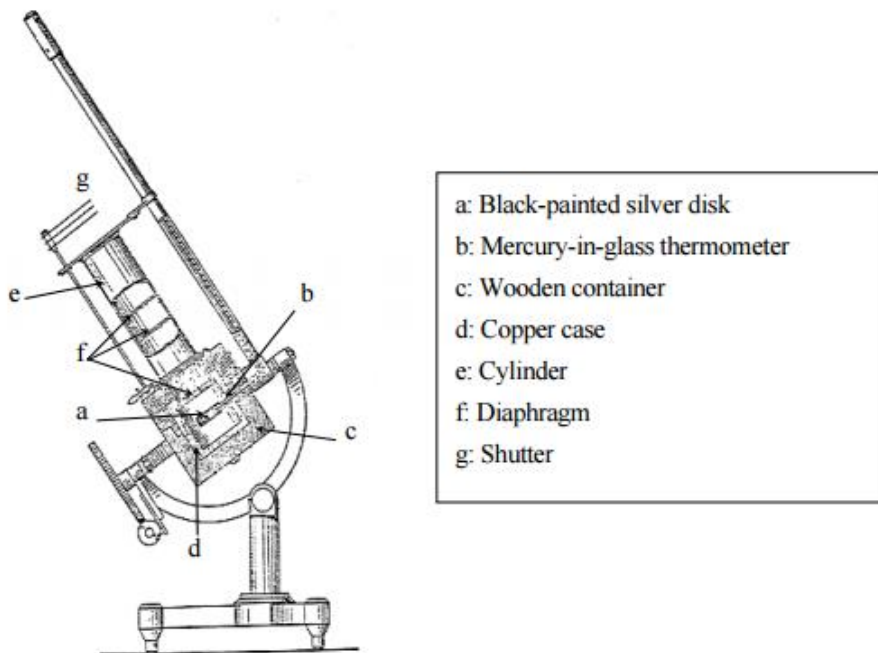


Figure 3.2: Silver-disk pyrliometer (1608).

## Thermo-electric pyrheliometer

The sensing unit of this instrument is a thermopile and it consistently conveys a thermo-electromotive power in extent to the direct sun powered irradiance (Measurement of Sunshine Duration and Solar Radiation). This kind of instrument has a see-through optical glass in the gap to make it reasonable for use in every single climate condition like the previously mentioned sorts that have a housing that permits the external air to be in direct contact with the sensor bit. In order to establish an outdoor automatic operation this instrument is mounted on a sun-tracker. Even though there are different types of thermo-electric pyrheliometers but their structures are similar. An example is the thermo-electric pyrheliometer used by the Japan Meteorological Agency (JMA). Fig 3.3 shows a cross-section of the Eppley NIP instrument.

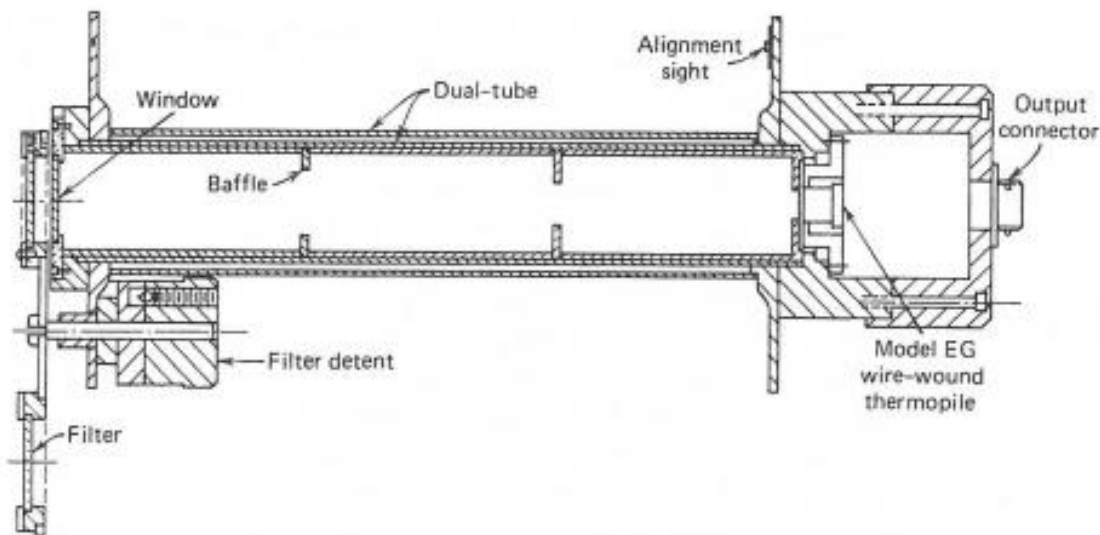


Figure 3.3: Cross section of the Eppley NIP (16081).

In this instrument, the copper-plated constantan wire is utilised as the thermopile as a part of the sensor component and is connected to the base of the barrel at right angle to the chamber hub. Diaphragms fit to the chamber to guide the daylight to the sensor bit. The barrel is made of a metallic piece with high heat capacity and good thermal conductivity. It is encased in a polished middle chamber and a silver-plated external metal barrel with high reflectivity to avoid fast changes in surrounding temperature or keep external wind from disturbing the heat flux in the

radiation-detecting component. Condensation on the inside of the aperture window is prevented by a desiccant that keeps the cylinder dry. To measure the direct solar irradiance, a temperature contrast is created between the sensor surface normally referred to as the hot intersection and the reference temperature point, i.e. the metallic square of the inward barrel normally referred to as the cold junction (Measurement of Sunshine Duration and Solar Radiation). Since the temperature distinction is corresponding to the power of the radiation consumed, the level of sun oriented radiation can be inferred by measuring the thermo-electromotive force off the thermopile. However, this instrument is not a standard instrument, alignment ought to be performed with a standard instrument to determine the instrumental factor. The temperature inside the barrel ought to be observed to monitor and correct the instrument since the thermo-electromotive power yield relies upon the unit's temperature.

### **3.1.1 Kipp and Zonen Normal Incidence Pyrheliometer (NIP)**

Direct solar radiation received at a particular location is measured using a pyrheliometer. It measures the nearly collimated radiation within a narrow field of view, typically between  $5.0^\circ$  and  $5.8^\circ$  (Sabburg & Wong, Evaluation of sky/cloud formula for estimating UV-B irradiance under cloudy skies, 2000b). The Absolute Cavity Radiometer (ACR) is used to calibrate other pyrheliometers since it is of higher class. In this work, a Kipp and Zonen Normal Incidence Pyrheliometer (NIP) was used for obtaining DNI measurements. The angle of aperture of the instrument is  $5.0 \pm 0.2^\circ$  and its sensitivity is approximately  $7.4 \mu\text{V}/\text{Wm}^{-2}$  (Marquez, Gueorgulev, & Coimbra, 2011). The pyrheliometer was mounted onto the solar tracker which constantly follows the sun so as to continuously measure the direct solar radiation. There are different types of solar trackers: passive, microprocessor and electro-optically controlled while the microprocessor-based tracker is considered to have a higher level of accuracy compared to the passive and electro-optical systems. The axis of rotation, whether one axis of rotation, or two axes of rotation can further classify the trackers' category (Nimnuan & Janjai, 2012). Commonly used solar trackers are Eppley's ST-1 or ST-3, Solys and BRUSAG's INTRA. The Kipp and Zonen pyrheliometer was mounted onto a Solys 2 tracker as shown in Fig 3.4.

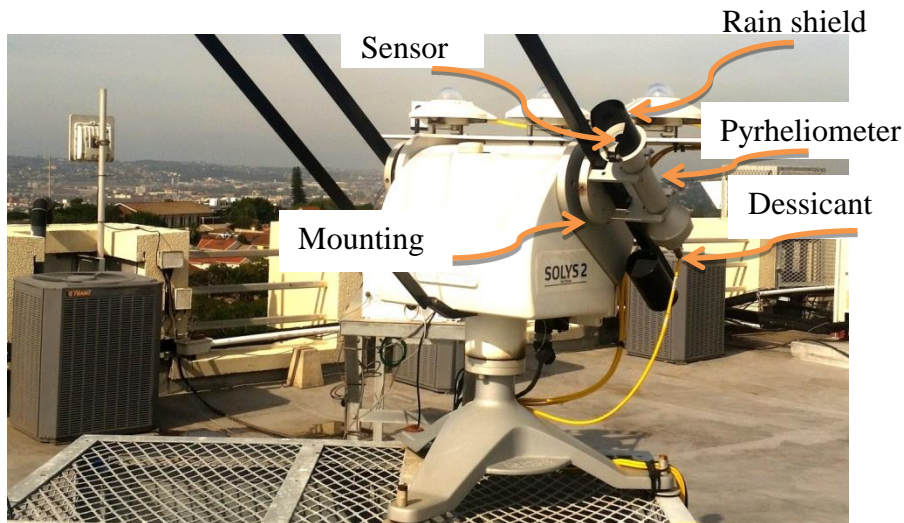


Figure 3.4: Pyrheliometer mounted onto the Solys 2 tracker measures the DNI component.

### 3.2 Pyranometers

A pyranometer is an instrument that is used to measure global solar radiation falling on a horizontal surface. Its sensors consist of a horizontal radiation-sensing surface that absorbs solar radiation energy from the whole sky, which is transformed into heat energy (Measurement of Sunshine Duration and Solar Radiation). The heat energy will be proportionally quantified to give the corresponding global solar radiation. The two types of pyranometers generally used are the thermopile type and the bimetallic pyranometers.

#### Thermo-electric pyranometers

The instrument's radiation-detecting component has a structure fundamentally similar to that of a thermo-electric pyrheliometer (Measurement of Sunshine Duration and Solar Radiation). The other common similarity of this instrument with the latter is that the temperature distinction inferred between the radiation-detecting component (the hot intersection) and the reflecting surface (the chilly intersection) which is used as a temperature reference point is communicated by a thermopile as a thermo-electromotive power. In a pyranometer, numerous sets of thermocouples are joined in series arrangement to make a thermopile that identifies the temperature distinction between the black and white radiation-detecting surfaces. The thermopile recognises the temperature contrast between a radiation-detecting surfaces painted strong dark

and a metallic piece with high warmth limit. Fig 3.5 shows a diagram of a thermo-electric pyranometer.

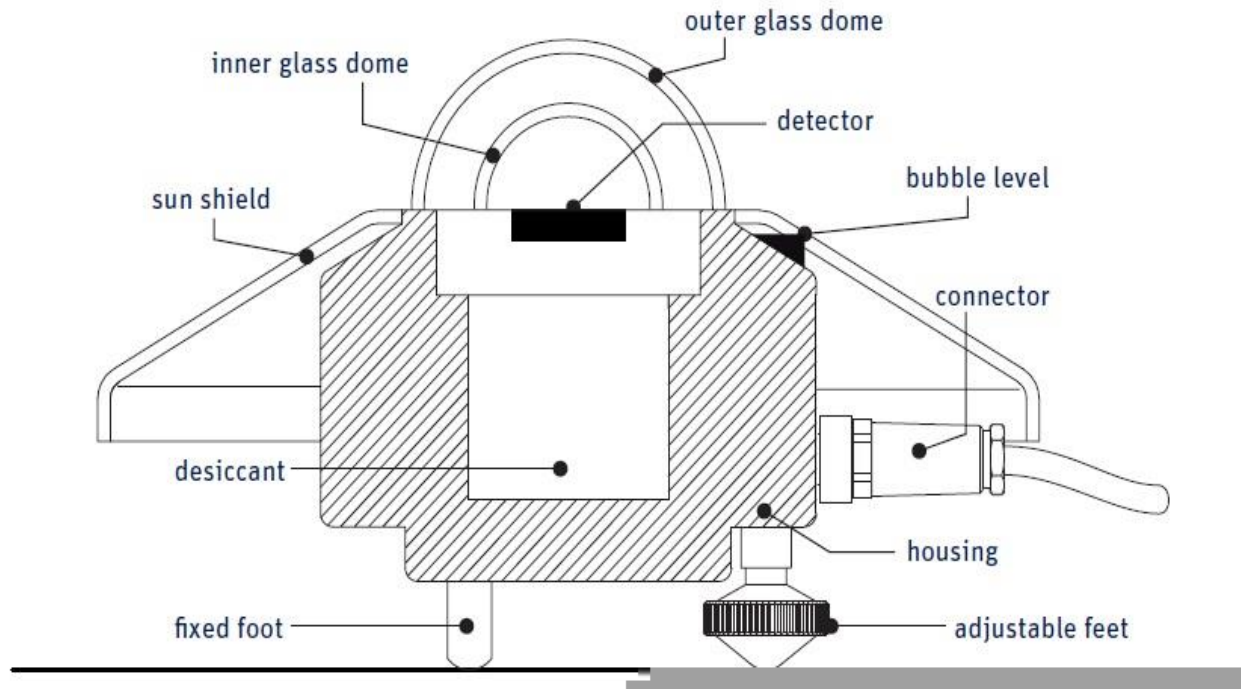


Figure 3.5: Thermo-electric pyranometer (16082).

### A bimetallic pyranograph

The radiation-detecting component is comprised of two sets of bimetals, one painted dark and the other one painted white, put in inverse headings, one confronting up and the other confronting down, and they are joined to a typical metal plate toward one side (Measurement of Sunshine Duration and Solar Radiation). The white bimetallic strips are settled to the casing of the pyranograph at the flip side and the dark ones are associated with the recorder area through a transmission shaft. Through an amplifying framework, the recording pen receives signals from the unpinned edge of the black strips through deflection. At the point when the air temperature changes, the high contrast strips joined to the basic plate toward one side, both curve by the same extent yet in inverse bearings, subsequently just the temperature distinction credited to sun based radiation is transmitted to the recording pen. Its normally used for observing the daily total

irradiance due to its strength of being sturdy and it does not need electrical power supply for it to operate hence it is suitable for remote areas (Garg & Garg, 1993).

Similarities on these two pyranometers is that they are both hermetically fixed in a glass arch to shield the sensor part from wind and rain and furthermore keep the sensor surface temperature unresponsive to disturbances brought about by wind (Measurement of Sunshine Duration and Solar Radiation). To avoid build-up of water molecules on the internal surface a desiccant is put in the vault. Solar radiation of wavelengths in the range of 0.3 to 3.0  $\mu\text{m}$  which constitute much of the solar radiation energy is allowed to pass through by the glass. Some models consist of a fan that prevents dust and frost to settling on the dome's outer surface since it significantly affect the amount of light received. It's therefore of utmost importance to regularly clean the glass surface to allow constant passage of solar radiation. Fig 3.6 shows a bimetallic pyranograph.

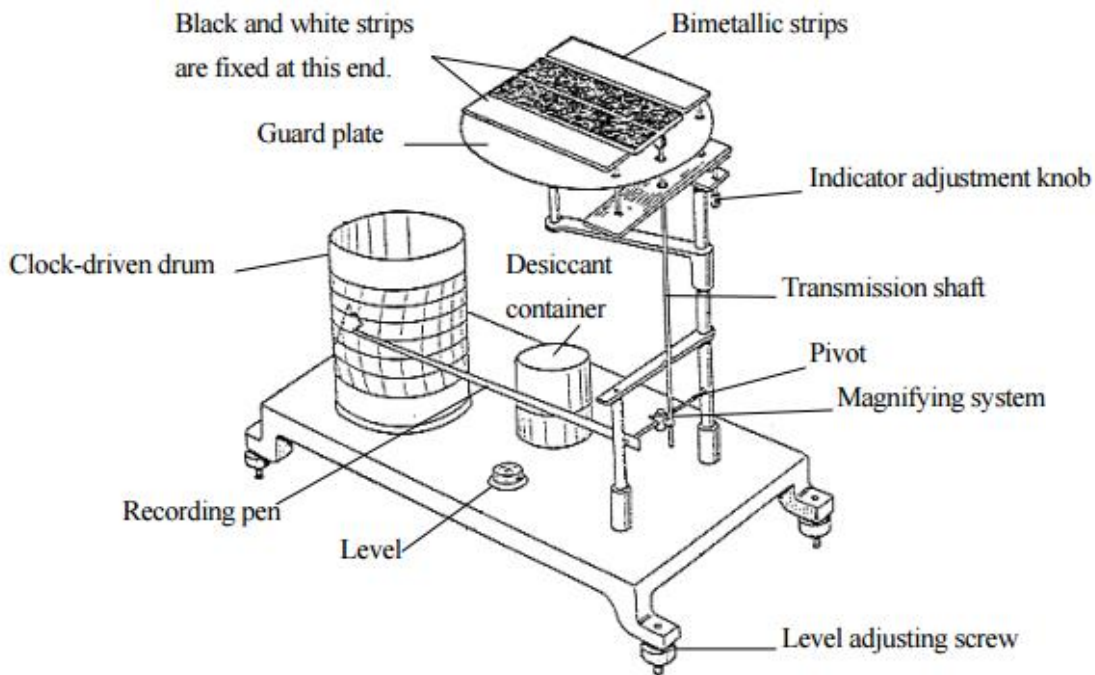


Figure 3.6: Bimetallic pyranograph (1608).

### 3.2.1 Kipp and Zonen shaded and unshaded pyranometers

Pyranometers are used to measure global and diffuse solar radiation. They measure the incident solar radiation that within the solid angle of  $2\pi$  to them. For this research, the Kipp and Zonen shaded and unshaded pyranometers used to measure the diffuse and direct components respectively have sensitivity values of  $9.1$  and  $9.3 \mu\text{V}/\text{Wm}^{-2}$  respectively, and are shown in Fig 3.7. It consists of a copper-constantan thermopile sensing element that converts the temperature to a voltage and it is housed in a domed structure.

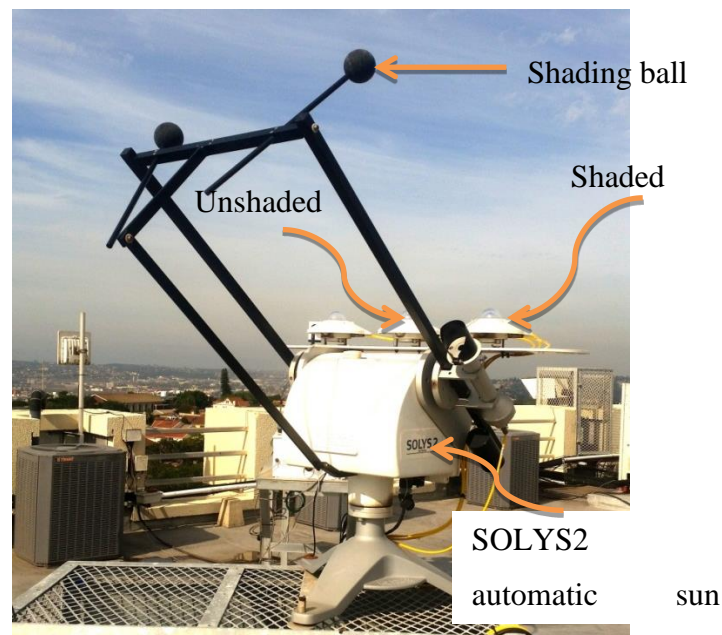


Figure 3.7: Shaded and unshaded pyranometers mounted on a stationary plate on top of the Solys 2 tracker.

The dome cover is used to shield the sensing element from dust, wind and rain since these factors may affect its temperature. However, the dome allows transmission of the solar radiation from all directions equally. Measurement of the diffuse component can be achieved by the use of a shadow band or shading ball blocking the passage of the direct solar radiation to the sensing element so that only the scattered radiation can be received by the sensor. Nonetheless, if the direct and global components are known the diffuse component can be calculated using equation (2.4).

### 3.3 Sky Imagers (SI's)

The hardware used for sky imaging dates back to the twentieth century ( Urquhart, Ghonima, Nguyen, Kurtz, Chow, & Kleissl, 2013). The development of a fisheye lens made a great contribution to the development of sky imaging tool. Hill (1924) made the first true modern fisheye lens by making use of a large negative-meniscus front element in the lens, allowing the full sky to be in a focus (Hill, 1924). The evolution of sky imagers was made possible by the development of digital systems utilizing computers and semiconductor sensors which started in the 1980s. Some work was done by different communities utilizing these ideas and the Scripps Institute of Oceanography (SIO) is one of them that developed a system designed for cloud imaging. The SIO's Marine Physical Laboratory (MPL) developed the Whole Sky Imager (WSI) in the 1980s and 1990s for US military applications. Whole sky imagers (WSI) are designed to measure irradiances at different wavelength bands across the hemisphere. The WSI models include a high temperature controlled charge-coupled device (CCD), high quality optics including spectral filtering and detailed mapping of the sky dome to CCD element. The WSI has many interesting scientific capabilities and it can also be used to estimate fractional sky cover (Tooman, 2003). The WSI cloud retrieval classifies sky elements as belonging to one of the following eight defined categories depending on the ratio of measured radiance to that of expected for the same element in an exceptionally clear sky. The eight categories are as follows: clear, aerosol, mixed aerosol and cloud, bright clouds, intermediate cloud, dark cloud, indeterminate and undefined (Slater, Long, & Tooman, 2001). The high cost of WSI makes them to be unpopular among meteorological researchers (Huo & Lu, Cloud determination of all-sky images under low-visibility conditions, 2009). The high costs are highly contributed by the high quality components and complex engineering involved in manufacturing them. Another popular sky imager to the researcher is the TSI manufactured by the Yankees Environmental Systems Inc. (YES).

The famous TSI evolved from a Hemisphere Sky Imager (HSI) which is a prototype. Long and Deluissi first described the system of a TSI as an HSI in 1998 (Long & DeLuissi, Development of an automated hemispheric sky imager for cloud fraction retrievals., 1998). The HSI was developed at the National Oceanic and Atmospheric Administration Surface Radiation Research

Branch (SRRB) located in Boulder, Colorado. It was through a joint effort between US Department of Energy's Atmospheric Radiation Measurement (ARM) Program and Yankees Environmental Systems Inc. (YES) that resulted in rebranding of a HIS into a commercial product named TSI. The HIS and TSI consists of a rotating mirror that reflects the sky onto the camera that is mounted pointing downwards. This mirror is always rotating and consists of a dull strip that is always blocking direct sun from damaging the camera consequently by always being aligned to the sun. The rotation of the mirror is enabled by the mounted on-board computer. The TSI camera captures images of the sky during the daytime and the rate at which images are captured can be set by the user. The raw sky images are processed to establish the fractional sky cover (Long, Sabburg, Calbo, & Pages, Retrieving cloud characteristics from ground-based daytime color all-sky images., 2006). However, its system has a relatively low resolution and also there are fewer options in the capturing settings.

Other sky imager systems are described below. Long *et al.* (2006) described the Whole Sky Camera (WSC) which was developed by the University of Girona in Spain (Long, Sabburg, Calbo, & Pages, Retrieving cloud characteristics from ground-based daytime color all-sky images., 2006). Its CCD is about a third of the normal size with  $752 \times 582$  pixels and consists of a fish eye lens with a focal length of about 1.6 mm. Its shadowband needs to be adjusted to match site latitude and declination. Carzola *et al.* (2008) in their first document discussed the All-Sky imager developed at the University of Granada in Spain (Carzola, Olmo, & Alados-Arboledas, 2008a). It has a QImaging RETIGA 1300C camera that uses a Sony ICX085AK 2/3 inch thermoelectrically cooled CCD image sensor that captures 36-bit images (Carzola, Olmo, & Alados-Arboledas, 2008a). It used a Fujinon fish eye lens which is shaded from direct sunshine by a shadowball. The camera system ensemble is housed in a weatherproof casing with a sun tracking system. Lu *et al.* (2001) discussed on the all-sky imager ASI developed by the Institute of Atmospheric Physics, Chinese Academy of Sciences (Lu, Huo, & Lu, 2001). Its digital camera also has a fisheye lens to capture all-sky images (JPEG format and  $2272 \times 1704$  resolution) (Huo & Lu, Comparison of cloud cover from all-sky imager and meteorological observer, 2012). The CCD sensor is protected from direct sunlight. ASI takes images from sunrise to sunset at 3 minutes interval daily. Kalisch and Macke (2008) discussed the high-resolution camera developed by the Leibniz Institute of Marine Sciences at the University of Kiel

in Germany (IFM-GEOMAR) (Kalisch & Macke, 2008). This camera has no shading devices like others and its design was specifically meant to cater for shipboard sky photography. It uses a  $3.648 \times 2.736$  CCD image sensor that captures 30-bit colour images in JPEG format.

Sebag *et al.* (2008) discussed the All Sky Infrared Visible Analyser (ASIVA) developed by Dimitri Klebe of the Denver Museum of Natural Science (Sebag, Krabbendam, Claver, Andrew, Barr, & Klebe, 2008). Unlike the TSI which use the reflection-based method for sky imaging, the ASIVA is one of the rare longwave-infrared (LWIR) that is refraction-based. It uses a  $640 \times 480$  uncooled microbolometer array that range from 8 – 12  $\mu\text{m}$ . It consists of a customized germanium fisheye lens. It has a visible-range CMOS dual camera with high resolution. Dye (2012) discussed the high-dynamic- range all-sky-imaging system (HDR-ASIS) developed by the U.S Geological Survey (Dye, 2012). It consists of a CMOS-based camera that produces an HDR composite image. However, there are still new developments going on in the field of sky-imaging especially on the systems. The sky imager that will be used for this research work is the Total sky imager and hence its detailed information is explained below.

### **3.3.1 Total Sky Imager**

The TSI is an instrument that provides time series of hemispheric sky images during the daytime and they provide retrievals of fractional sky cover for solar elevation greater than 10 degrees. They provide a visual record of sky conditions showing sun obscuration by clouds (using their inbuilt sunshine meter) and quantify the fractional sky cover as percentages, but specifying if the clouds covering the sun are thin or opaque. The instrument operation is automatic and its images are in full-colour. Sky images are captured via a solid-state charge-coupled device (CCD) that is facing down into the heated and a rotating hemispherical mirror or dome. There is a filament under the dome provides heating to evaporate any moisture on the dome surface (Sabburg & Long, 2004). The imager optics of the camera is always protected by a rotating shadowband that is always aligned so as to prevent it from the intense direct light from the sun. The instrument has an image-processing algorithm that captures and displays the images. The camera, its arm and the sun-blocking shadowband are first masked out before the software starts analysing. Fractional cloud cover is deduced after the raw colour image is analysed. Both files are stored

mainly in JPEG format depending on the TSI (Morris, 2005). More information on the specific TSI used for this research will be explained in detail in the next sub-section.

### **Cloud detection Algorithm**

Cloud detection algorithms are generally based on a threshold technique that utilizes the red-green-blue (RGB) channel magnitudes to determine the red-blue ratio (RBR) (Shields, Johnson, & Koehler, Automated whole sky imaging systems for cloud field assessment., 1993). A fixed ratio threshold algorithm was used to identify thick clouds by Shields *et al.* (1993) (Shields, Johnson, & Koehler, Automated whole sky imaging systems for cloud field assessment., 1993) whereas thin clouds are detected through a comparison with a clear sky background RBR library as a function of solar angle, look angle and site location. Another algorithm was used by Souza-Echer *et al.* 2006 (Souza-Echer, Pereira, Bins, & Andrade, 2006) of saturation in the hue, saturation and luminance (HSC) colour-space with fixed thresholds for cloud detection. However Carzola *et al.* (2008) (Carzola, Olmo, & Alados-Arboledas, 2008a) used neural networks to classify clouds. Neto *et al.* (2010) (Neto, von Wangenheim, Pereira, & Comunello, 2010) utilised the multidimensional Euclidean geometric distance (EGD) and Bayesian methods to classify image pixels based on cloud and sky patterns. Nevertheless, Shields *et al.* (2010) (Shields J. E., et al., 2010) added an adaptive threshold technique the haze amount for variations in haze amount in real time. The latest developed technique is that of Li *et al.* (2011) (Li, Lu, & Yang, 2011) which use a hybrid threshold technique (HYTA) that is based on both fixed and adaptive threshold techniques for cloud detection. The general description of the decision algorithm of the TSI will be given in the subsequent subsection below.

The TSI digital image analysis is based on the red-to-blue ratio (RBR), which is the ratio of red to blue light in a pixel, in each image pixel. The red-to-blue ratio for white clouds is higher than that of a clear blue sky. However, this distinction may be confused by that of a pallid sky with hazy conditions, especially near the sun or the horizon and also by dark clouds illuminated by a skylight. The red-to-blue ratio gives an indication to whether the dominant source of the scattered light incident on a pixel is the clear sky or a cloud (Chow, et al., 2011). A red-to-blue threshold needs to be established so as to differentiate between clear and cloudy pixels when a cloud image is processed. This limit need not to be constant across the entire image, but is

determined as a function of the relative position of the image pixel and the sun (Pfister, McKenzie, Liley, Thomas, Forgan, & Long, 2003).

Blue light is scattered more than red when molecular scattering takes place in clear skies, resulting in the clear sky appearing blue to our eyes. Fig 3.8 shows a specimen picture of clear-sky followed by a picture of its relative Red/Blue ratio and on extreme right two pictures that demonstrate extracts of blue and red pixel values that make up the specimen picture. In Fig 3.8, the red pixel brightness is low in the sky segment of the picture contrasted with the relating blue pixel values, aside from close to the skyline where the path length has increased making the first specimen sky picture seem white to our eyes. The scattered light appears whiter because usually scattering by aerosols have low wavelength dependence as compared to scattering by particles due to difference in size of aerosols contrasted to the wavelength of visible light (Chow, et al., 2011).

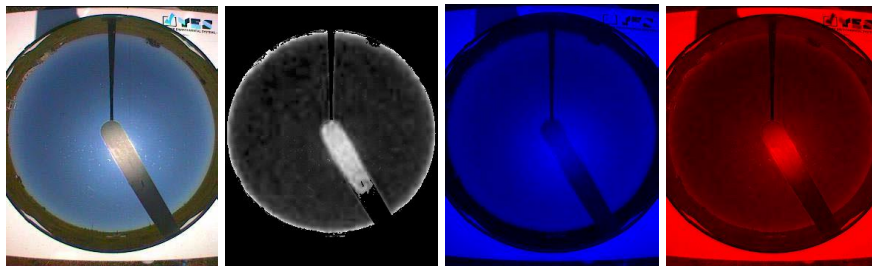


Figure 3.8: Clear-Sky Image (left end), Corresponding Relative Red/Blue Ratio Image, (second from left end), Separated Blue (second from right end), and Red (right end) Pixel Value Amount Images (Long, Slater, & Tooman, Total sky imager model 880 status and testing results, 2001).

Fig 3.9 demonstrates the cloud identification, picture relating to Fig 3.8, which is a graphical representation of the aftereffects of the sky spread recovery handling. In the cloud recognition picture, the camera arm and sun-shutting strip are covered out with dark, and the blue shading in whatever remains of the circle indicates that all the processed pixels (for a 160° FOV) have been resolved to be clear (Long, Slater, & Tooman, Total sky imager model 880 status and testing results, 2001).

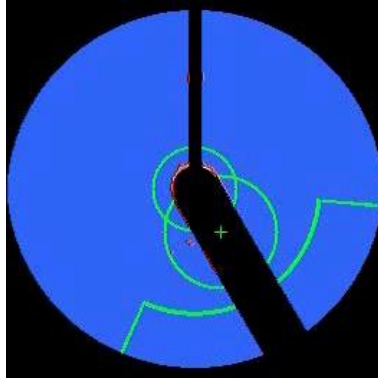


Figure 3.9: Cloud Detection Image Corresponding to Fig 3.8. Black represents shading. Green outlines represents areas where separate cloud/clear pixel counts are taken into consideration in the sky cover retrieval output files. (Long, Slater, & Tooman, Total sky imager model 880 status and testing results, 2001).

Unlike the clear sky, clouds generally scatter both the blue and red visible light more equally. A sample of a partly cloudy-sky is shown in Fig 3.10. As in Fig 3.8, in favour of this specimen shady sky picture are two pictures that demonstrate the relating separated blue and red pixel values that make up the example picture. In any case, where clouds are present, the red pixel qualities are much more noteworthy than where there are no clouds. The blue pixel picture appears far less difference in pixel values. The relative proportion of red/blue pixel values (Fig 3.10 second from left end) indicates obviously that the proportion is more noteworthy for clouds than for clear-sky. There is a preset lower limit for clear-sky proportion esteem for every pixel in the picture, and the pixels for which the red/blue proportion surpasses as far as possible are considered cloudy (Long, Slater, & Tooman, Total sky imager model 880 status and testing results, 2001).

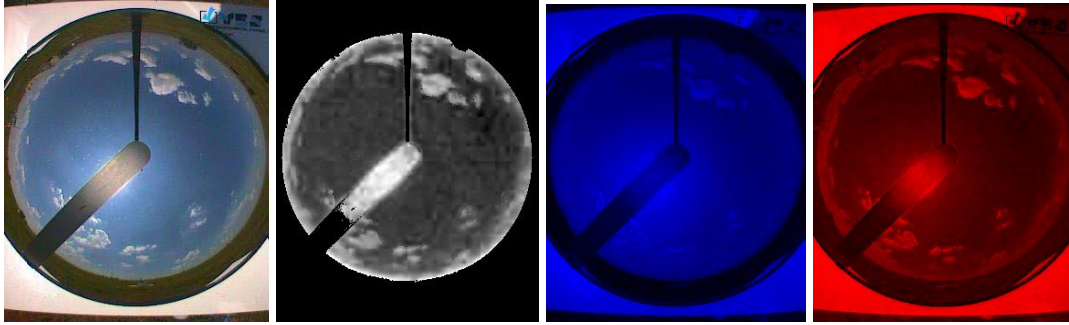


Figure 3.10: Cloudy-Sky Image (left end), Corresponding Relative Red/Blue Ratio Image (second from left end), Separated Blue (second from right end), and Separated Red (right end) Pixel Value Amount Images (Long, Slater, & Tooman, Total sky imager model 880 status and testing results, 2001).

Fig 3.11 shows a picture of the processed image which appears in Fig 3.10 where masking has been employed on the camera arm and shadowband. Grey colour represents thin clouds whereas white colour is for opaque/thick clouds. Considering an FOV  $160^\circ$ , the amount of cloudy pixels as a fraction of the total amount of pixels gives the fractional sky cover (Long, Slater, & Tooman, Total sky imager model 880 status and testing results, 2001).

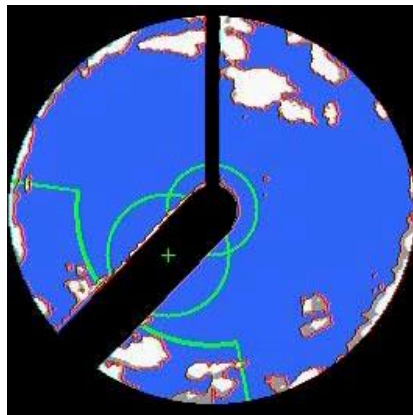


Figure 3.11: Cloud Detection Image Corresponding to Fig 3.10. (Long, Slater, & Tooman, Total sky imager model 880 status and testing results, 2001).

It was found that a solitary RBR threshold for the whole picture is not proper, hence the concept of the clear sky library is employed by other authors (Chow, et al., 2011) (Shields J. , et al., 2009). The RBR is big near the sun and inversely proportional to the sun-pixel angle. The RBR is also high near the horizon due to increased optical path and larger aerosol content near the

surface (Gueymard & Thevenard, 2009). These exaggerated RBRs can be removed by making use of the clear sky library (CSL). A CSL act as a reference point that is derived from historical clear day images and is used to compare with each pixel that is within the timeframe closer to that of the images in question (Shields, Johnson, & Koehler, Automated whole sky imaging systems for cloud field assessment., 1993). If the difference between the RBR and the CSL is greater than the thickness threshold, then the sky will be cloudy with opaque clouds. If the difference is less than the thickness threshold, but greater than or equal to the thin threshold then the sky is cloudy with thin clouds and if it is less than the thin threshold then the sky is clear.

### **3.3.2 TSI-440A Total Sky Imager**

The Total Sky Imager (TSI-440A) was fabricated by Yankees Environmental frameworks, Inc. It is a colour camera for the sky and comprises of a product bundle that permits the client a simple to-use and dependable field sensor for taking sky images. This instrument is intended for long haul field establishments and elements complex camera optics and also client serviceable mirror segments. A filament under the dome provides heating to evaporate any moisture on the dome surface. The instrument has a computer-automated rotating spherical mirror and a descending guiding camera shielded from direct daylight by a shadow-band. It generally has a sampling rate of taking an image in every 30 s. The camera provides an image resolution of 352 x 288 colour. Pictures are put away in a standard JPEG design, henceforth outsider apparatuses may likewise be utilized to see and change the pictures. The picture yield settings of the TSI information obtaining programming are default and can't be changed. The system captures images into industry-standard JPEG format data files which are then analysed for fractional cloud cover. The fractional cloud cover gives an estimated percentage of how overcast the sky is and it is represented by values between 0 and 1 for clear sky and fully overcast consecutively. The operating temperature ranges from  $-30\text{ }^{\circ}\text{C}$  to  $+34\text{ }^{\circ}\text{C}$ . It requires input power of 115/230 VAC and a standby battery may be added to avoid interruptions when there is a power failure.

A picture preparing program running on a client-given PC workstation takes pictures by means of TCP/IP at a client-characterized sampling rate and stores them to JPEG records for examination. The MS-Windows support analysis software masks known obstructions such as the camera, sun-shielding shadow-band and the arm. The raw picture is analysed for partial overcast

spread and both the raw and the analysed images are stored as files. The compression process actuates a little loss of data in the picture. To decide sky spread shielded by the camera arm and the shadow band, a picture mask is created, the edges of the veils are distinguished, and pixel estimations of the edge district are utilised to interpolate within the region. The system can act as a sky picture server to web programs if it is connected to a TCP/IP network on installations e.g. on the NREL website. Once the framework is set up there is little maintenance other than intermittent cleaning of the mirror (Yankee Environmental Systems). An image of the TSI-440 Total Sky Imager mounted on Desmond Clarence Building is shown in Fig 3.12.



Figure 3.12: Model TSI-440 Total Sky Imager as mounted on Desmond Clarence Building, at UKZN Howard College Campus, Durban.

The following side-by-side cloud images show a raw image before any processing has been performed and the same image with a software filter applied. The filter consists of a sophisticated image-analysis algorithm that clearly defines the clouds so that fractional cloud cover can then be calculated (Yankee Environmental Systems). Images in Fig 3.13 shows a processed image with a white sunspot which shows that for this particular image it was not sunny

or the sun was obstructed. The condition of being not sunny as indicated by the TSI depicts a condition whereby the sun is obstructed regardless of how low the  $CF$  can be, it may be regarded as locally not sunny. The picture below shows a high content of the opaque and no thin clouds. Thick or opaque clouds are shown as white and the thin clouds as grey in colour on the processed image. The portion of the sky which is not covered by any clouds is shown as blue in colour in the processed image.

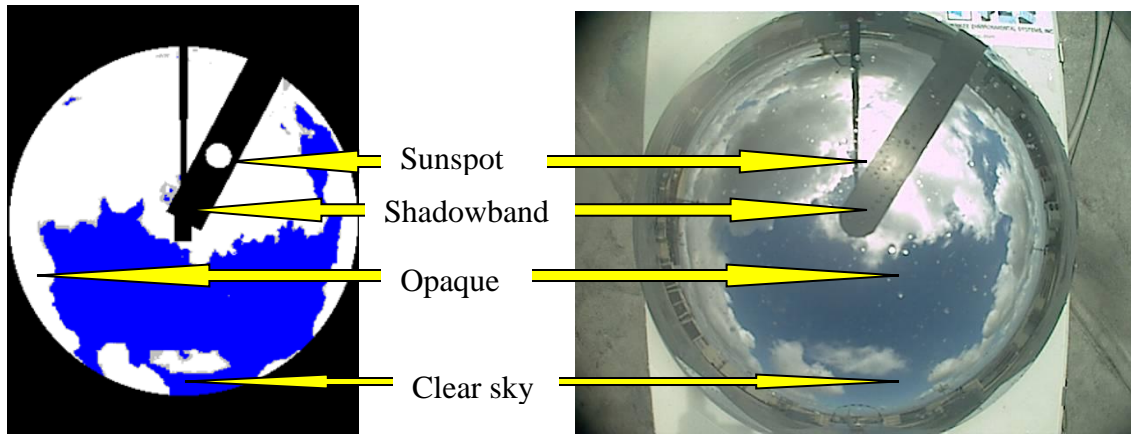


Figure 3.13: Processed image (left) and Raw sky image (right) at time 10:52 on the 01<sup>st</sup> of October 2014.

Images in the Fig 3.14 show a processed image with a yellow sunspot which shows that for this particular image the sky condition was sunny. The condition of being sunny as indicated by the TSI depicts a condition whereby the sun is not obstructed regardless of how high the  $CF$  can be, it may be regarded as locally sunny. The picture below shows a higher content of thinner clouds than of the opaque clouds since there is greyer than the white colour of the processed image.

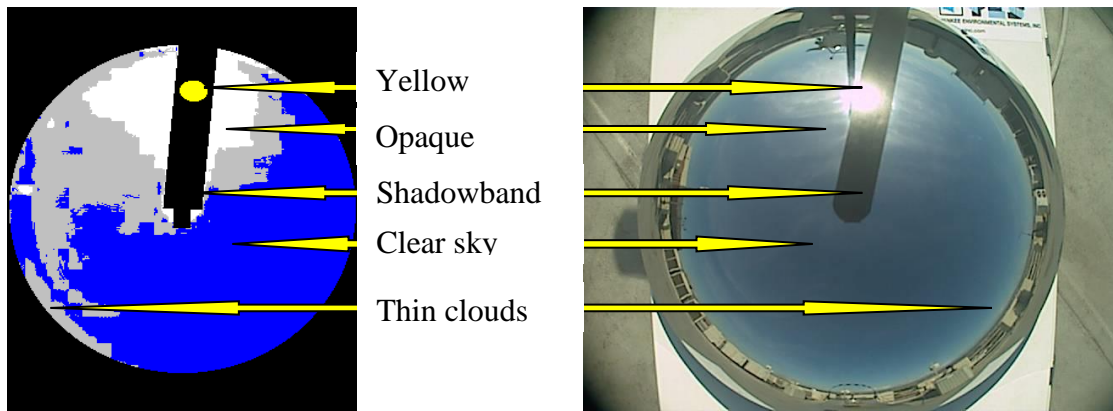


Figure 3.14: Processed image (left) and Raw sky image (right) at 11:45 on 14<sup>th</sup> of July 2014. The *CF* was 41% and the sky condition was sunny.

The *CF* for the image above is 41%, which means the sky fraction that is covered with clouds is 41% out of the 100% of the sky portion captured by the TSI. Besides cloud cover analysis, the TSI 440 can be used for: general meteorology, atmospheric research, pollution monitoring and plume research and UV prediction (Yankee Environmental Systems).

### Cloud detection algorithm

In examining the picture, the TSI decision algorithm depends on the RGB (Red, Green, Blue) code. R and B signs are contained in every picture pixel and a red to blue sign proportion (the R/B proportion) is connected with that specific pixel (Long, Sabburg, Calbo, & Pages, Retrieving cloud characteristics from ground-based daytime color all-sky images., 2006) (Pfister, McKenzie, Liley, Thomas, Forgan, & Long, 2003). The fractional sky cover estimation is based on thresholding the image according to the ratio of red and blue intensities of the red–green–blue (RGB) image (Calbo & Sabburg, Feature extraction from whole-sky ground-based images for cloud-type recognition, 2008). The TSI operator needs to choose a separating value for characterising a pixel as cloudy or not cloudy, hence R/B proportion less than the separating value registers clear-sky, somewhat blue sky pixels, while R/B proportions over the selected value allude to a cloudy sky, whitish sky pixels. The determination of the R/B ratio limit is arbitrary since it solely depends on the TSI operator’s perception of the sky, hence it is vital for the person who chooses these limit values to have adequate meteorological experience.

As mentioned, to determine the TSI picture pixel as overcast or clear-sky relies on upon the urgent and sufficient setting of the R/B proportion points of confinement to create two TSI routine parameters specifically, the clear/thin separation and the thin/opaque separation. In the event that the pixels have R/B proportion beneath the clear/thin parameter they would be referred to as clear-sky while pixels that are above the R/B ratio limit are referred to as cloudy. The amount of aerosols in air largely affects the clear/thin parameter. However, the thin/opaque parameter can be manipulated so as to sub-classify the cloudy pixels as either thin or opaque. When we add up segments comprising of the thin and opaque then cloud cover will be obtained. The above mentioned parameters denotes limits and they need to be exceptionally chosen to give a better comparison between the TSI prepared pictures and the sky scene observed by the onlooker. Nevertheless, the thin/opaque parameter is of paramount importance because of its character that is exceedingly uncertain.

The distinguishing proof of fringes and thin portions of clouds does not depend just on the subjective translation of the spectator, additionally on impacts like the low level of brightening in a few sections of the sky delivered by clouds hindering the sun, and the nearness of vaporized crest which can be mistakenly seen as the slender parts of a cloud. TSI pictures consist of some cumbersome impacts ascribed to characteristic and unnatural sources. At larger zenith angles the TSI gives untrue cloud cover, a distorted image and glare produced by serious daylight scattering. The mutilation of the pictures can be adjusted following the contortion from a TSI mirror stretches around 8 % at  $ZA \approx 50^\circ$  (Long, Sabburg, Calbo, & Pages, Retrieving cloud characteristics from ground-based daytime color all-sky images., 2006). There is no method as yet to completely differentiate aerosols from clouds utilising just the R/B proportion (Long, Correcting for circumsolar and near-horizon errors in sky cover retrievals from sky images, 2010). Hence the pale-whitened areas should be removed amid the TSI procedure to prepare the TSI pictures.



# Chapter 4

## Methods and Data Quality

This chapter comprises the procedure for where, when and how the data used in this thesis was collected. The data used in this thesis were collected at UKZN Howard College. Howard College is in Durban, South Africa at Latitude of  $-29.87098^{\circ}$  S, Longitude of  $30.97695^{\circ}$  E and Elevation of 150 m. Data was accessed through Southern African Universities Radiation Network (SAURAN) which provides solar radiometric data for the public. Data was collected for the period ranging from August 2014 to April 2015. This period was chosen since it is characterised by clear and cloudy days of summer. All instruments were strategically placed in close proximity such that there is no interference from other instruments. Available readings of interest included *DNI*, *DHI*, *GHI* and *CF* measurements at UKZN, Howard College campus. Extracted data from the SAURAN is recorded at different time intervals that ranged from minute to daily-averaged time-periods. Measurements are recorded in a spreadsheet file that is date- and time- stamped by day, month, and year as well as local clock time. The experimental set-up of the equipment used will be discussed in the sections to follow including the data acquisition.

### 4.1 Experimental set-up

The radiometric instruments were all mounted on the roof of a Desmond Clarence building at UKZN, Howard College campus. Among the instruments were Kipp & Zonen CMP11 unshaded, Kipp & Zonen CHP1 on a SOLYS tracker, Kipp & Zonen CMP11 under a shading ball on a SOLYS tracker and the total sky imager TSI 440A (Yankee Environmental Systems). The newly incorporated TSI was mounted on the rooftop of Desmond Clarence building in July 2014. The TSI was geometrically aligned with the sun so that the shadow band, taped onto the hemispherical mirror dome that rotates to track the sun across the sky throughout the day, prevented reflection of the sun directly into the digital camera lens.

## 4.2 Data acquisition

The daily, hourly and minute data were logged by a CR1000 data logger (with *LoggerNet* software). The cloud fraction was monitored by the TSI 440A (Yankee Environmental Systems) total sky imager. The following schematic shows the Instrument setup at the test site of the radiometric instruments (pyrheliometer and shaded and unshaded pyranometers) and TSI connected to CR1000 data logger shows how the TSI is connected at the UKZN Howard campus.

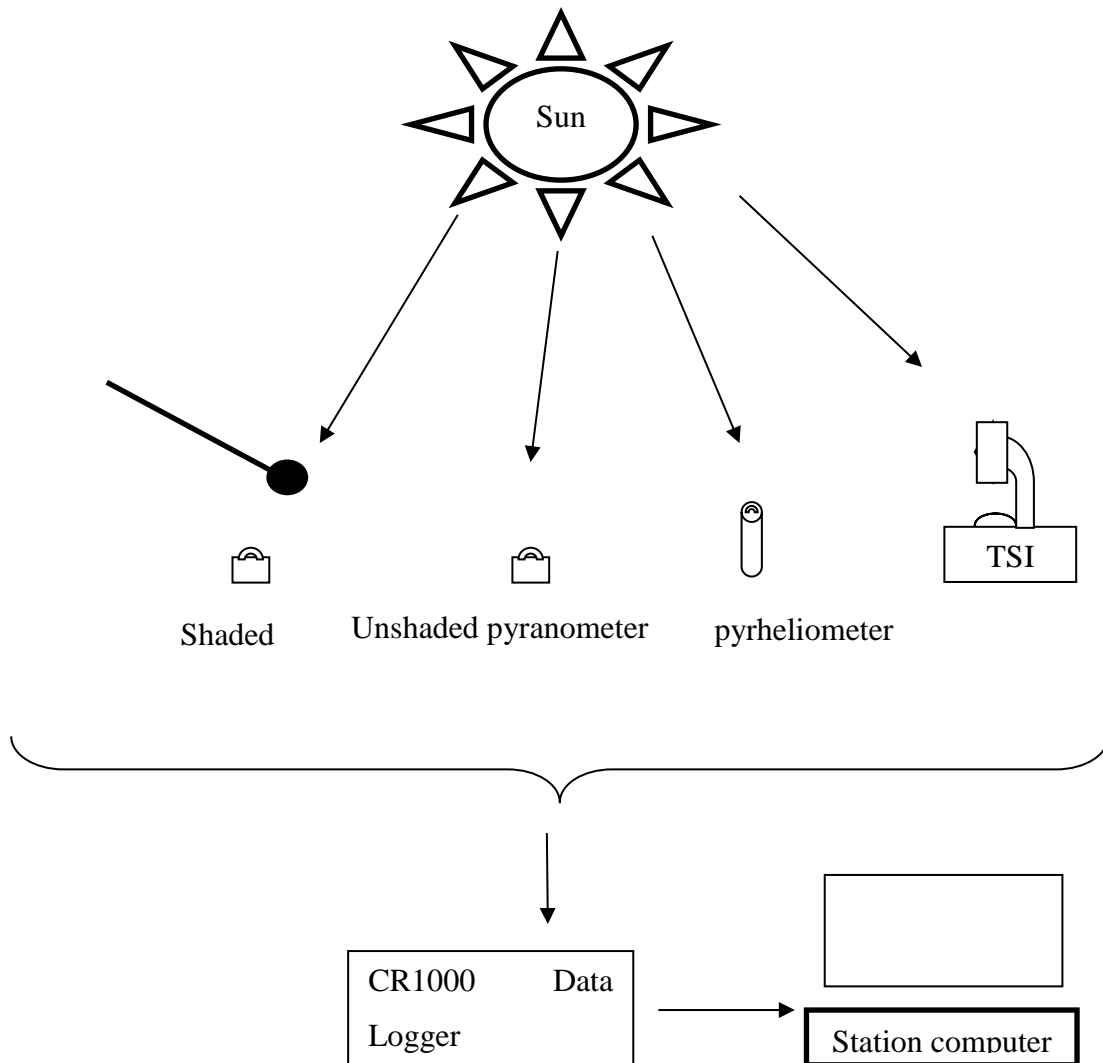


Figure 4.1: Instrument setup at the test site of the radiometric instruments (pyrheliometer and shaded and unshaded pyranometers) and TSI connected to CR1000 data logger.

### 4.3 Data collected and analysis

The cloud fraction values are measured by the TSI 440-A for particular days of interest. The method on how the  $CF$  is derived from the TSI image is outlined in chapter 3. The Kipp and Zonen shaded pyranometer, CMP11, is used to measure the readings for the average  $DHI$  and Kipp and Zonen unshaded pyranometer, CMP11, measures the average  $GHI$  component. The Kipp and Zonen Normal Incidence Pyrheliometer (NIP), CHP1, is used to measure the average  $DNI$  component. The  $DHI$ ,  $DNI$  and  $GHI$  values were retrieved from the SAURAN website on the internet and more station and instrument details are in the Appendix B. The used data were scrutinised for completeness and it was observed that the data were complete except for some time-frames, whereby there were no  $CF$  data recorded by the TSI hence radiometric readings for the corresponding time was removed from the data used. When the radiometric data are retrieved, quality control was performed on the dataset to make sure that the data has no problems through the use of equations (1.10), (1.11), (1.12) and (1.13) but however all data fulfilled the conditions stated by the equations. Furthermore the scatter plot of diffuse fraction  $k_d$  against clearness index  $k_t$  is shown in Fig 4.2 from Boland *et al.* (2013) and is used for comparison with the actual plot of  $k_d$  against  $k_t$  for this study which is shown in Fig 4.3. In Fig 4.2, most of the data fall along the lower right-hand side of the plot which represent clear periods. The data points spread to the right representing data when clouds are less present and the shape is as suggested by Boland *et al.* (2013) for data with no problem (Boland, Huang, & Ridley, 2013). Using Tsubo and Walker (2003) classification  $K_t$  ranges, it can be noted that most of the diffuse fraction values fall in the middle class  $K_t$  range ( $0.2 \leq K_t \leq 0.8$ ). This result is in agreement to the findings of Tsubo and Walker (2003) for southern Africa results whereby the most of the diffuse fraction values also fell in the middle class  $K_t$  range ( $0.2 \leq K_t \leq 0.8$ ) (Tsubo & Walker, 2003).

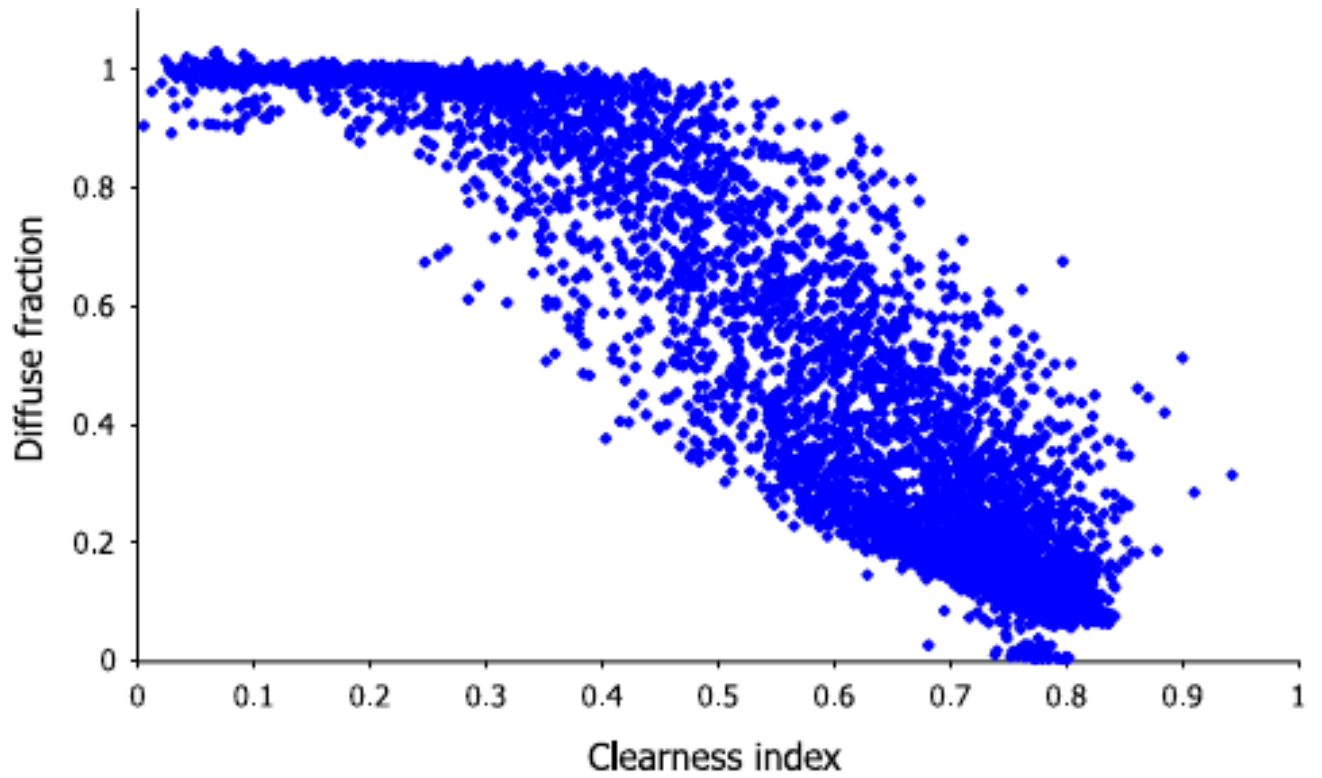


Figure 4.2: Plot of diffuse fraction  $k_d$  against clearness index  $k_t$  for hourly values at Adelaide (Boland, Huang, & Ridley, 2013).

The scatter plot shown in Fig 4.3 is similar to Fig 4.2 which means the data obtained for this study is of acceptable quality.

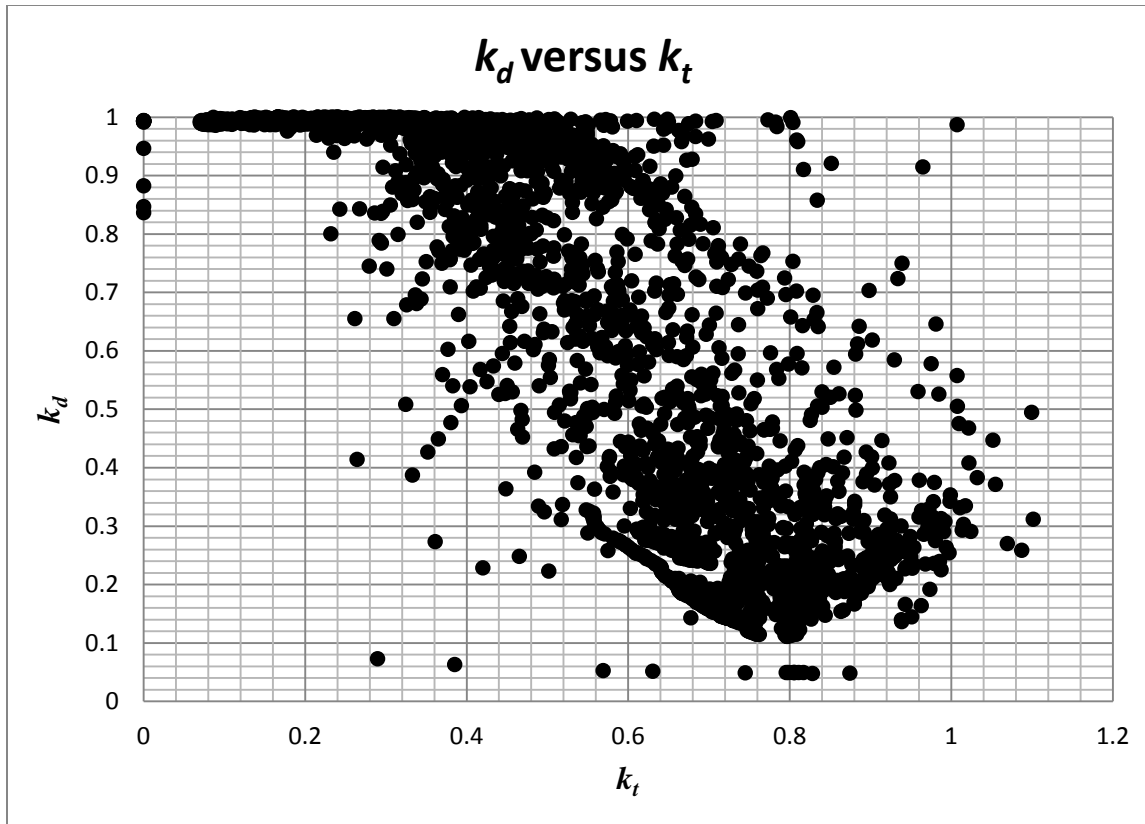


Figure 4.3: Graph of the  $k_d$  against clearness index  $k_t$  for 1-minute data of the entire dataset.

The scatter plot of atmospheric transmittance  $k_b$  against  $k_t$  was plotted in Fig 4.4 from Vignola *et al.* (2012) and is used for comparison with the actual plot of  $k_b$  against  $k_t$  for this study shown in Fig 4.5. In Fig 4.4, most of the data fall along the lower left-hand side of the plot which represent cloudy periods. The data points spread to the right representing data when clouds are less present and the shape of the graph is as suggested by Vignola *et al.* (2012) for data with no problem (Boland, Huang, & Ridley, 2013). Values with the largest clearness index are not the values with the largest beam clearness index values. Large clearness index values occur when there are clouds in the vicinity of the sun to reflect sunlight into the global pyranometer and this reflected sunlight does not reach the pyrheliometer hence a relatively lower  $DNI$ . The scatter plot shown in Fig 4.5 compares well to Fig 4.4 which means the data obtained for this study is of acceptable quality.

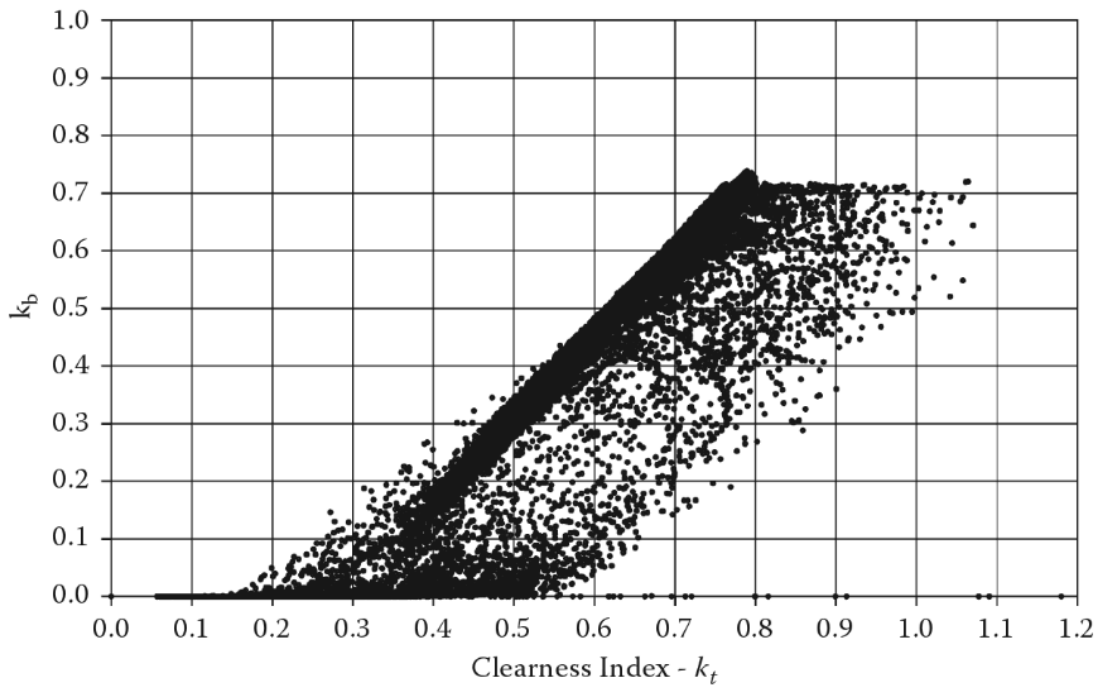


Figure 4.4: Plot of  $k_b$  versus  $k_t$  for 1-minute data at Eugene (Vignola, Michalsky, & Stoffel, 2012).

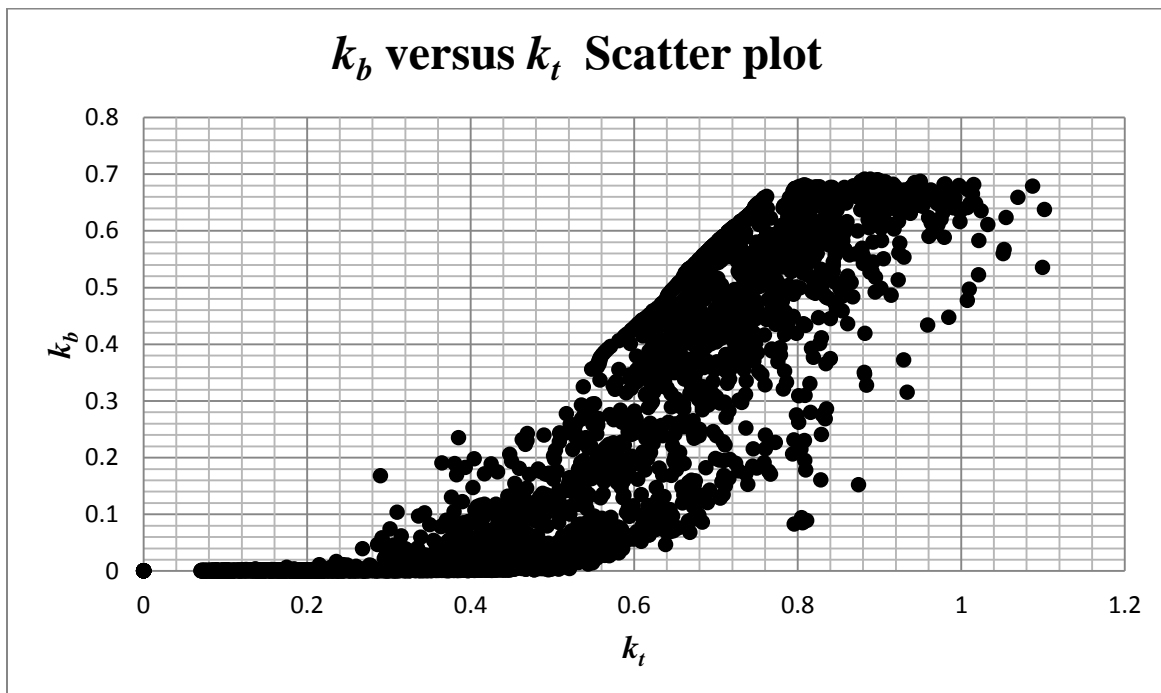


Figure 4.5: Graph of  $k_b$  vs  $k_t$  for 1-minute data of the entire data.

Since the data has been evaluated and found to be conforming to the trends suggested by the literature, it was used for statistical analysis. The research question is going to be answered in two forms, which are, qualitative and quantitative. The qualitative aspect will plot the radiometric profiles of *GHI*, *DNI*, and *DHI* against *CF* graphs and examine typical patterns and the effects of variation in *CF*. Images of corresponding *CF* will be used in explaining the effect of clouds on radiometric readings since they show if the sun is obstructed or not. Plots for centred moving averages of radiometric profiles and *CF* at different time scales were also plotted against time and will be compared to 1 minute data.

The quantitative aspect used a clear sky model to generate the clear sky and extraterrestrial radiometric profiles that will be used to calculate the clearness indices which was correlated with the *CF* for analysis. The clear sky model that was used to generate clear sky radiometric profiles is the National Renewable energy Laboratory (NREL's) Measurement & Instrumentation Data Center (MIDC) Solar and Moon Position Algorithm (SAMPA) Calculator. The clear sky radiometric profiles that will be derived are clear sky global horizontal irradiance, clear sky direct normal irradiance and clear sky diffuse horizontal irradiance which are represented as follows:  $GHI_c$ ,  $DNI_c$  and  $DHI_c$  respectively. The extraterrestrial radiometric profiles were generated by the NREL's MIDC Solar Position and intensity (SOLPOS) calculator. The extraterrestrial profiles include extraterrestrial global horizontal irradiance ( $GHI_o$ ) and extraterrestrial direct normal irradiance ( $DNI_o$ ). Extraterrestrial diffuse horizontal irradiance was not included since it is  $0 \text{ W/m}^2$ . A clear sky radiometric profile against time for 04 December which was a clear sky is shown in Fig 4.6.

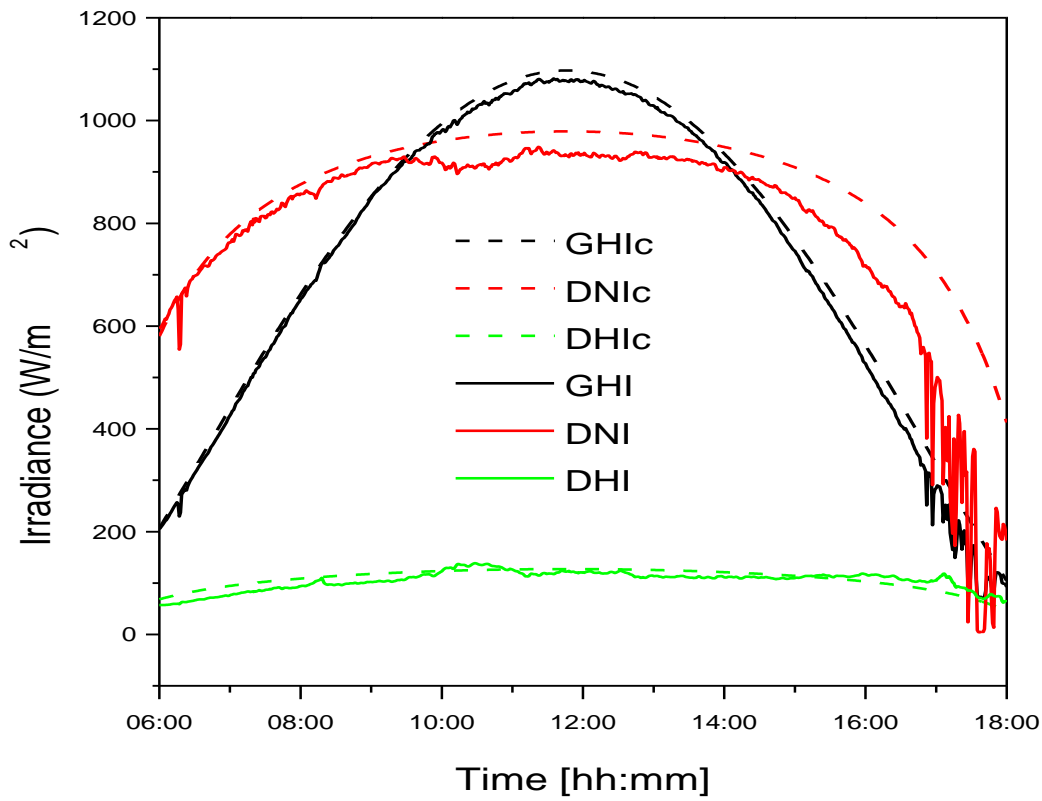


Figure 4.6: Graph of clear sky and actual radiometric readings for 04 December 2014.

Clearness indices were derived as follows:  $GHI/GHI_c$  as clearness index  $k_c$ ,  $GHI/GHI_o$  as clearness index  $k_t$ ,  $DNI/DNI_c$  as atmospheric transmittance,  $DNI/DNI_o$  as atmospheric transmittance  $k_b$  and  $DHI/DHI_c$ . Each clearness index for 1 minute data was plotted against  $CF$  as follows:  $GHI/GHI_o$  vs  $CF$ ,  $GHI/GHI_c$  vs  $CF$ ,  $DNI/DNI_o$  vs  $CF$ ,  $DNI/DNI_c$  vs  $CF$  and  $DHI/DHI_c$  vs  $CF$  which is as suggested by Pfister *et al.* (2003) except that this work is using 1 minute data. As Janjai and Tosing (2000), Augustine and Nnabuchi (2009a,2009b and 2010) have analysed the relationship between cloud fraction and solar radiation through correlating the monthly mean radiation ratio ( $k_t$ ) and the monthly mean  $CF$ , this work performed the same correlations on the scatter plots of  $\langle GHI/GHI_o \rangle_t$ ,  $\langle GHI/GHI_c \rangle_t$ ,  $\langle DNI/DNI_o \rangle_t$ ,  $\langle DNI/DNI_c \rangle_t$  and  $\langle DHI/DHI_c \rangle_t$  against  $\langle CF \rangle_t$  but for shorter time frames of the order of 15 minutes, 30 minutes, 1 hour, 2 hours, 3 hours and 4 hours. However the scatter plots for  $\langle GHI/GHI_o \rangle_t$

against  $\langle CF \rangle_t$  correlations of 30 minutes, 2 hours and 3 hours averages are not included in the main text but will be provided in Appendix D.

The Matlab code that was used to calculate the averages of the above time is in Appendix C. Statistical analysis was performed on the data by looking at how strong the variables correlate. Linear regression was used to obtain the correlation coefficients ( $R$ ) and correlation of determination ( $R^2$ ) for scatter plots of  $\langle GHI/GHI_o \rangle_t$ ,  $\langle GHI/GHI_c \rangle_t$ ,  $\langle DNI/DNI_o \rangle_t$ ,  $\langle DNI/DNI_c \rangle_t$  and  $\langle DHI/DHI_c \rangle_t$  against  $\langle CF \rangle_t$ . Different time-averages were used to produce centred moving average scatter plots for all graphs mentioned above and their  $R$  and  $R^2$  were compared to identify the suitable time period when a higher correlation coefficient of determination was found. As done by Pfister *et al.* (2003) the correlations of clear sky-derived indices will be compared to the extraterrestrial-derived indices to examine the ones giving higher  $R$  and  $R^2$  (Pfister, McKenzie, Liley, Thomas, Forgan, & Long, 2003).

# Chapter 5

## Results

The results of the radiometric profiles and cloud fraction are presented in this chapter. The days that will be presented here are 14<sup>th</sup> of July 2014 for a clear day, 10<sup>th</sup> of September 2014 and 30<sup>th</sup> of January 2015 for partly cloudy weather days and 27<sup>th</sup> of January 2015 for totally overcast sky condition. More days were selected for partly cloudy weather so as to establish the relationship between radiometric readings and cloud fraction. Results are presented per specific day showing the TSI images of interest for that specific day and the plot showing how radiometric profiles vary with change in *CF* with respect to time. Results for a clear day will be presented first, followed by results of totally overcast sky and lastly results of different partly cloudy sky conditions. The first section is based more on qualitative results, whereas the second section is based on quantitative aspects of the results.

### 5.1 Radiometric profiles and TSI images to show cloud fraction *CF*

#### Results for 14<sup>th</sup> July 2014

A raw sky image showing a clear sky is shown in Fig 5.1 (a). This image shows a sky that is clear and to get the fraction of the sky that is covered with clouds a TSI uses a processed image which is shown in Fig 5.1 (b). The *CF* for this image is 4%.

The radiometric profiles show variation with change in *CF* with respect to time in Fig 5.2. The graph shows profiles from 06:00 to 18:00 but the *CF* profile is shown for the period when the TSI was in operation from 11:15 to 16:00.

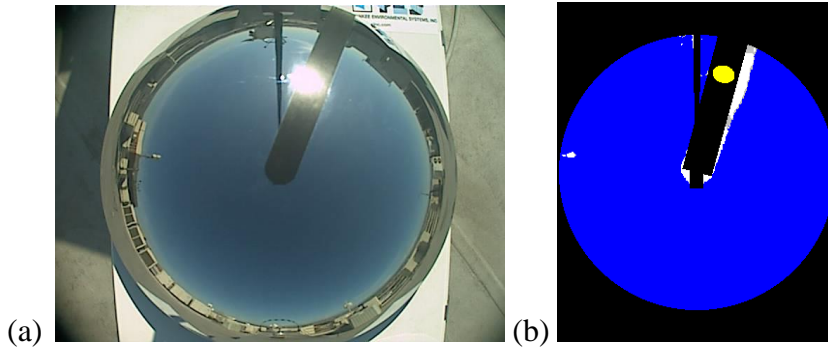


Figure 5.1: Raw sky image (a) and processed image (b) at 11:09 on 14<sup>th</sup> of July 2014. The *CF* was 4% and the Sun was not obstructed by clouds.

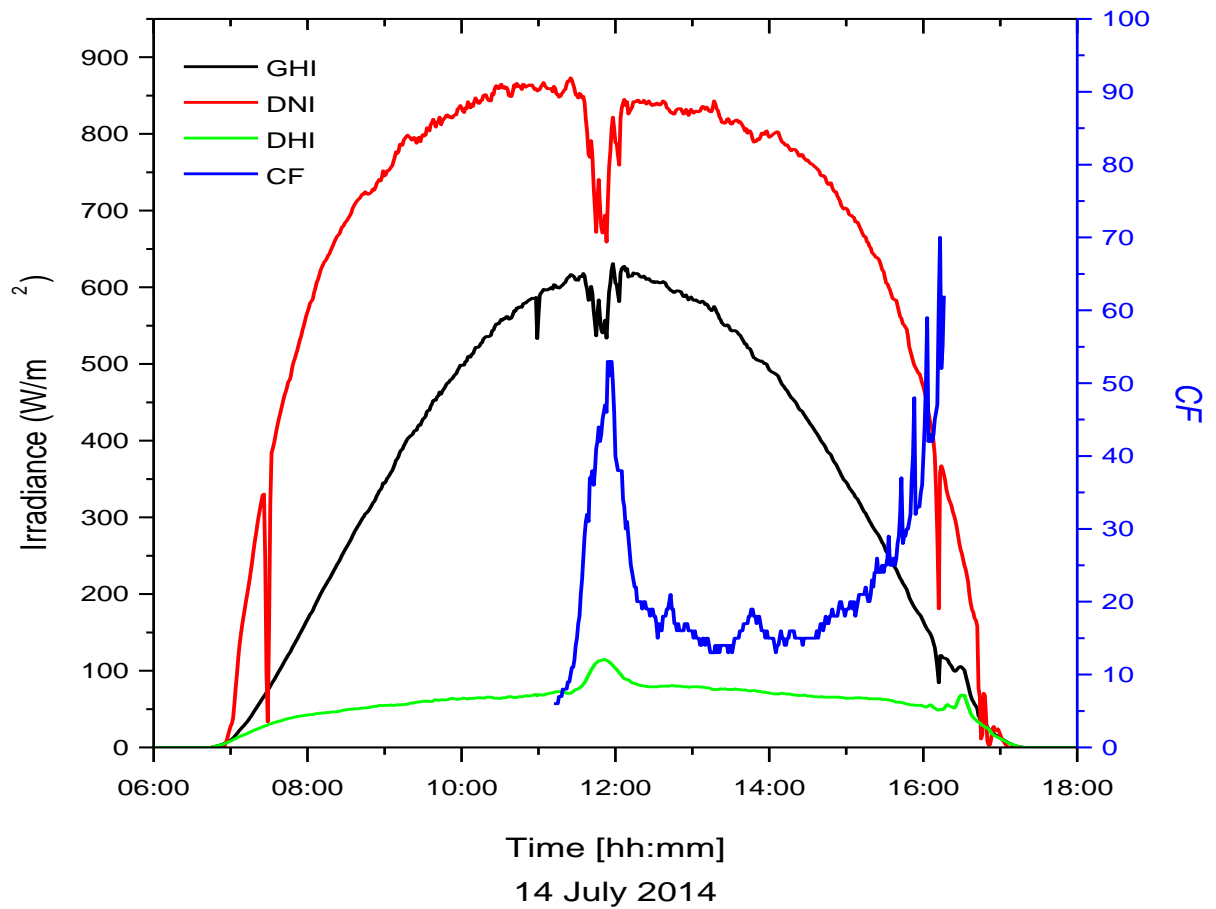


Figure 5.2: Plot of *CF* and solar irradiance against time between 06:00 and 18:00 on 14<sup>th</sup> of July 2014.

According to Fig 5.2 representing a clear day, between the time 11:00 and 13:00 there was a sharp increase in  $CF$  which consequently resulted in the beam irradiance  $DNI$ , dropping from just above  $850 \text{ W/m}^2$  to  $650 \text{ W/m}^2$ . This dip on the beam irradiance is a result of the Sun being partly obscured by thin clouds. Increased  $CF$  leads to lower beam, but higher diffuse irradiance due to increased scattering. The increase in the diffuse irradiance is directly a result of more scattering take place due to more thin clouds in the atmosphere. Even though the  $DHI$  component increased, the  $GHI$  component for this period decreased due to a high decrease in the  $DNI$  component. Between 11:00 and 13:00, the sky condition was sunny as recorded by the TSI. An image in Fig 5.3 shows a processed image with a yellow sunspot which shows that for this particular image the sky condition was locally sunny, showing a condition whereby the Sun is not obstructed regardless of how high the  $CF$  can be.

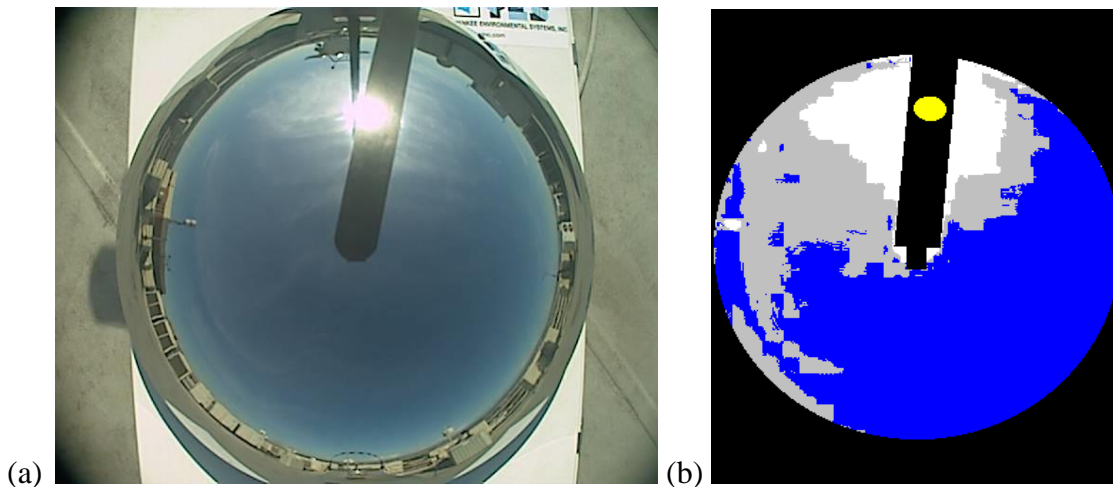


Figure 5.3: Raw TSI image (a) and processed TSI image (b) at 11:45 on 14<sup>th</sup> of July 2014. The  $CF$  was 41% and the Sun was not obstructed.

The fluctuations that occurred between the time period 12:30 and 14:30 on the  $CF$  resulted in corresponding fluctuations in  $DNI$  significantly and little variation in  $DHI$  component. Between the time 15:00 and 16:00 there was another gradual increase on the  $CF$  from 15% to 40%, resulting in a decrease on the  $DNI$  correspondingly from  $800 \text{ W/m}^2$  to  $470 \text{ W/m}^2$ . Variations in  $CF$  may not cause any change in  $DHI$  component as evidenced after 15:00, unlike between 11:00 and 13:00 whereby an increase in  $CF$  resulted in an increase in  $DHI$ . The sky condition was sunny for this period, but there was small or insignificant scattering of Sun rays during this

period since the irradiance intensity decreases as the time approaches sunset hence a lower *DHI* component. *GHI* decreases as the *DNI* component decreased since there is little change in the *DHI* component.

### Results for 27<sup>th</sup> January 2015

A raw sky image showing an overcast sky is shown in Fig 5.4a This image shows a sky that is totally filled with clouds and to get the fraction of the sky that is filled with clouds a TSI uses a processed image which is shown in Fig 5.4b. The *CF* for this image is 100%.

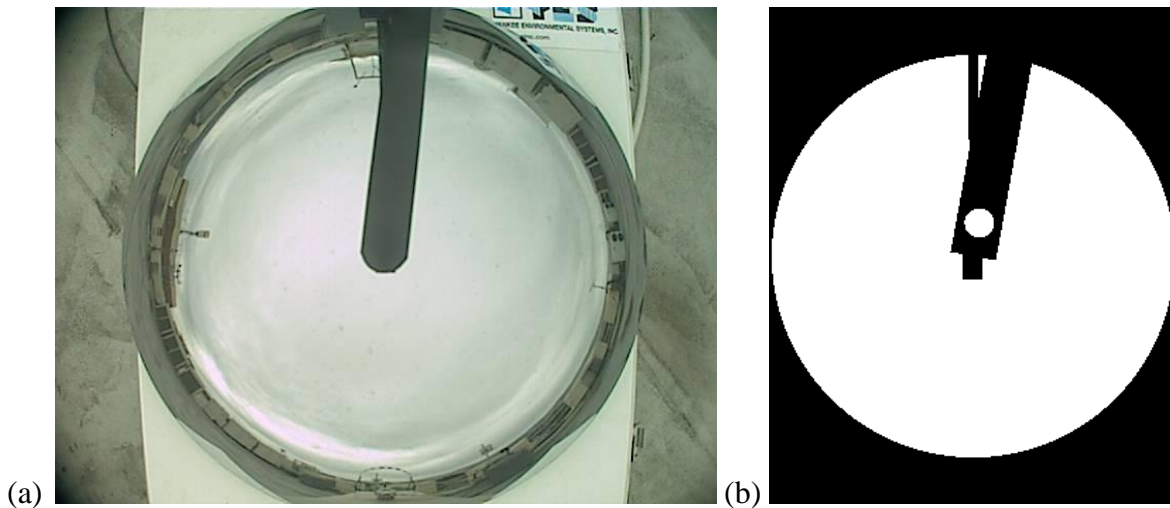


Figure 5.4: Raw sky image (a) Processed image (b) and at 12:00 on 27<sup>th</sup> of January 2015. The *CF* was 100% and the sun was obstructed by clouds.

The radiometric profiles showing variation with change in *CF* with respect to time are shown in Fig 5.5. The graph shows profiles from 06:00 to 18:00 but the *CF* profile is shown for the period when the TSI was in operation from 09:30 to 16:00.

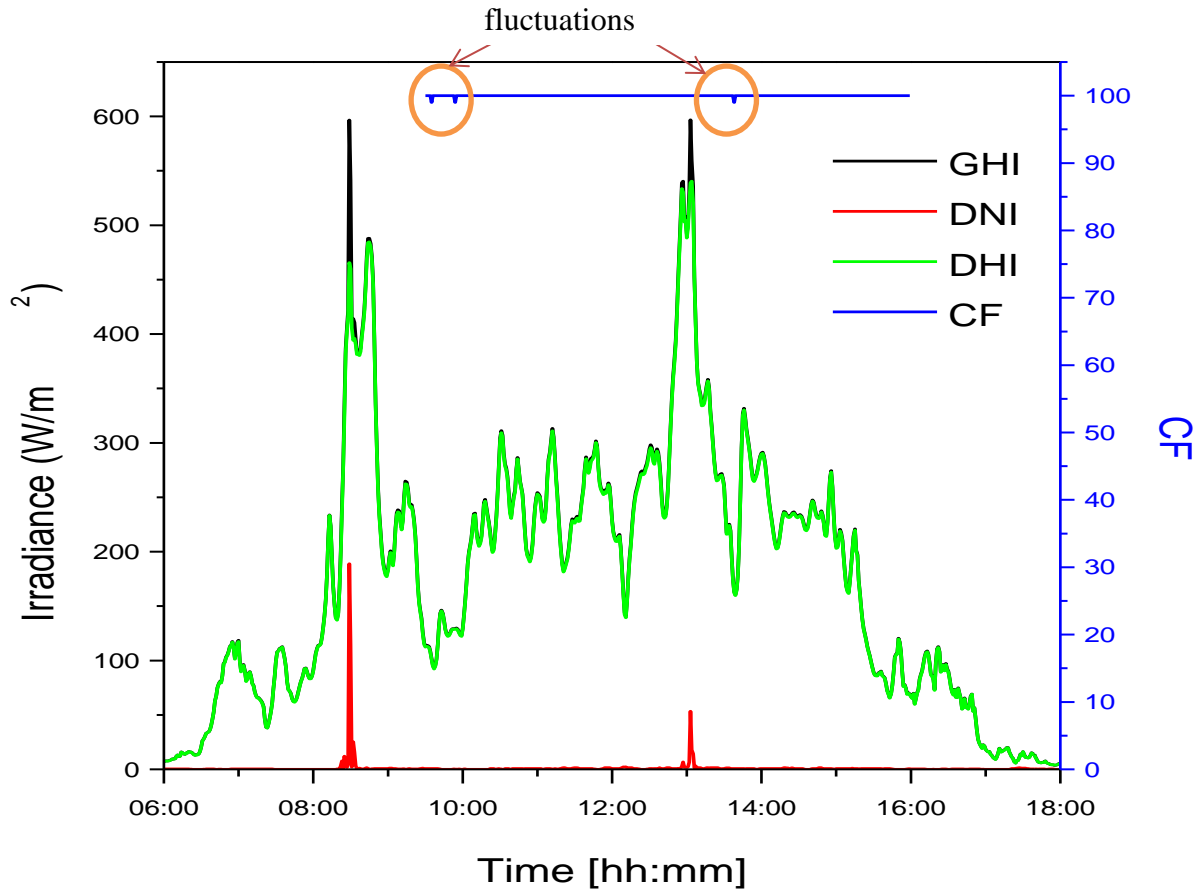


Figure 5.5: Plot of  $CF$  and solar irradiance against time between 06:00 and 18:00 on 27<sup>th</sup> of January 2015.

Fig 5.5 shows a typical overcast day whereby the  $CF$  is constantly 100%. There were insignificantly small fluctuations between 09:30 and 10:00 but beam irradiance remained constant at  $DNI = 0 \text{ W/m}^2$ . The other small fluctuation was between 13:30 and 14:00 but it also had no effect on the beam irradiance since it remained constant at  $DNI = 0 \text{ W/m}^2$ . There was a noticeable spike on the beam irradiance (see Fig 5.30) at 13:05 regardless of the  $CF$  being 100% at this time. The enhancement was a result of the gaps within the clouds and the thickness of the clouds that was somehow porous to some solar radiation, which is evidenced by the illumination that is shown in the images for this particular time in Fig 5.6.

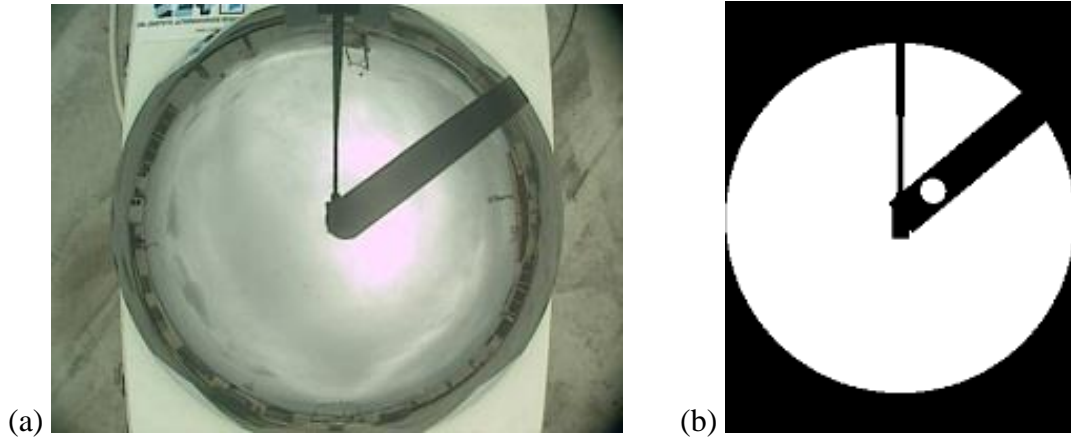


Figure 5.6: Raw sky image (a) and processed image (b) at 13:03. The  $CF$  was 100% and the sky condition was not sunny.

From the image in Fig 5.6 it is clear that even though the sky condition is overcast the sunspot of the raw image is illuminated revealing that the clouds that were around the sunspot were not thick enough to prevent all the sun rays from passing through hence a spike in the beam irradiance graph. Since the clouds at this time did not totally prevent the sun rays from passing through, there was more scattering as compared to other times giving rise to a higher diffuse irradiance of  $550 \text{ W/m}^2$  being registered and consequently a higher global irradiance. Between the time 09:30 and 16:00 when the sky was constantly overcast the diffuse irradiance was always fluctuating in the range of  $100 \text{ W/m}^2$  to  $300 \text{ W/m}^2$  thus exhibiting the fact that even though the  $CF$  may be constantly overcast at 100% the cloud thickness content does not remain the same hence different scattering magnitudes. Different scattering magnitudes will result in varying diffuse irradiance which consequently causes fluctuations. This shows that for the same  $CF$ , we may have different cloud content (cloud optical thickness) leading to different responses on the beam/diffuse irradiance graph thus there is no simple relationship between the  $CF$  alone (without other cloud properties) and the radiometry measurements.

### Results for 30<sup>th</sup> January 2015

A raw sky image showing a partly cloudy sky is shown in Fig 5.7a. This image shows a sky that is partly cloudy and to get the fraction of the sky that is covered with clouds the TSI uses a processed image which is shown in Fig 5.7b. The  $CF$  for this image is 53%.

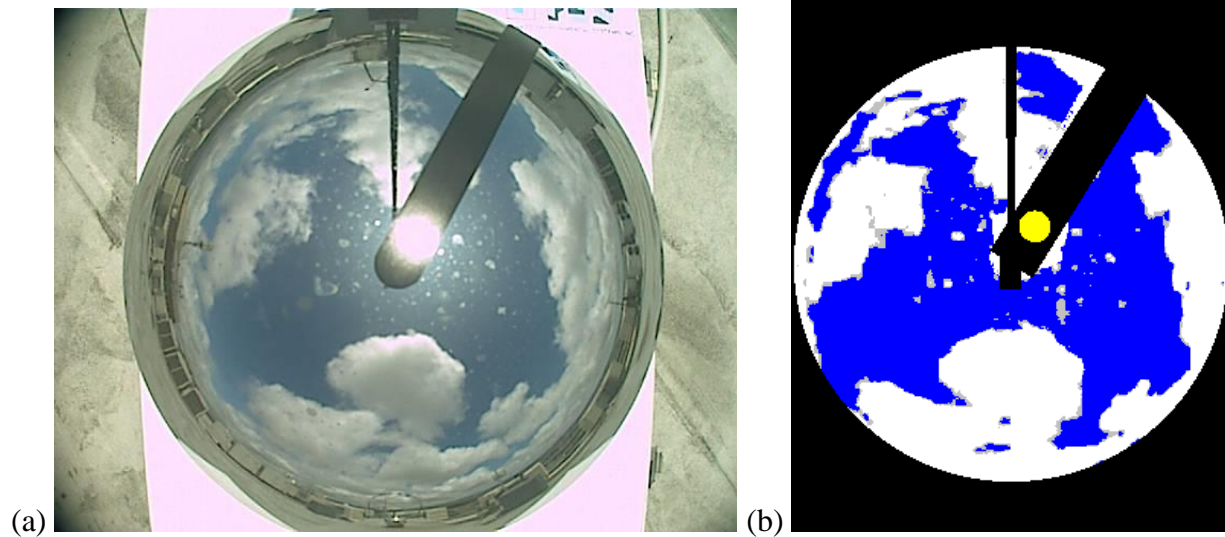


Figure 5.7: Raw sky image (a) Processed image (b) and at 11:38 on 30<sup>th</sup> of January 2015. The  $CF$  was 53% and the sun was obstructed by clouds.

The radiometric profiles showing variation with change in  $CF$  with respect to time are shown in Fig 5.8. The graph shows radiometric profiles from 06:00 to 18:00 but the  $CF$  profile is shown for the period when the TSI was in operation from 09:30 to 16:00. As seen in Fig 5.8, between 08:00 and 10:00 the  $CF$  was 100%, but it fluctuates and dips to a minimum of 80% at 8:20. To explain the effects of  $CF$  on radiometric profiles, the graph is zoomed for timeframe between 08:00 and 10:00 as shown in Fig 5.9.

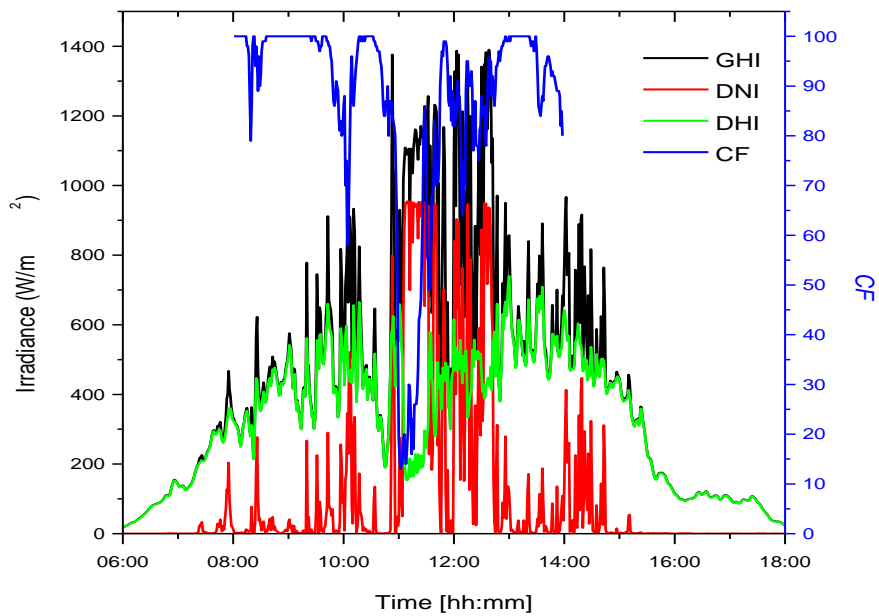


Figure 5.8: Plot of  $CF$  and solar irradiance against time between 06:00 and 18:00 on 30<sup>th</sup> of January 2015.

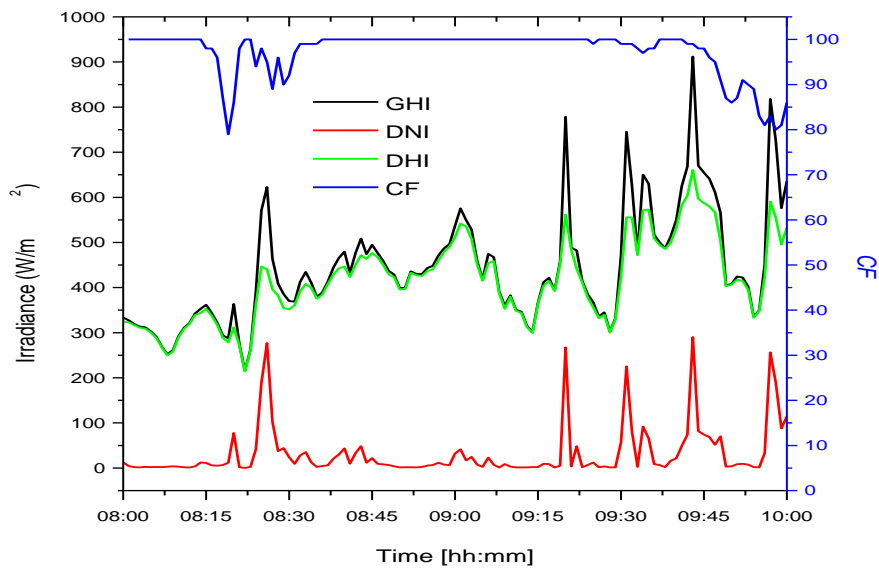


Figure 5.9: Plot of  $CF$  and solar irradiance against time between 08:00 and 10:00 on 30<sup>th</sup> of January 2015.

According to Fig 5.9, between the time 08:00 and 09:00 the beam irradiance was very low with a minimum of  $DNI = 0 \text{ W/m}^2$ . However, there was a peak on the beam irradiance graph between 08:20 and 08:30 reaching a maximum of  $240 \text{ W/m}^2$  at 08:25. The peak was due to the fact that the sun was not obstructed between 08:22 to 08:26 according to the TSI image in Fig 5.10.

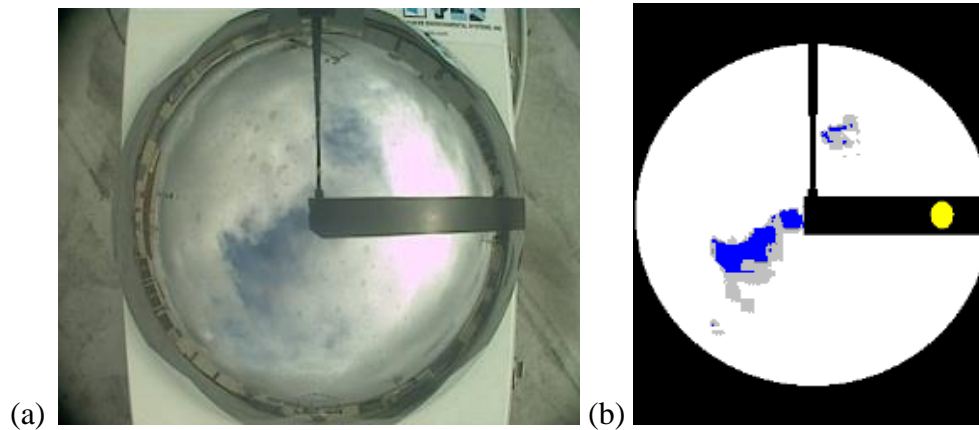


Figure 5.10: Raw sky image (a) and processed image (b) at 08:25. The  $CF$  was 98% and the sky condition was sunny.

Fig 5.10 shows a processed image and raw sky image at 08:25. The  $CF$  was 98% and the sun was not obstructed. Since the sun was not obstructed for this period more scattering took place, resulting in a higher diffuse irradiance of  $DHI = 440 \text{ W/m}^2$  from  $200 \text{ W/m}^2$ . Between 09:00 and 11:00 there were fluctuations in the  $CF$  having a dip that reached a minimum of 58% at 10:05. These fluctuations in the  $CF$  resulted in the indirectly proportional fluctuations in the beam irradiance graph. Within these fluctuations in the beam irradiance graph there were peaks which resulted because the sun was not obstructed. The maximum peaks on the beam irradiance graph were  $DNI = 500 \text{ W/m}^2$  at 10:05 and  $DNI = 800 \text{ W/m}^2$  at 10:50 when the  $CF$  was lowest and also the sun was not obstructed at these times. Between 09:15 and 09:45 small changes in  $CF$  resulted in pronounced fluctuations in  $GHI$ ,  $DNI$  and  $DHI$  components. A decrease in  $CF$  just before 10:00 resulted in an increase in  $GHI$ ,  $DNI$  and  $DHI$  components.

As seen in Fig 5.8, there is too much fluctuation in both radiometric and  $CF$  profiles between 11:00 and 13:00 hence an enlarged part of this time-frame graph is zoomed in Fig 5.11. In Fig 5.11 just after 11:00 the  $CF$  decreased from 85% to 13%, resulting in an increase in beam

irradiance from  $DNI = 50 \text{ W/m}^2$  to a maximum of  $950 \text{ W/m}^2$  and a decrease in diffuse irradiance from  $DHI = 650 \text{ W/m}^2$  to  $150 \text{ W/m}^2$ . Fewer clouds in the sky result in less scattering hence a lower  $DHI$  component was received.

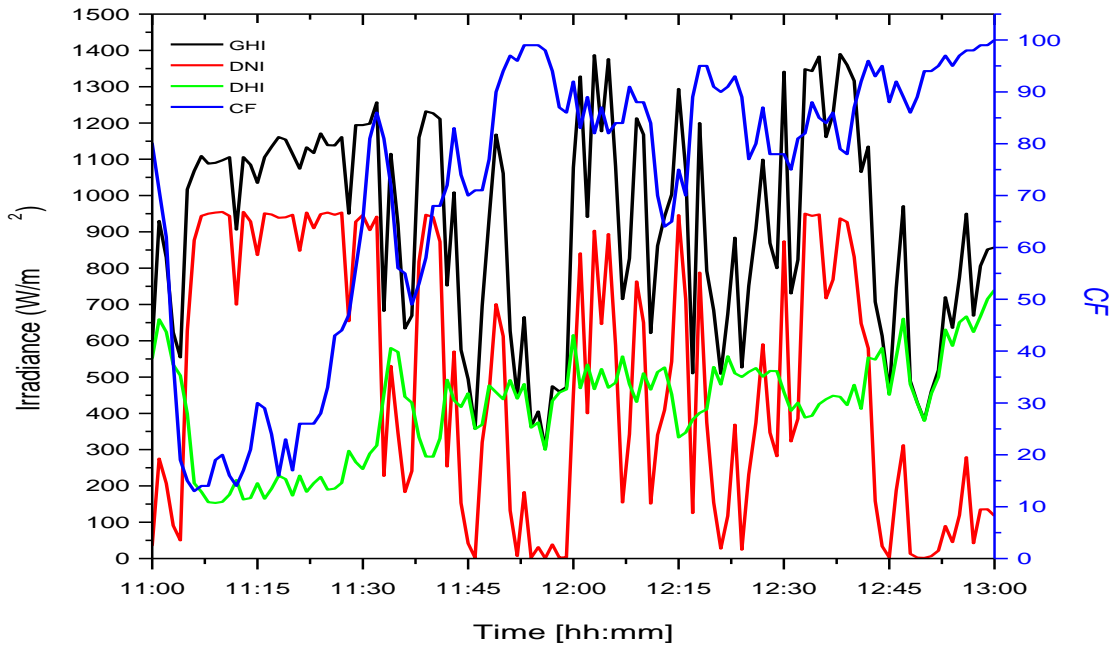


Figure 5.11: Plot of  $CF$  and solar irradiance against time between 11:00 and 13:00 on 30<sup>th</sup> of January 2015.

An increase in  $CF$  towards 11:30 resulted in an increase in diffuse irradiance and a decrease in the  $DNI$  and  $GHI$  components. Since the amount of clouds in the sky increased the diffuse irradiance increased to  $550 \text{ W/m}^2$  at 11:30 as there was more scattering taking place. For this period, the diffuse irradiance increased with increasing  $CF$  since there were more clouds in the sky increasing the scattering of solar radiation. At 11:46 a very low beam irradiance  $DNI \sim 0 \text{ W/m}^2$  was recorded, but the  $CF = 71 \%$  as a result of the sun being blocked by the clouds. However the TSI image for 11:46 shows that the sky was not obstructed as shown in Fig 5.12. Between 12:00 and 13:00 the  $CF$  fluctuated having a minimum of 65% at 12:13 and a maximum of 100% at 13:00 and the beam irradiance also fluctuated opposite to  $CF$  reaching a beam irradiance of  $DNI = 0 \text{ W/m}^2$  at 12:55 when the  $CF$  was 100% and the sky was overcast.

However, between 12:30 and 12:45 the  $CF$  was as high as 80%, but the beam irradiance was also high reaching a maximum of  $DNI = 950 \text{ W/m}^2$ .

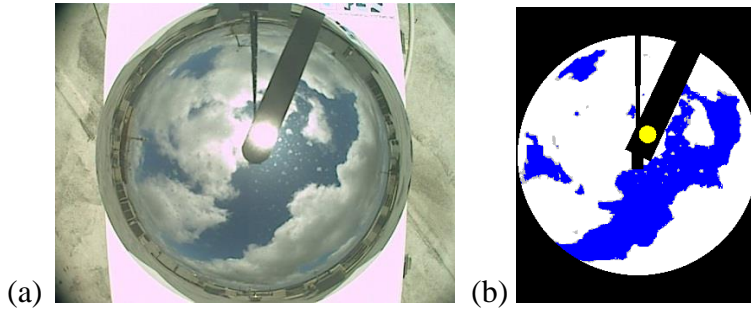


Figure 5.12: Raw sky image (a) and processed image (b) and at 08:25. The  $CF$  was 71% and the sky condition was sunny.

### Results for 10<sup>th</sup> September 2014

The sky condition for the 10th of September 2014 is a partly cloudy day as evidenced by a series of TSI raw and processed images for the time 10:00, 11:00 and 12:00 in Fig 5.13.

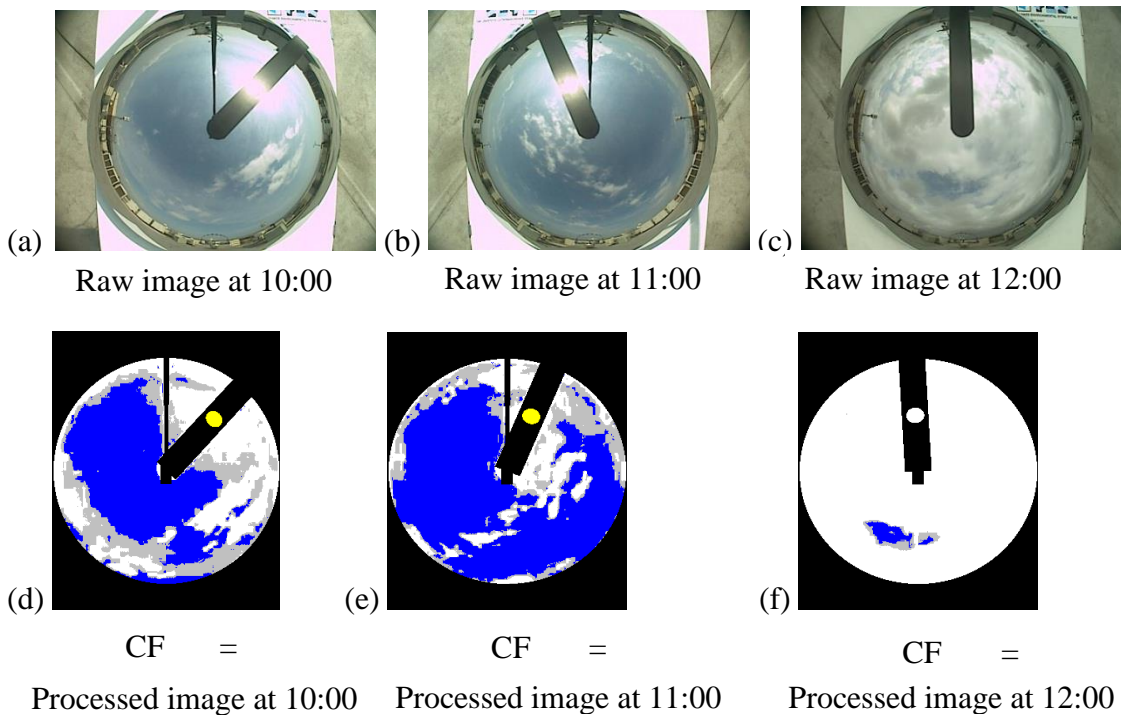


Figure 5.13: Raw TSI image at (a) 10:00 (b) 11:00 and (c) 12:00. Processed TSI image at (d) 10:00 (e) 11:00 and (f) 12:00.

The radiometric profiles showing variation with change in  $CF$  with respect to time of a partly cloudy day are shown in Fig 5.14. The graph shows radiometric profiles from 06:00 to 18:00 but the  $CF$  profile is shown for the period when the TSI was in operation from 10:00 to 13:45.

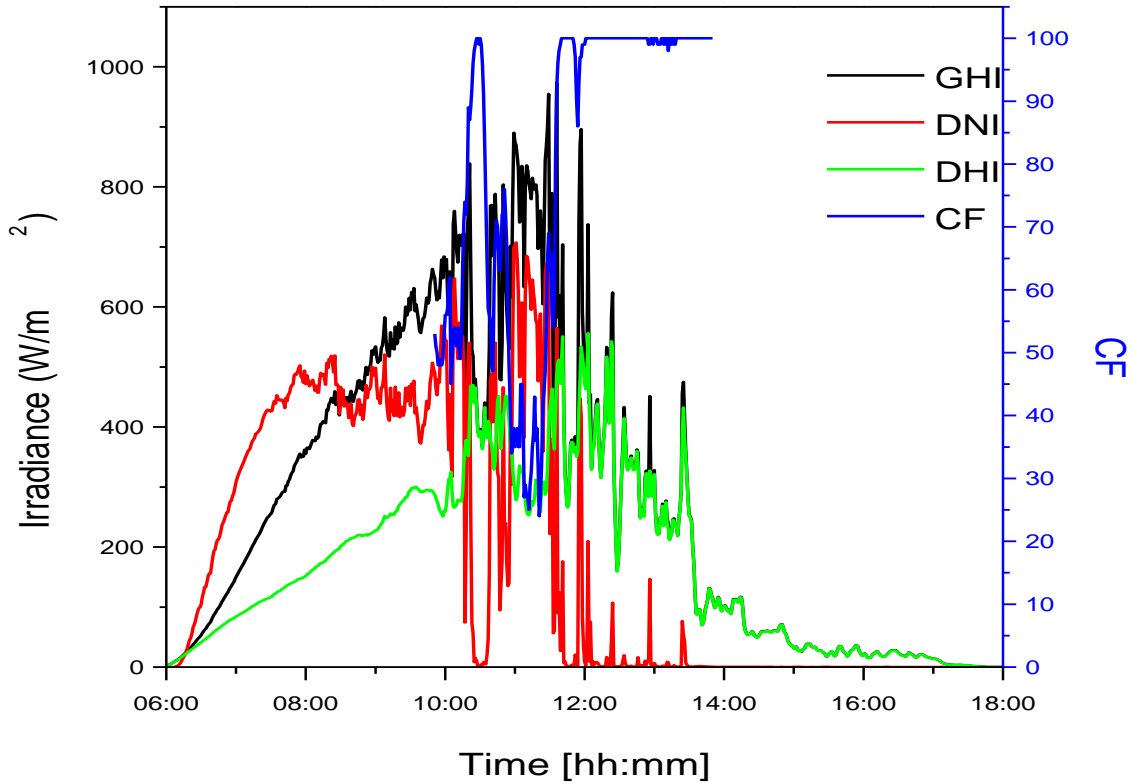


Figure 5.14: Plot of  $CF$  and solar irradiance against time between 06:00 and 18:00 on 10<sup>th</sup> of September 2014.

As seen in Figure 5.14, between 10:00 and 12:00 there is so much variation in both radiometric and  $CF$  profiles and to explain the effects of  $CF$  on radiometric profiles, the figure was redrawn and zoomed in for timeframe between 10:00 and 12:00 as shown in Fig 5.15. According to the Fig 5.15, there was a sharp increase in the  $CF$  doubling from 50% to 100% between the time 10:15 and 10:30.

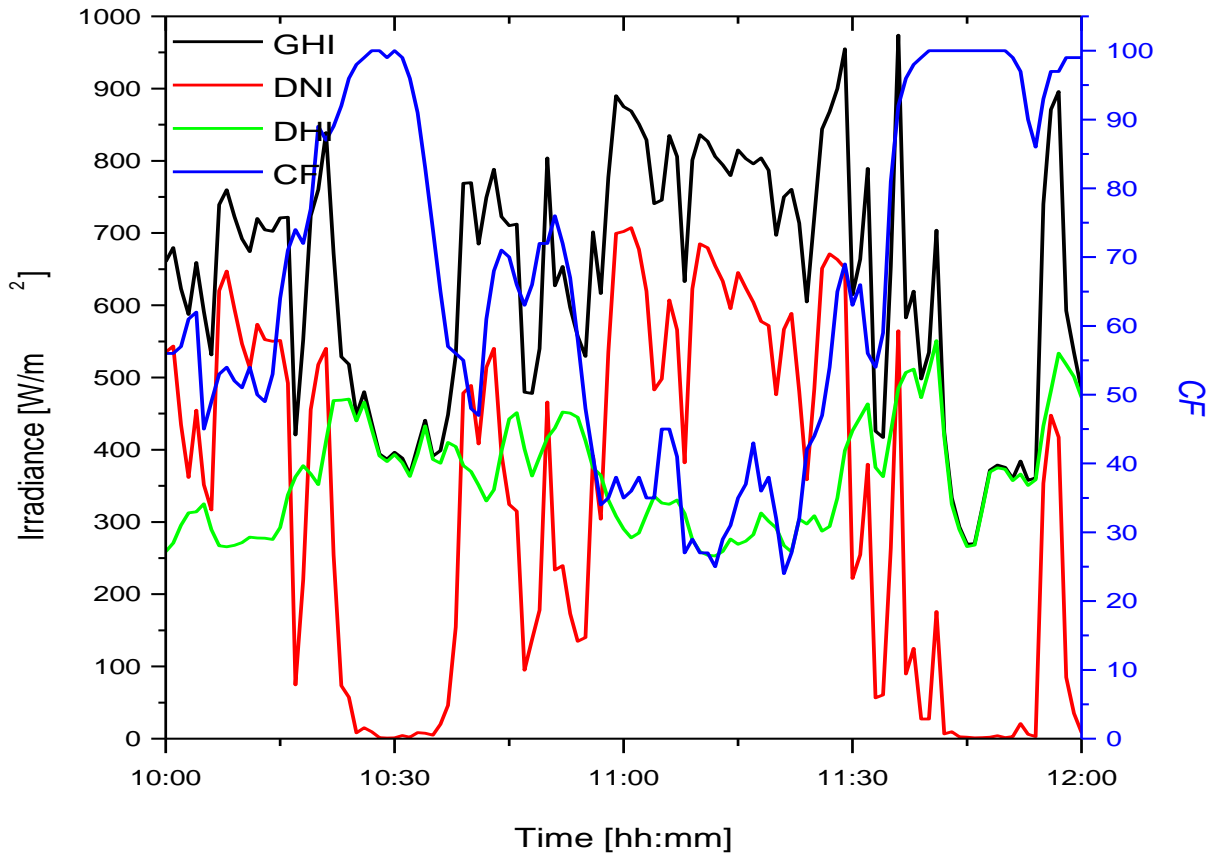


Figure 5.15: Plot of  $CF$  and solar irradiance against time between 10:00 and 12:00 on 10<sup>th</sup> of September 2014.

The sun was not obstructed from 10:15 to 10:23 and obstructed from 10:24 to 10:30 as shown in the TSI images in Fig 5.16. A series of images from the TSI for the period between 10:16 and 10:30 is shown in the Fig 5.16 to substantiate the trend observed between 10:15 and 10:30. The TSI images in Fig 5.16 show clouds building up from the south east direction. There was a spike on the  $DNI$  component between 10:15 and 10:30 reaching a maximum of  $DNI = 550 \text{ W/m}^2$  before it decreased to  $DNI = 0 \text{ W/m}^2$ . This is a result of a passing opaque cloud that had a gap in-between which has allowed the sun rays to pass through resulting in the sudden increase. When

the  $CF$  reached 100% the beam irradiance dropped to  $0 \text{ W/m}^2$  since the sky was overcast and the clouds were blocking the sun's pathway to the radiometers.

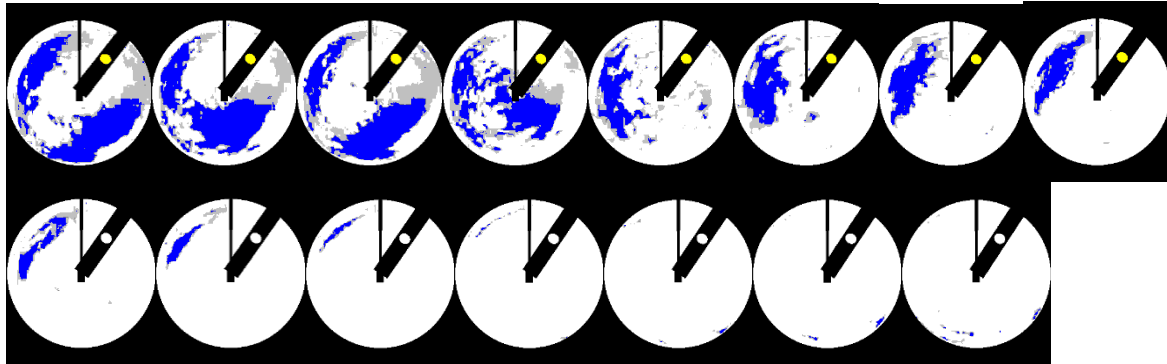


Figure 5.16: Processed 1-minute images between 10:16 to 10:30 (from left to right on the top row and down row also from left to right). The  $CF$  increased from 71% at 10:16 to 100% at 10:30. The temporal variation of images shows cloud evaluation from South East direction.

During the time 10:15 to 10:30 when the  $CF$  increased the diffuse irradiance also increased from  $270 \text{ W/m}^2$  to  $470 \text{ W/m}^2$  due to scattering of solar rays and when the  $CF$  was 100% the diffuse irradiance decreased to  $370 \text{ W/m}^2$ . The diffuse irradiance does not decrease to  $0 \text{ W/m}^2$  since there is always scattered and re-radiated radiation even if the sky is overcast. There is also another sharp decrease in the  $CF$  between 10:30 and 10:45 from 100% to 25%. This decrease results in an increase in the beam irradiance from  $0 \text{ W/m}^2$  to  $550 \text{ W/m}^2$  since the amount of clouds blocking the sun's passage have decreased. There are quite big fluctuations in the  $CF$  between 10:45 to 11:35 with the highest reached  $CF$  being 75% and the lowest  $CF$  being 25%. During these significant fluctuations in the  $CF$ , the beam irradiance was inversely fluctuating in such a way that when the  $CF$  increased, the corresponding beam irradiance would decrease. For the same time period, it is seen that the diffuse irradiance increased with increasing  $CF$  and decrease with decreasing  $CF$ , but in smaller magnitudes as compared to that of the beam irradiance.

However, there is a dip in the  $CF$  between 11:45 and 12:00 from 100% to 85%, resulting in a spike on the beam irradiance increasing from  $0 \text{ W/m}^2$  to  $450 \text{ W/m}^2$ . Even though the  $CF$  may be as high as 85% there are instances when the sun is not obstructed by the clouds allowing passage

of sun rays to the radiometers hence an increase in the beam irradiance. This is evidenced by the images shown in Fig 5.17.

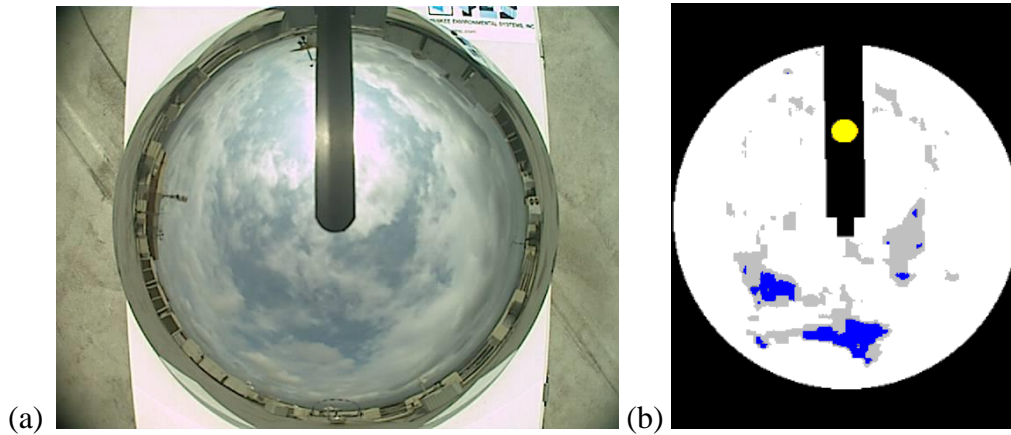


Figure 5.17: Raw sky image (a) and processed image (b) at 11:56. The  $CF$  was 97% and the sun was not obstructed.

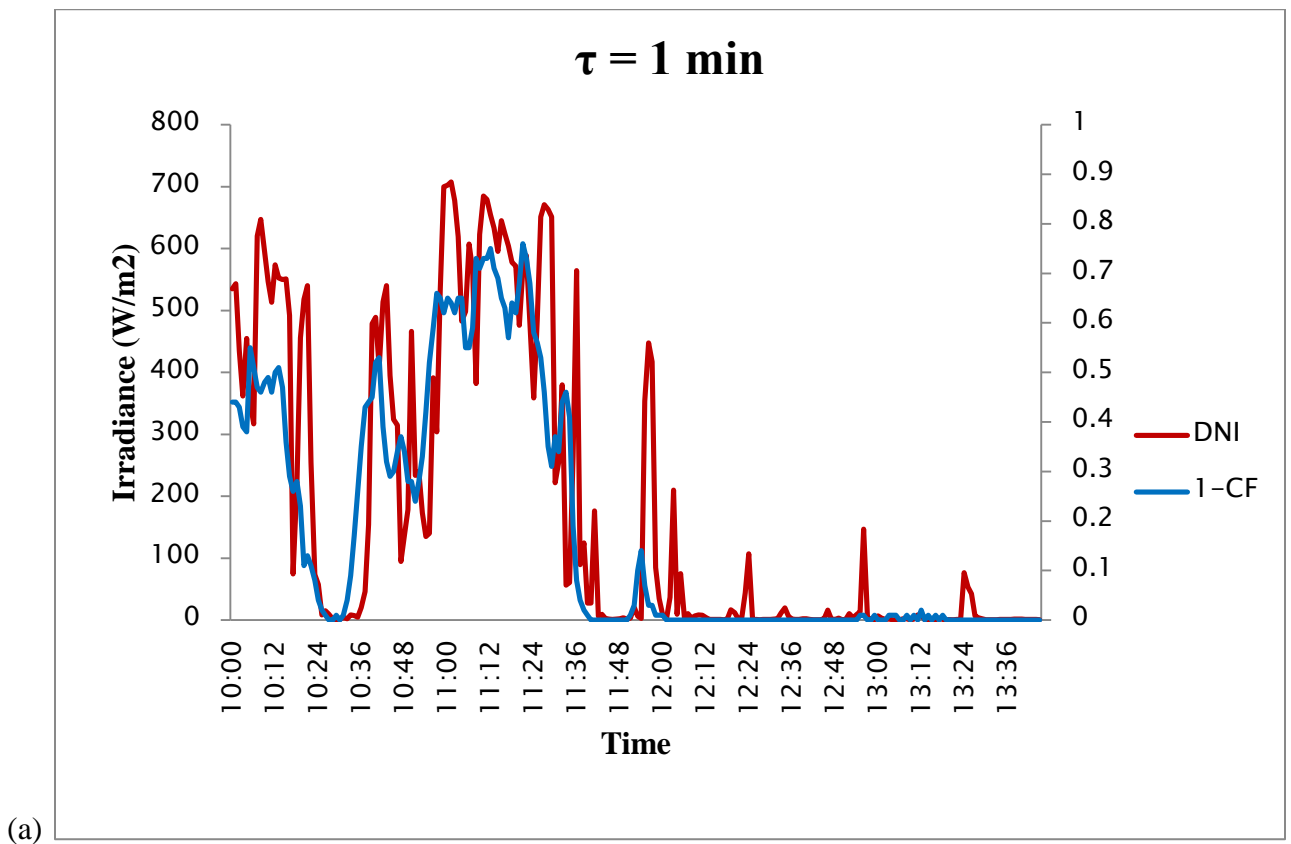
From the image in Fig 5.17 it is evident that even though the  $CF$  is high, the sun is not obstructed hence a yellow sunspot on the shadowband of the processed image. This also reveals that the clouds that are closer to the sun have gaps between them, allowing the sun rays to pass through. The presence of the unobstructed sun in the vicinity of the clouds increased chances of scattering hence there is also an increase of the diffuse irradiance from  $360 \text{ W/m}^2$  to  $530 \text{ W/m}^2$ . This increase in the diffuse irradiance resulted in an ultimate increase in the global irradiance from  $360 \text{ W/m}^2$  to  $900 \text{ W/m}^2$ .

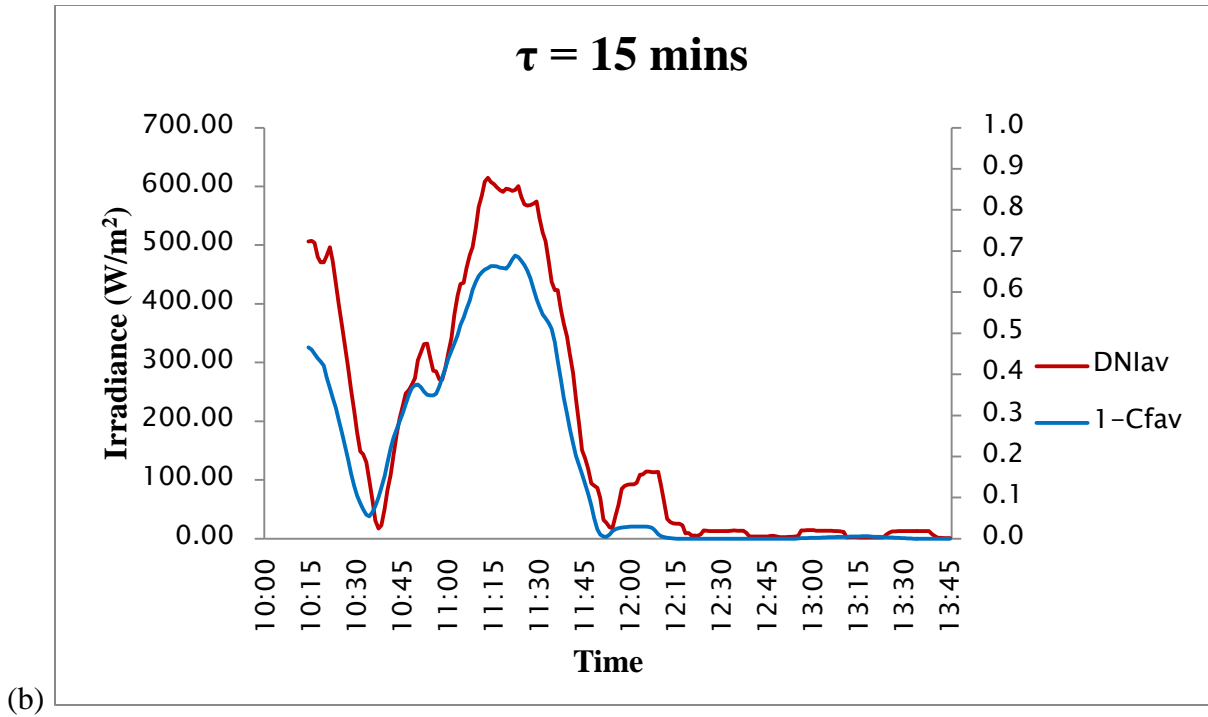
### Different time scale analysis for 10 September 2014

#### a) Between $DNI$ and $1 - CF$

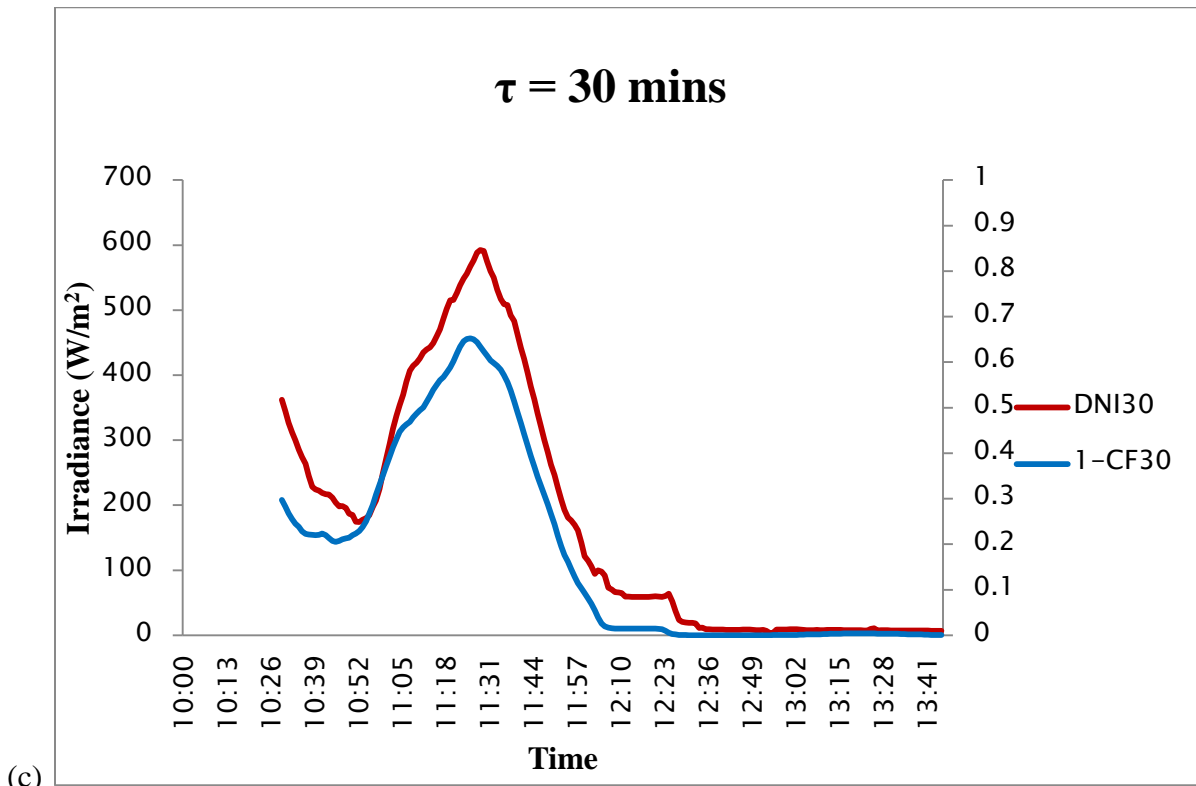
Centred moving average  $DNI$  and  $1 - CF$  against time graphs were plotted for different time-averaging time-scales for the 10th of September 2014 in Fig 5.18. The day of the 10th of September 2014 was chosen since it is a partly cloudy day, which will give a clear trend of the effect of  $CF$  on the beam irradiance. Instead of using  $CF$ , the graph is using  $1 - CF$  because it quantifies the sky that is not covered by clouds and this may be referred to as the sky's transmissivity. The more transparent sky is the higher the  $DNI$  component will be recorded. The

different time-averaging that was used is 15 minutes shown in Fig 5.18b, 30 minutes shown in Fig 5.18c and 1 hour is shown in Fig 5.18d which were compared to the 1 minute plot shown in Fig 5.18a. This time-averaging was selected on the basis that bigger time-averaging of hours end up smoothing up the graphs reducing the responsivity of the graph. The different time-averaging show different smoothing effect on the data and hence a clear pattern is obtained. It can be noted that as the time-averaging increases, the responsiveness of the graph is lowered as shown in Fig 5.18d. *DNI* component increased as  $1 - CF$  increased as expected that when there are fewer clouds more beam irradiance passes through to the radiometers.





(b)



(c)

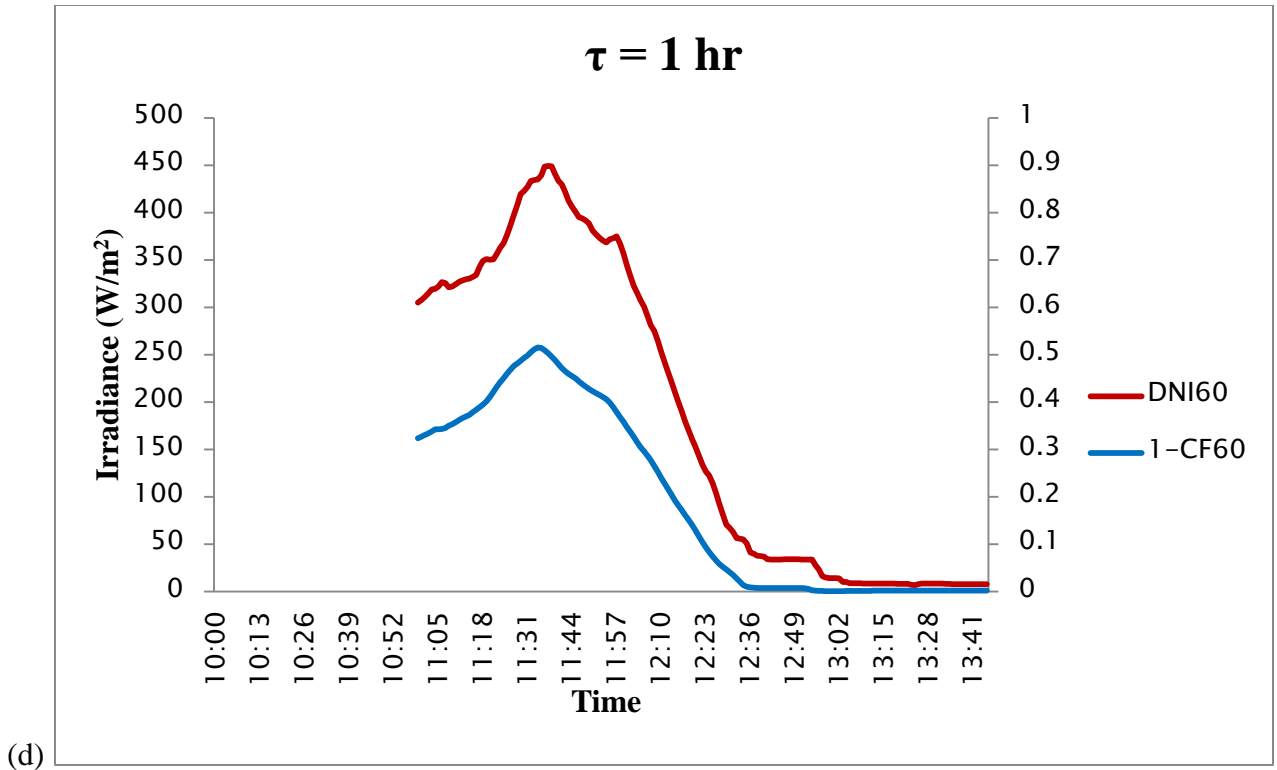
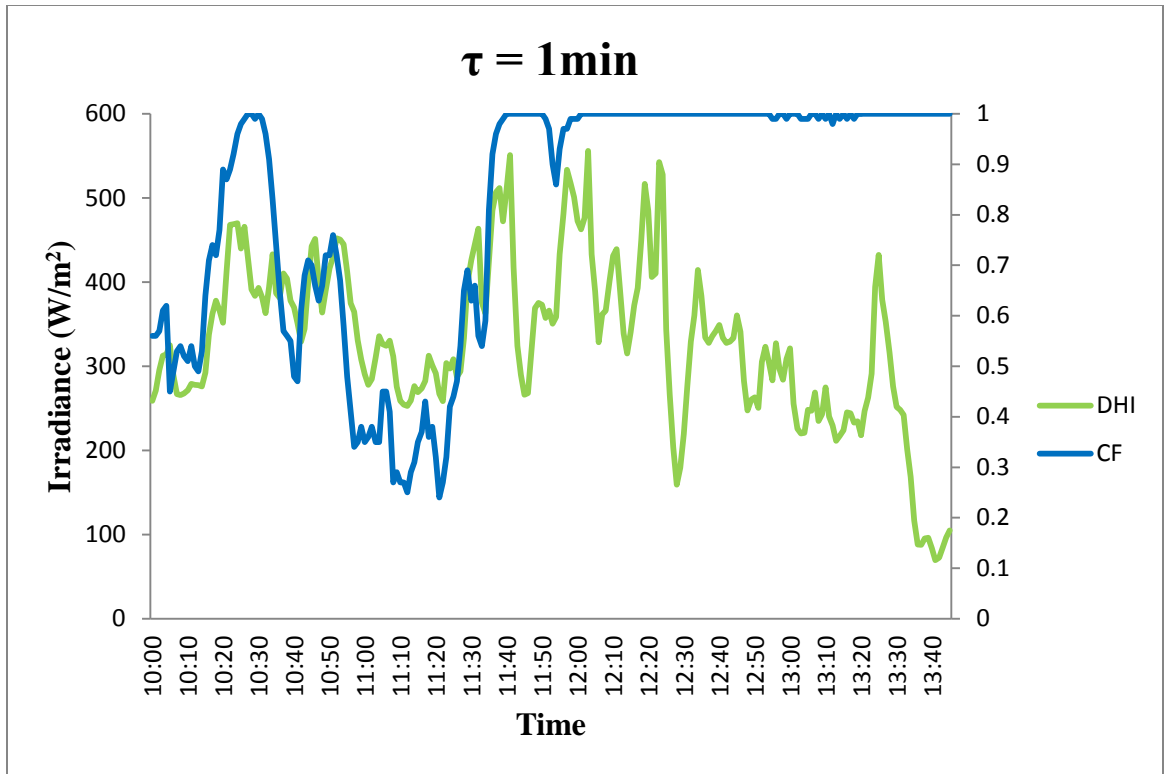


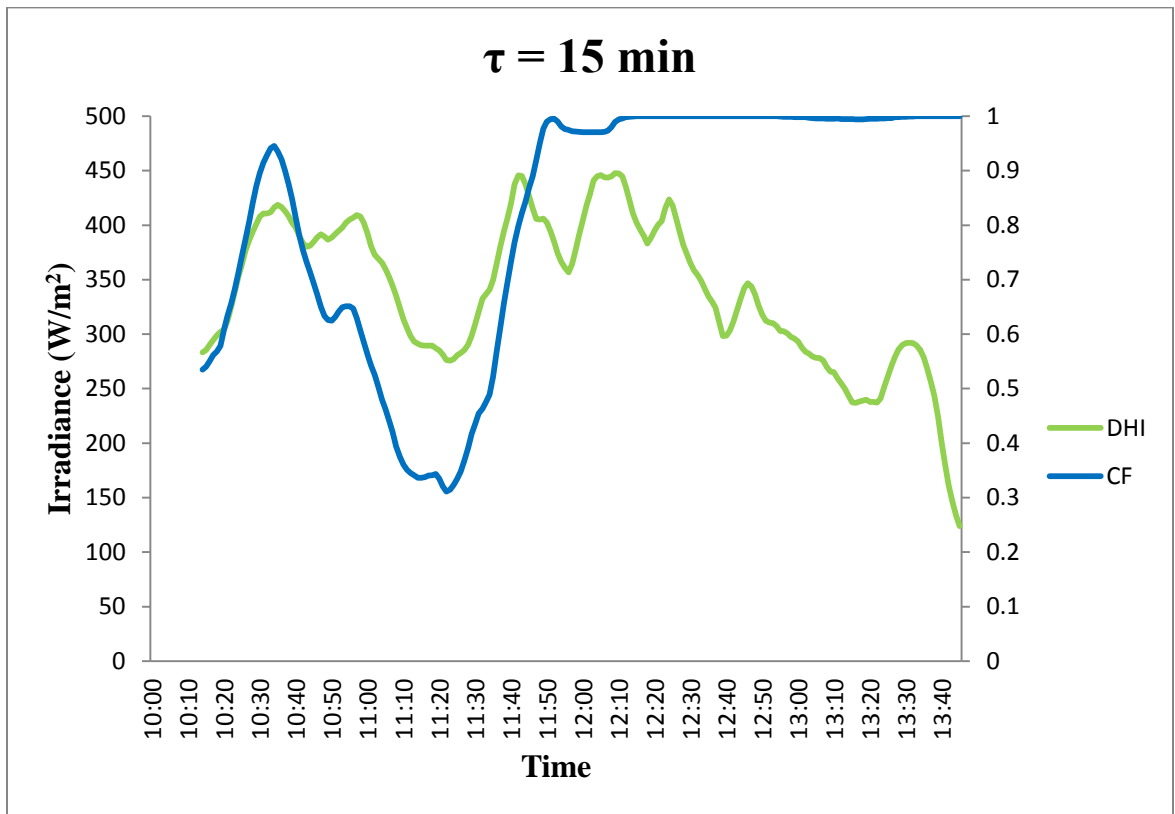
Figure 5.18: Plot of centred moving average *DNI* and  $1 - CF$  against time for different time-averaging time-scales  $\tau$

### b) Between *DHI* and *CF*

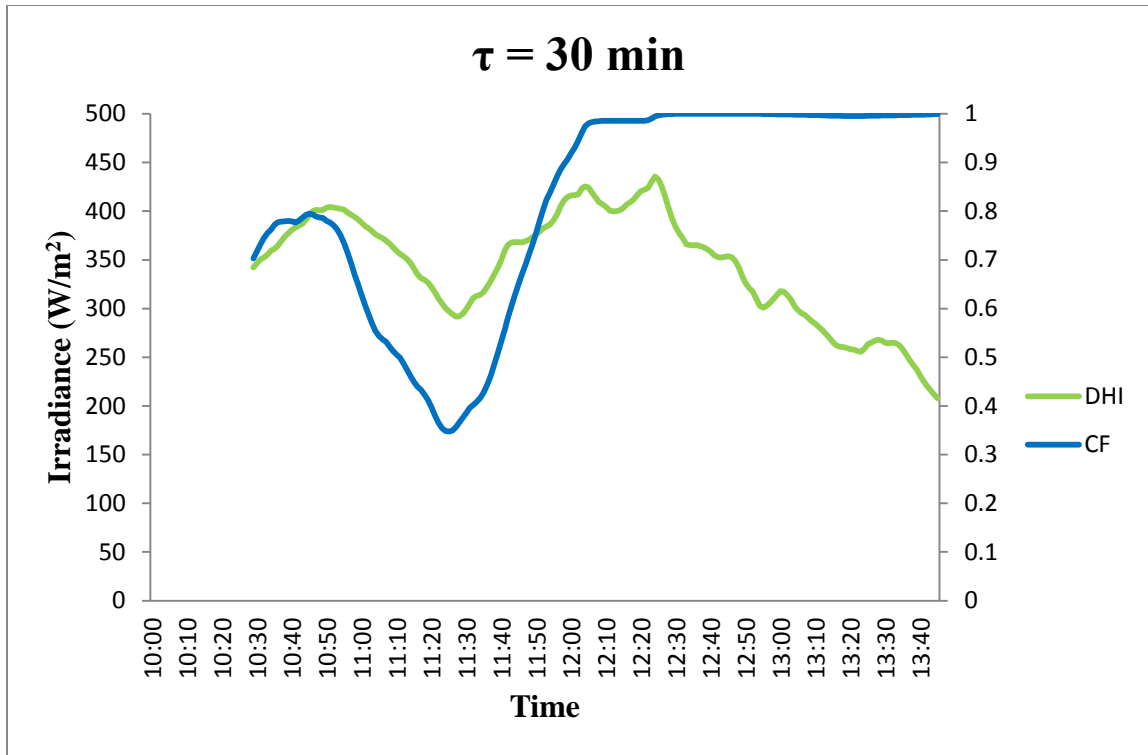
Centred moving average *DHI* and *CF* against time graphs were plotted for different time-averaging time-scales for the 10th of September 2014 in Fig 5.19. The day 10<sup>th</sup> September 2014 was chosen since it is a partly cloudy day, which gives a clear trend of the effect of *CF* on the diffuse irradiance. The lower *CF* results in low *DHI* received by the radiometer due to less scattering of radiation since the amount of clouds will be low. The different time-average that was used is 15 minutes shown in Fig 5.19b, 30 minutes shown in Fig 5.19c and 1 hour shown in Fig 5.19d which were compared to the 1 minute plot shown in Fig 5.19a. It can be noted that as the time-averaging increases, the responsiveness of the graph is lowered as shown in Fig 5.19d. There is no uniform relationship between the *CF* and diffuse irradiance received by the radiometers.



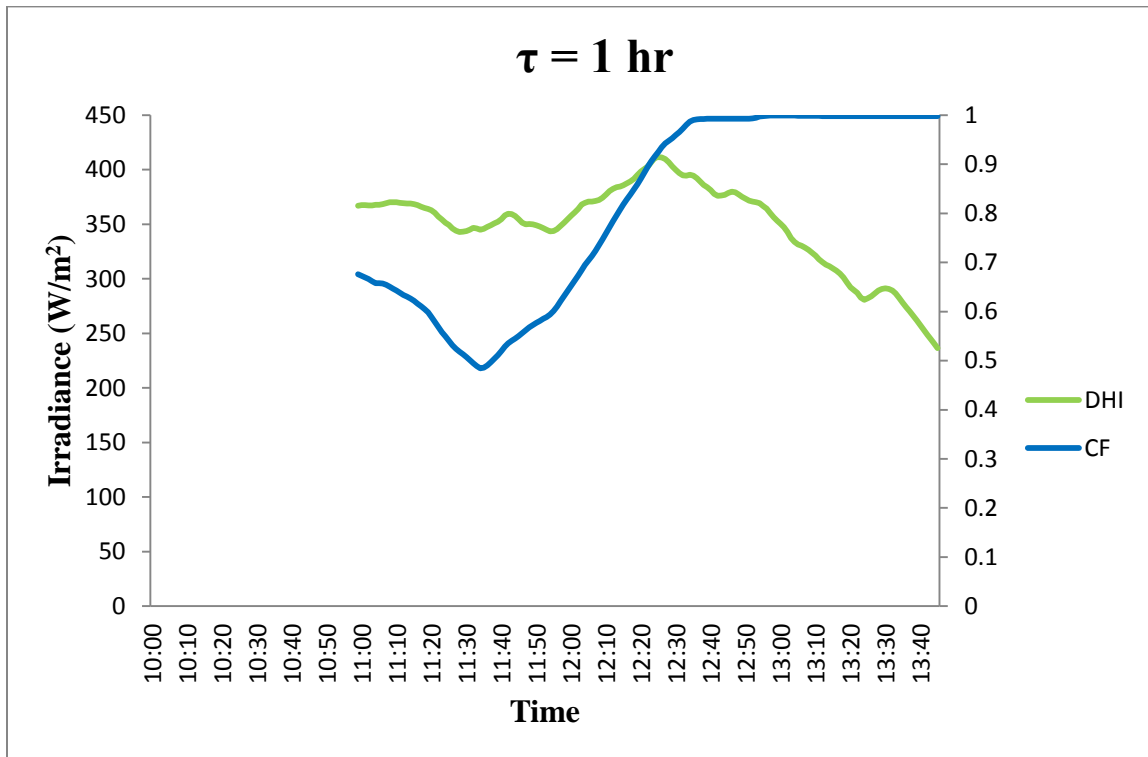
(a)



(b)



(c)



(d)

Figure 5.19: Plot of centred moving average *DHI* and *CF* against time for different time-averaging time-scales  $\tau$

## 5.2 Statistical Results

The quantitative aspect of the data is dealt with in this section. The time-averaged values of  $CF$  were correlated with the corresponding time-averaged  $GHI/GHI_o$ ,  $GHI/GHI_c$ ,  $DNI/DNI_o$ ,  $DNI/DNI_c$  and  $DHI/DHI_c$  for linear regression analysis. The time-averages that will be considered are 1 minute, 15 minutes, 1 hour and 4 hours, which will be compared to the 1 minute data. The entire data will be separated and analysed separately as follows, graphs for averaging over 1 minute, 15 minutes, 1 hour and 4 hours. Linear regression analysis was employed on all scatter plots from averaging over 15 minutes to 4 hours and the linear regression equation was stated. Comparisons were made mainly on correlation coefficients  $R$  and coefficient of determination  $R^2$ . A linear relationship was only affirmed if the coefficient of determination,  $R^2$  is greater than or equal to 0.8.

### 5.2.1 Linear regression plots for 1 minute data.

The total data points that were used for all the clearness indices of 1 minute data is 3960. In this data, the lowest  $CF$  of 0.03 was recorded which is 33 times smaller than the highest possible  $CF = 1$ . A linear regression of data was performed between the  $CF$  and a specific clearness index in the next subsections.

#### $k_t$ vs $CF$

A minimum clearness index  $k_t$  of 0.0 was recorded mainly when the sky was totally overcast with  $CF = 1$  and the highest registered clearness index  $k_t$  was 1.10. Fig 5.20 shows a scatter plot of  $k_t$  vs  $CF$  for 1 minute data and clearly there is no linear relationship of the variables in this graph.

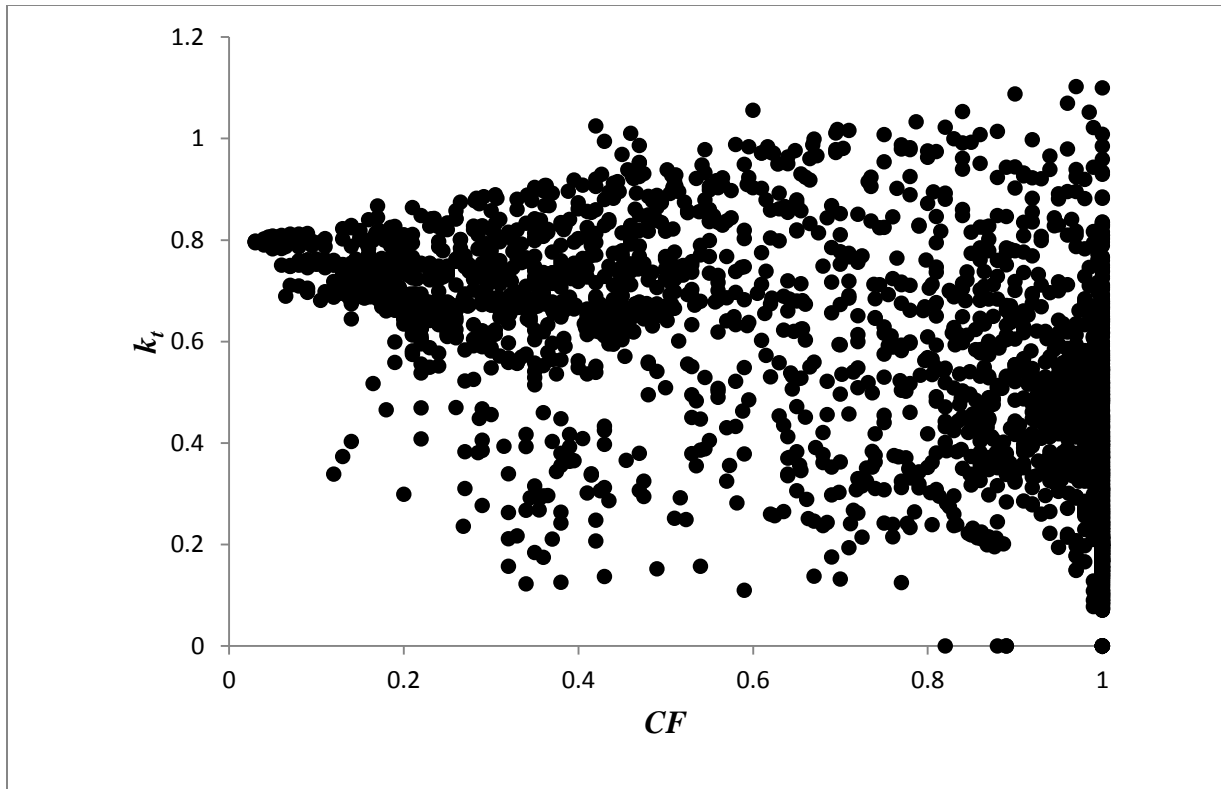


Figure 5.20: Scatter plot of  $k_t$  as a function of the total  $CF$  for the entire 1 minute dataset.

The graph for  $k_t$  vs  $CF$  for the 1 minute average data in Fig 5.20 shows that the values of  $k_t$  that are greater than 1 are mostly found in the  $CF$  range between 0.8 and 1.0. There is no linear relationship of the variables in this graph.

#### **$k_c$ vs $CF$**

Fig 5.21 shows a scatter plot of measured-to-clear sky global radiation ( $k_c$ ) as a function of the total  $CF$  for the entire 1 minute dataset. A minimum clearness index  $k_c$  of 0.0 was also obtained mainly when  $CF = 1$  and the highest obtained clearness index  $k_c$  was 1.1439996. As seen in Fig 5.21 the values of  $k_c > 1$  are found in the whole range of  $CF$  values, but they are more on the right-hand side of the graph. There is no linear relationship of the variables in this graph.

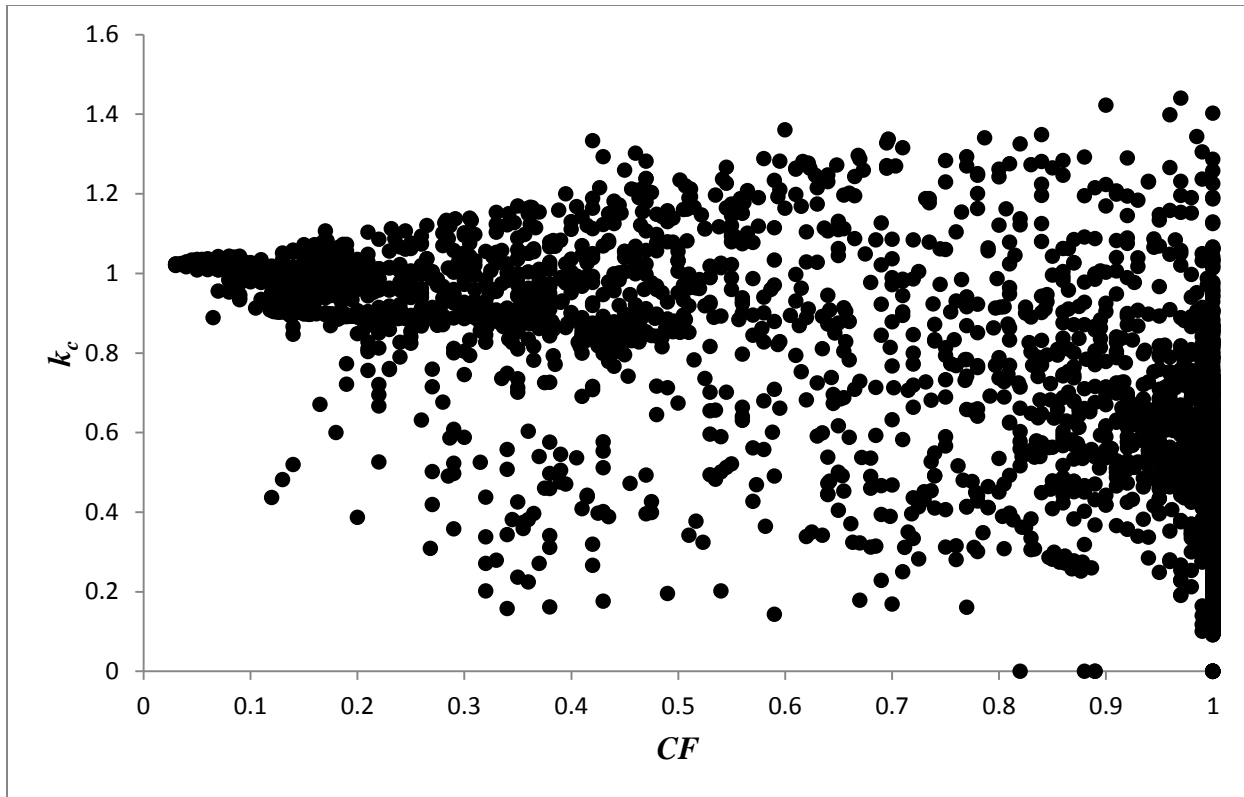


Figure 5.21: Scatter plot of  $k_c$  as a function of the total  $CF$  for the entire 1 minute dataset.

### $k_b$ vs $CF$

Fig 5.22 shows a scatter plot of measured-to-extraterrestrial beam irradiance ( $k_b$ ) as a function of the total  $CF$  of the entire 1 minute dataset. Fig 5.22 shows that the values of  $k_b$  are less than 0.7 and these higher values of  $k_b$  are mostly found in the  $CF$  range between 0.0 and 0.5. A minimum clearness index  $k_b$  of 0.0 was obtained mainly when the sky was totally overcast with  $CF = 1$  and the highest clearness index  $k_b$  of 0.690761. High  $k_b$  values are also noted on the graph even for very high  $CF$  values which is a possibility of gaps in the clouds even when the sky is overcast. However, there are those rare cases when the  $CF$  is very low and the  $k_b$  values are also low which is a situation whereby there are a few clouds but they will be obscuring the pyrheliometer from the sunlight. There is no linear relationship of the variables in this graph.

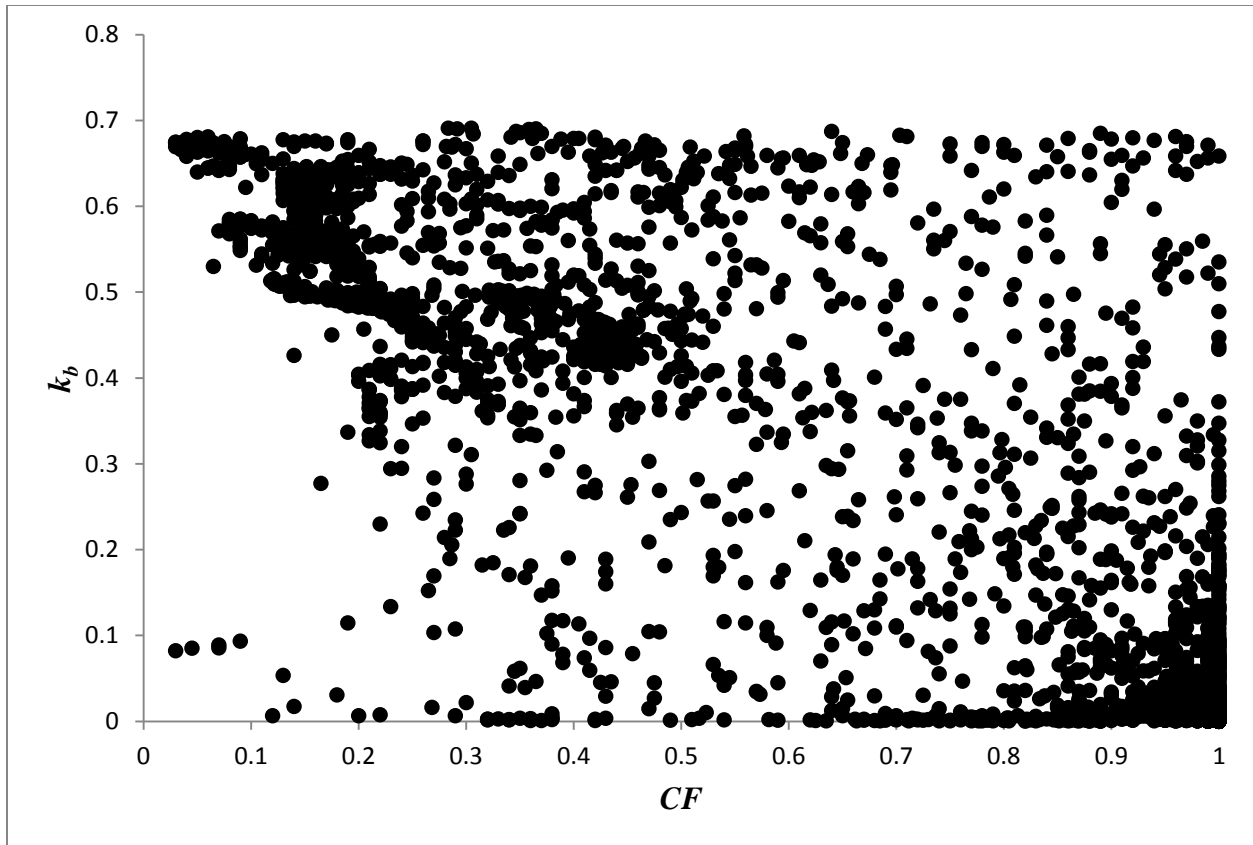


Figure 5.22: Scatter plot of  $k_b$  against  $CF$  for the entire 1 minute dataset.

### ***$DNI/DNI_c$ vs $CF$***

Fig 5.23 shows a scatter plot of measured-to-clear sky beam irradiance as a function of the total  $CF$  for the entire 1 minute dataset. According to Fig 5.23 a minimum clearness index  $DNI/DNI_c$  of 0.0 was obtained mainly with  $CF = 1$  and the value  $DNI/DNI_c > 1$  are present with the highest  $DNI/DNI_c$  value is 1.069621 and its widely spread across the whole range of  $CF$  values, but they are more on the left-hand side of the graph and minimum  $DNI/DNI_c$  values are more on the right-hand side. There is no linear relationship of the variables in this graph.

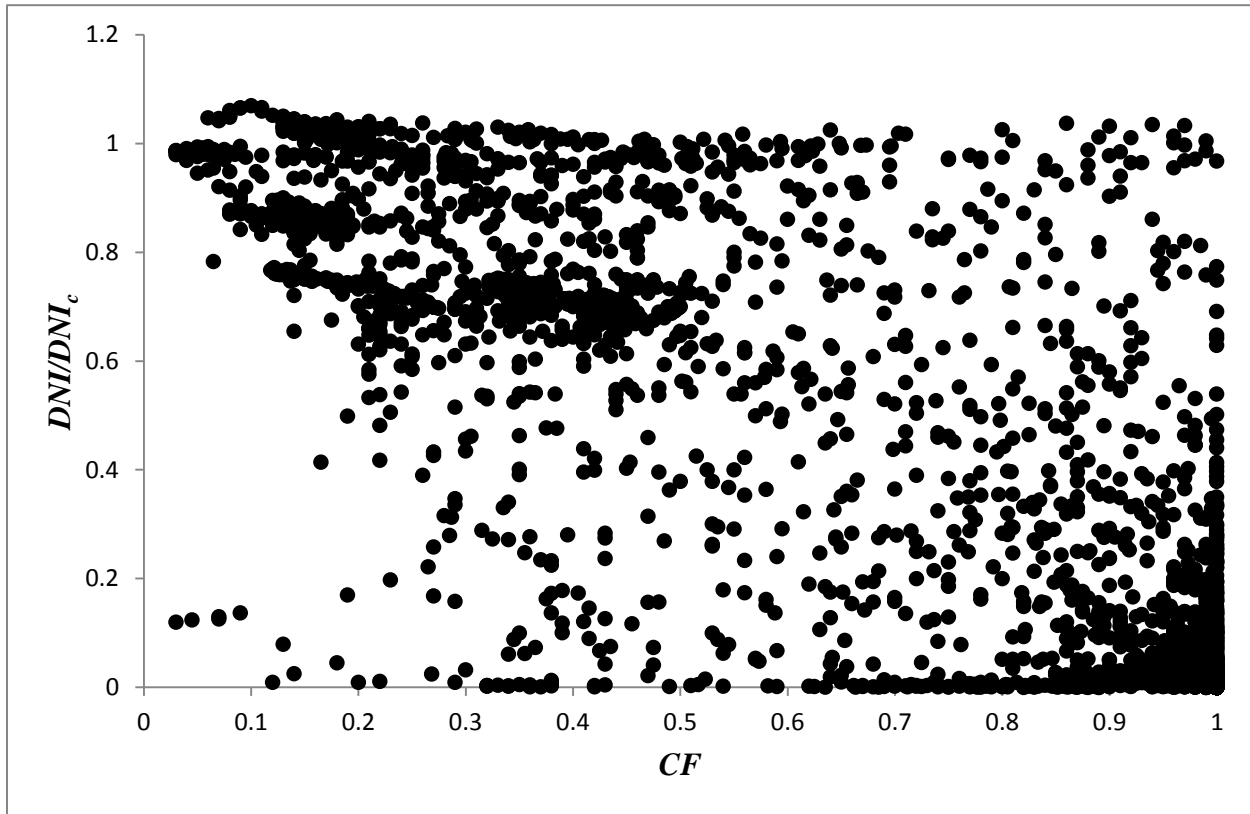


Figure 5.23: Scatter plot of  $DNI/DNI_c$  as a function of the total  $CF$  for the entire 1 minute dataset.

### ***DHI/DHI<sub>c</sub> vs CF***

The scatter plot of measured-to-clear sky diffuse irradiance as a function of the total  $CF$  for the entire 1 minute dataset is shown in Fig 5.24. A minimum clearness index  $DHI/DHI_c$  of 0.70734 was obtained for a wide range of  $CF$  and the highest  $DHI/DHI_c$  value of 6.0094. The graph for  $DHI/DHI_c$  vs  $CF$  for the 1minute data in Fig 5.24 shows that the values of  $DHI/DHI_c$  are as high as 6.0 and these higher values of  $DHI/DHI_c$  are mostly found in the  $CF$  range between 0.8 and 1.0 because scattering of irradiation is more pronounced when there are more clouds. The highest  $DHI/DHI_c$  values are more on the left-hand side of the graph and minimum  $DHI/DHI_c$  values are more on the right-hand side. There is no linear relationship of the variables in this graph.

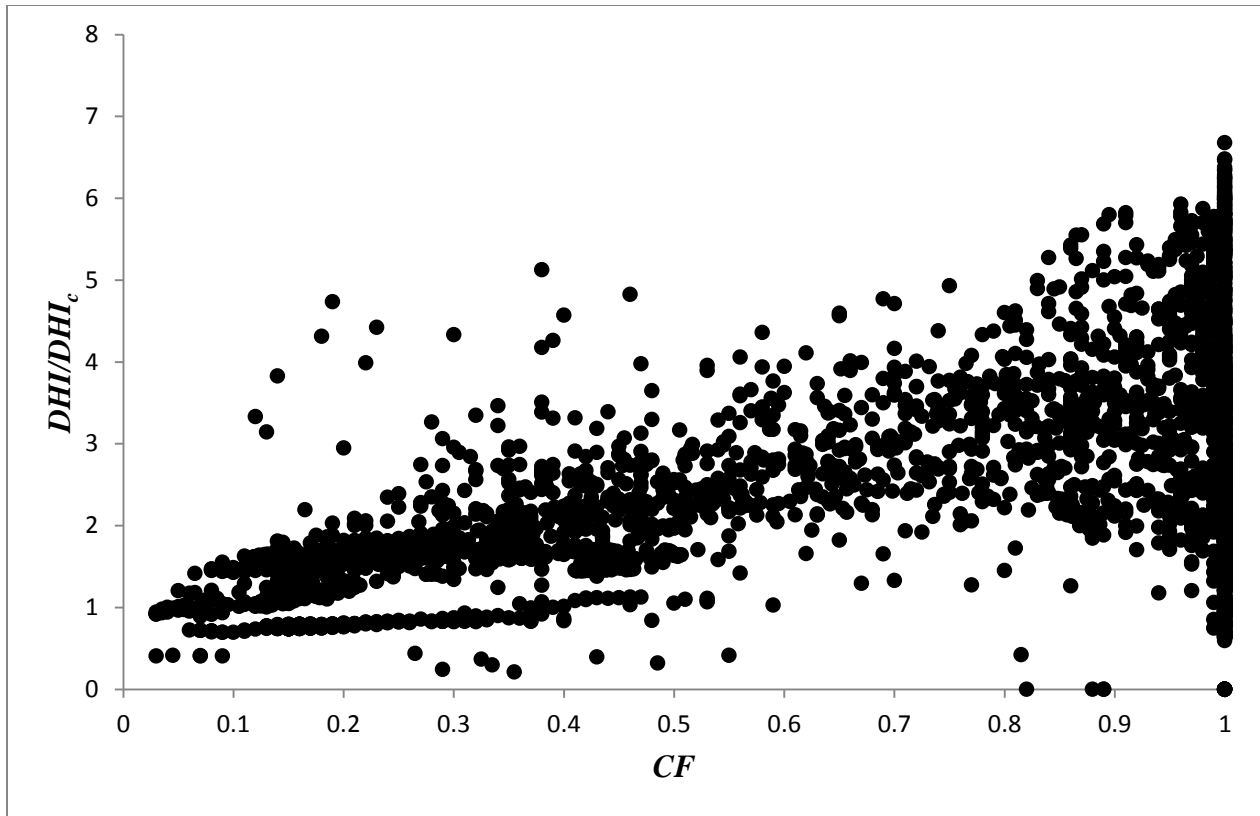


Figure 5.24: Scatter plot  $DHI/DHI_c$  as a function of the total  $CF$  for the entire 1 minute dataset.

### 5.2.2 Linear regression plots for 15 minutes-averaging data

The total data points that were used for all the clearness index values of 15 minutes-averaging data are 272. For this data, the lowest  $CF$  of 0.05 was registered which is 20 times smaller than the highest  $CF = 1$  that was registered. A linear regression of data was performed between the  $CF$  and a specific clearness index in the next subsections.

#### $k_t$ vs $CF$

Fig 5.25 shows a scatter plot of  $k_t$  as a function of the total  $CF$  for the entire 15 minute dataset. A minimum clearness index  $k_t$  of 0.075 was obtained mainly when the sky was totally overcast with  $CF = 1$  and the highest clearness index obtained was 0.9566.

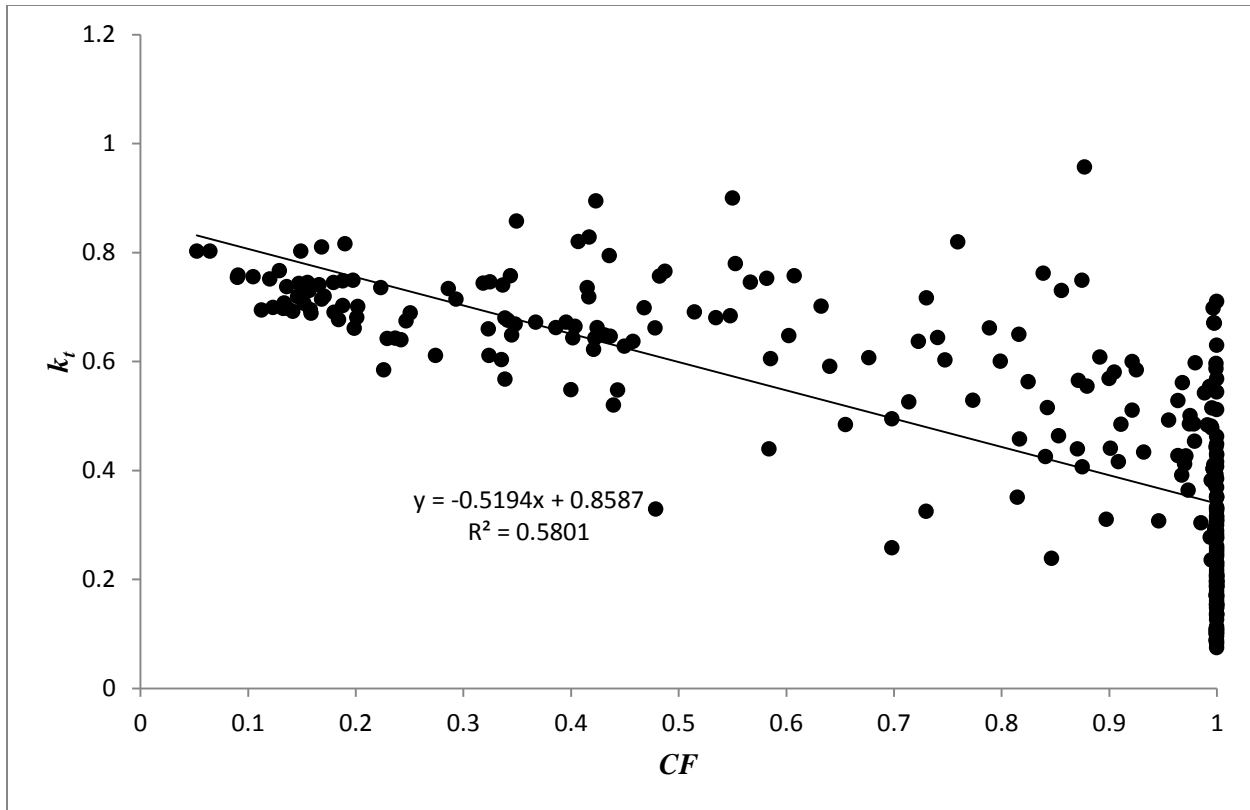


Figure 5.25: Scatter plot of  $k_t$  function of the total  $CF$  for the entire dataset.

Linear regression analysis of data was carried out as shown in Fig 5.25 and equation 5.1 was obtained:

$$k_t = 0.8587 - 0.5194 \frac{\bar{c}}{100} \quad (5.1)$$

For the whole data points used, the correlation coefficient for  $k_t$  was found to be  $R = -0.7616$  and the coefficient of determination was found to be  $R^2 = 0.5801$ .

### $k_c$ vs $CF$

Fig 5.26 shows a scatter plot of  $k_c$  as a function of the total  $CF$  for the entire 15 minute dataset. A minimum clearness index  $k_c$  of 0.097044 was also obtained mainly with  $CF = 1$  and the highest obtained clearness index  $k_c$  of 1.2533.

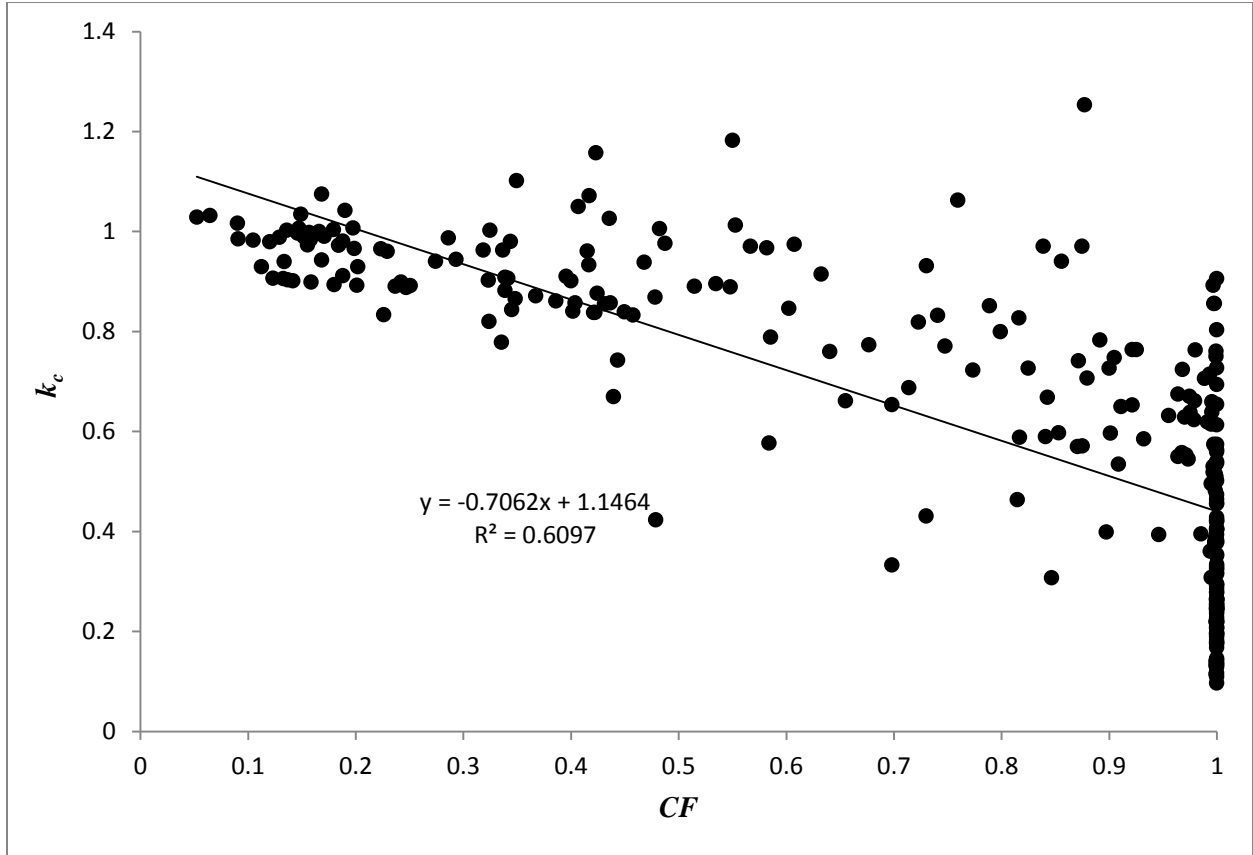


Figure 5.26: Scatter plot of  $k_c$  as a function of the total  $CF$  for the entire dataset.

Linear regression analysis of data was carried out as shown in Fig 5.26 and equation 5.2 was obtained:

$$k_c = 1.1464 - 0.7062 \frac{\bar{c}}{100} \quad (5.2)$$

For the whole data points used, the correlation coefficient for  $k_c$  values was found to be  $R = -0.7808$  and the coefficient of determination was found to be  $R^2 = 0.6097$ . As we increase the averaging time, this reduces the data points that exhibit enhancements and this shows that when you need to investigate solar irradiation enhancements, shorter time-frames in the order of 1 minute should be considered.

### $k_b$ vs $CF$

Fig 5.27 shows a scatter plot of  $k_b$  as a function of the total  $CF$  for the entire 15 minute dataset. A minimum clearness index  $k_b$  of 0.0 was recorded mainly when the sky was totally overcast with  $CF = 1$  and the highest clearness index  $k_b$  of 0.66567.

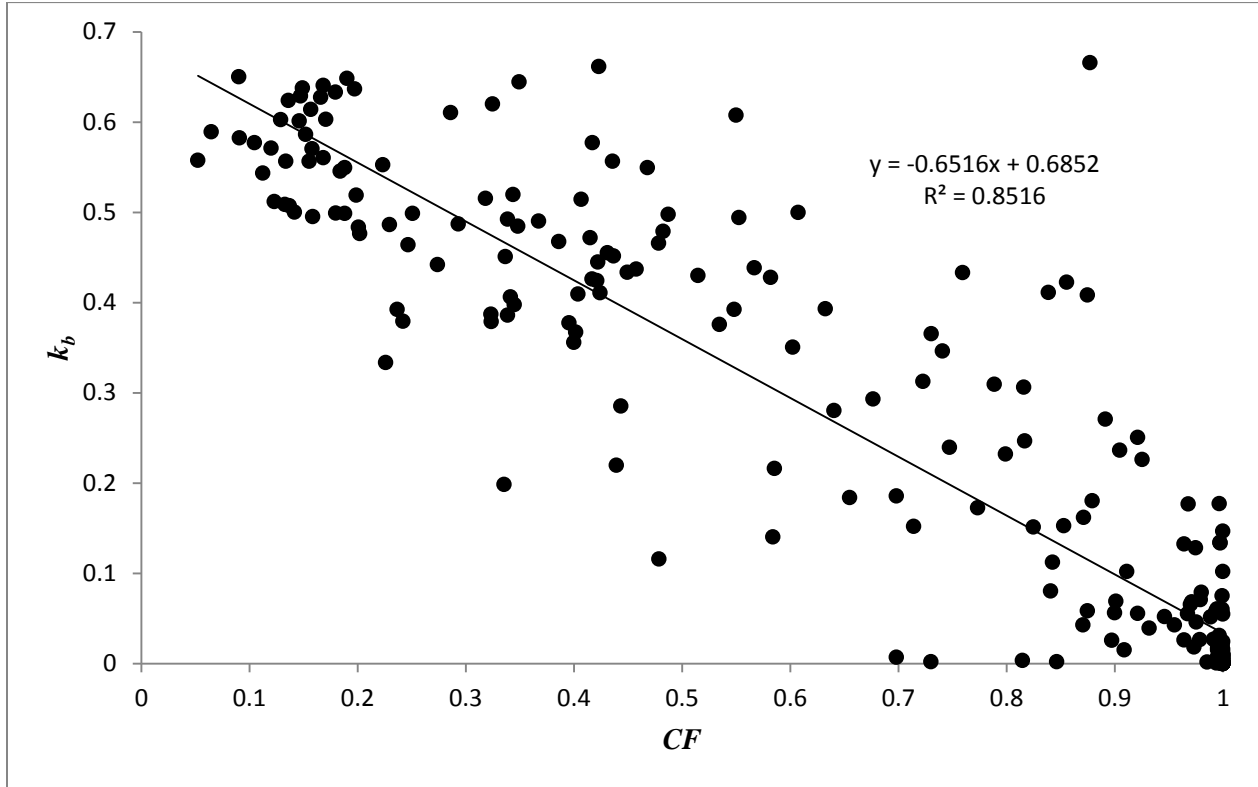


Figure 5.27: Scatter plot of  $k_b$  as a function of the total  $CF$  for the entire dataset.

Linear regression analysis of data was carried out as shown in Fig 5.27 and equation 5.3 was obtained:

$$k_b = 0.6852 - 0.6516 \frac{\bar{c}}{100} \quad (5.3)$$

For the whole data points used, the correlation coefficient for  $k_b$  was found to be  $R = -0.9228$  and the coefficient of determination was found to be  $R^2 = 0.8516$ .

### *DNI/DNI<sub>c</sub> vs CF*

Fig 5.28 shows a scatter plot of  $DNI/DNI_c$  as a function of the total  $CF$  for the entire 15 minute dataset. A minimum clearness index  $DNI/DNI_c$  of 0.0 was also recorded mainly with  $CF = 1$  and the highest recorded clearness index  $DNI/DNI_c$  of 1.0539.

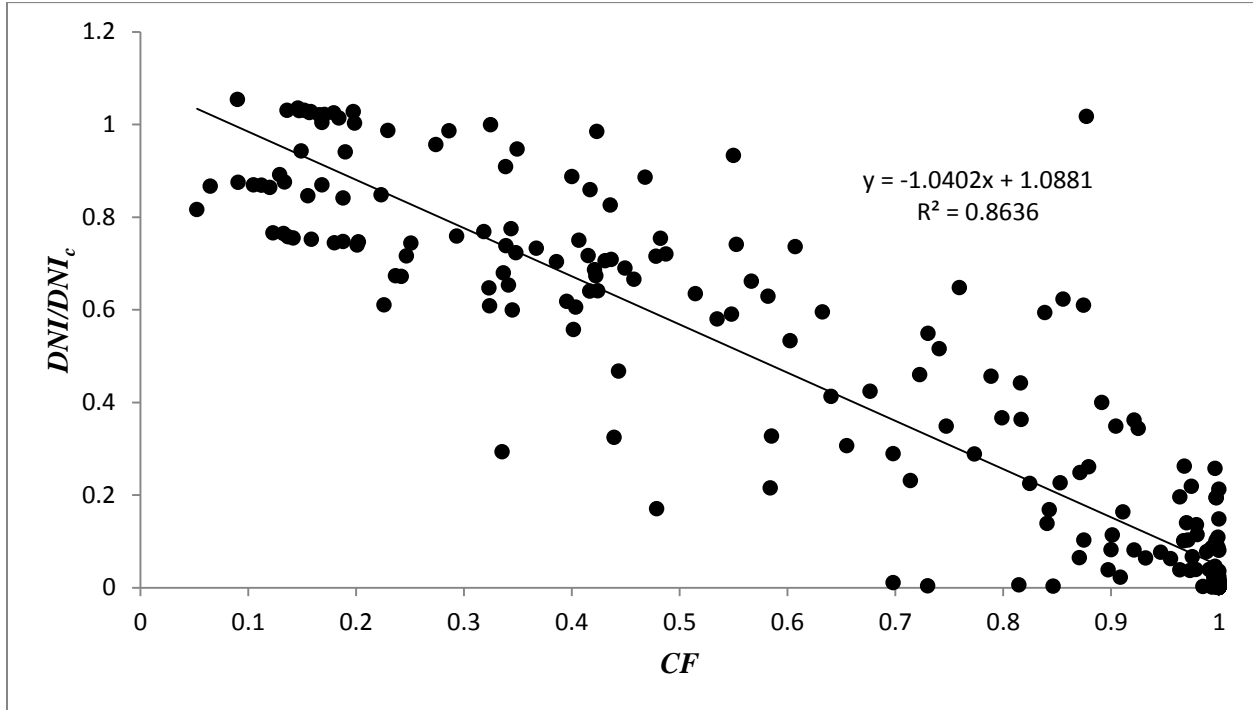


Figure 5.28: Scatter plot of  $DNI/DNI_c$  as a function of the total  $CF$  for the entire dataset.

Linear regression analysis of data was carried out as shown in Fig 5.28 and equation 5.4 was obtained:

$$\frac{DNI}{DNI_c} = 1.0881 - 0.0402 \frac{\bar{c}}{100} \quad (5.4)$$

For the whole data points used, the correlation coefficient for  $DNI/DNI_c$  values was found to be  $R = -0.9293$  and the coefficient of determination was found to be  $R^2 = 0.8636$ .

## *DHI/DHI<sub>c</sub>* vs *CF*

Fig 5.29 shows a scatter plot of  $DHI/DHI_c$  as a function of the total  $CF$  for the entire 15 minute dataset. A minimum clearness index  $DHI/DHI_c$  of 0.70734 was recorded for a wide range of  $CF$  and the highest  $DHI/DHI_c$  value of 6.0094.

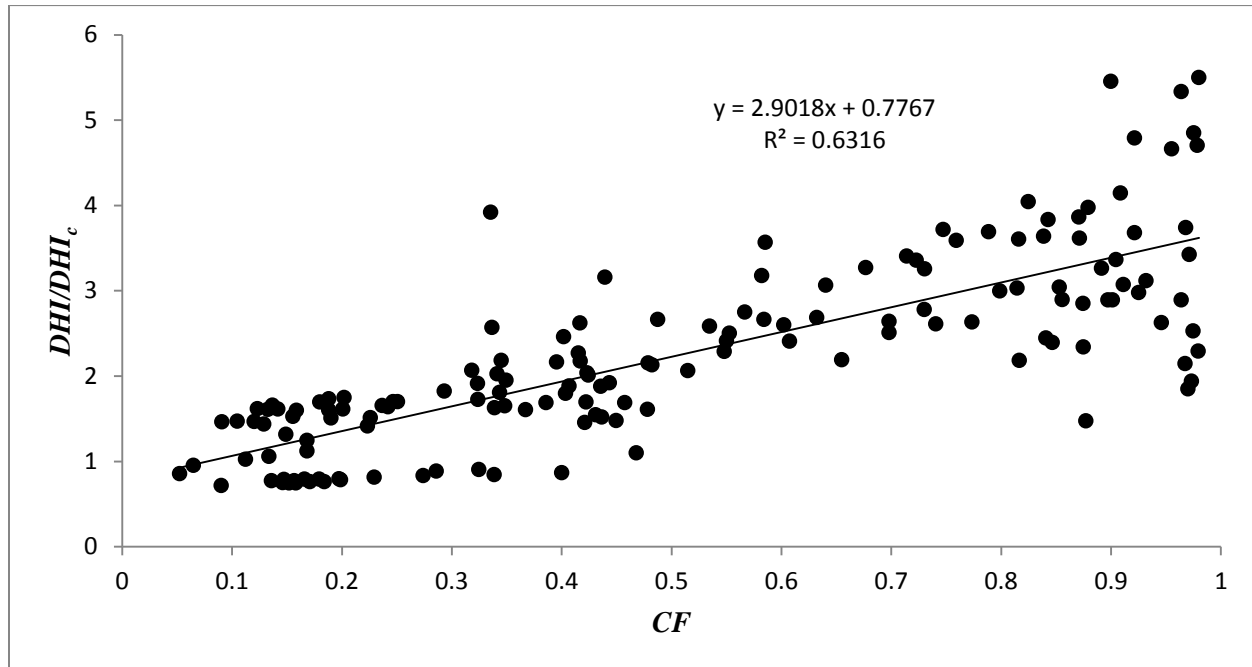


Figure 5.29: Scatter plot of  $DHI/DHI_c$  as a function of the total  $CF$  for the entire dataset.

Linear regression analysis of data was carried out as shown in Fig 5.29 and equation 5.5 was obtained:

$$\frac{DHI}{DHI_c} = 0.7767 + 2.9018 \frac{\bar{c}}{100} \quad (5.5)$$

For the whole data points used, the correlation coefficient for  $DHI/DHI_c$  was found to be  $R = 0.4920$  and the coefficient of determination was found to be  $R^2 = 0.2421$ .

### **5.2.3 Linear regression plots for 1 hour-averaging data.**

The total data points that were used for all the clearness indices values of 1 hour averages data are 72. In this data, the lowest  $CF$  of 0.12 was recorded which is about 10 times smaller than the

highest  $CF = 1$  that was recorded. A linear regression of data was performed between the  $CF$  and a specific clearness index in the next subsections.

### $k_t$ vs $CF$

Fig 5.30 shows a scatter plot of  $k_t$  as a function of the total  $CF$  for the entire 15 minute dataset. A minimum clearness index  $k_t$  of 0.090 was recorded mainly when the sky was totally overcast with  $CF = 1$  and the highest clearness index  $k_t$  of 0.9566.

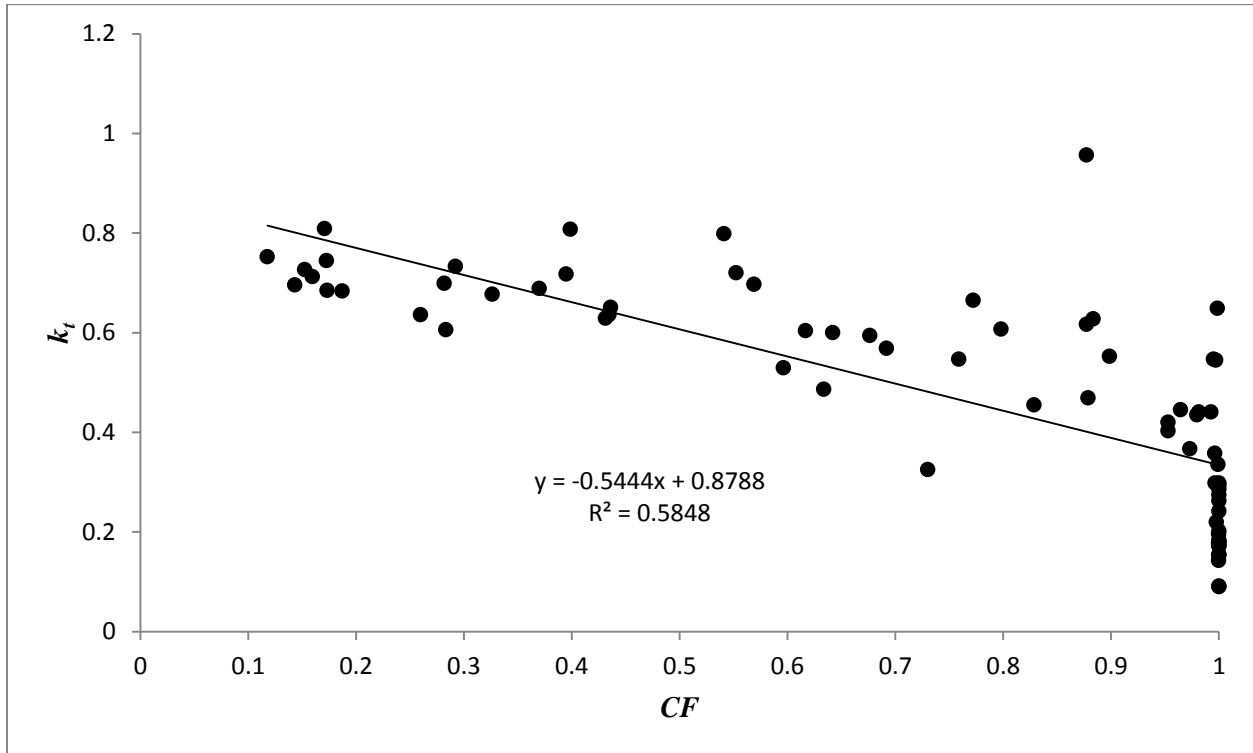


Figure 5.30: Scatter plot of  $k_t$  as a function of the total  $CF$  for the entire dataset.

Linear regression analysis of data was carried out as shown in Fig 5.30 and equation 5.6 was obtained:

$$k_t = 0.8788 - 0.5444 \frac{\bar{c}}{100} \quad (5.6)$$

For the whole data points used, the correlation coefficient for  $k_t$  was found to be  $R = -0.7647$  and the coefficient of determination was found to be  $R^2 = 0.5848$ .

### $k_c$ vs $CF$

Fig 5.31 shows a scatter plot of  $k_c$  as a function of the total  $CF$  for the entire 15 minute dataset. A minimum clearness index  $k_c$  of 0.11868 was also recorded mainly with  $CF = 1$  and the highest recorded clearness index  $k_c$  of 1.2533.

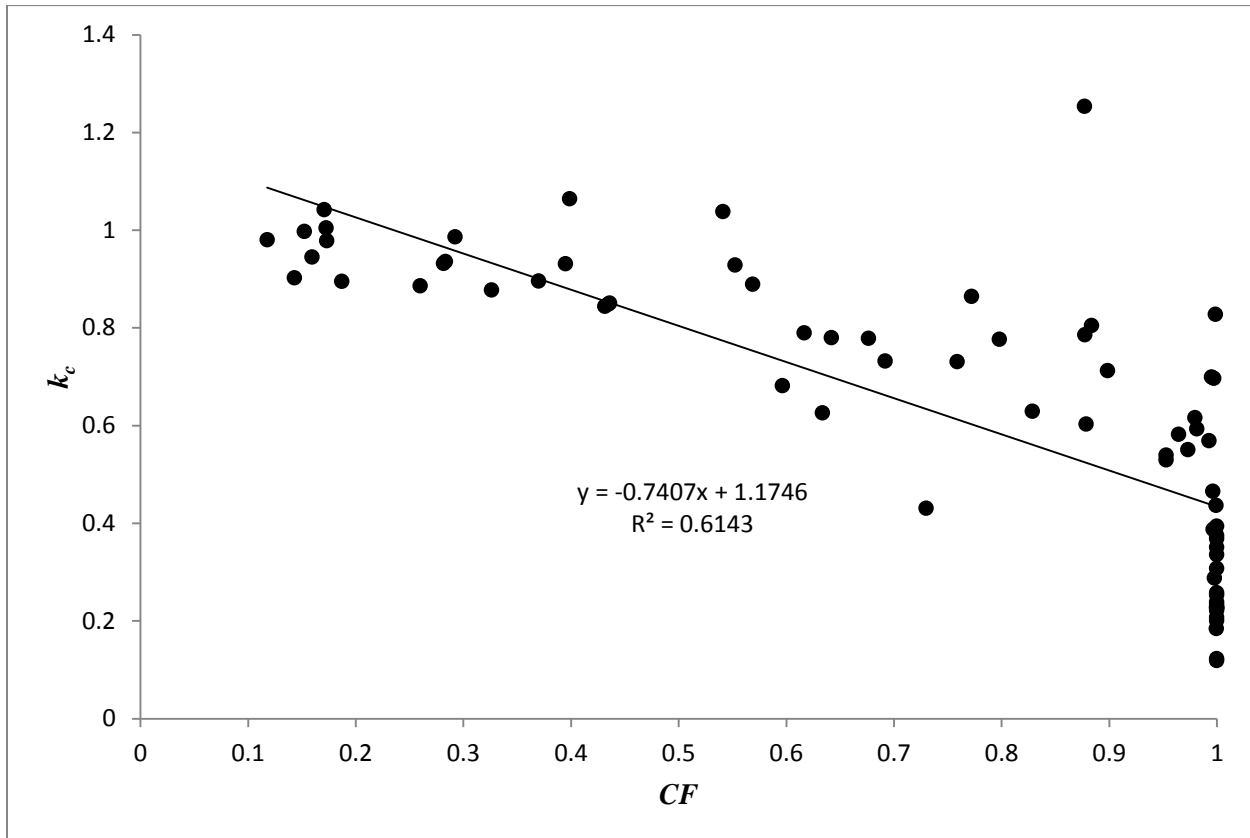


Figure 5.31: Scatter plot of  $k_c$  as a function of the total  $CF$  for the entire dataset.

Linear regression analysis of data was carried out as shown in Fig 5.31 and equation 5.7 was obtained:

$$k_c = 1.1746 - 0.7407 \frac{\bar{c}}{100} \quad (5.7)$$

For the whole data points used, the correlation coefficient for  $k_c$  values was found to be  $R = -0.7838$  and the coefficient of determination was found to be  $R^2 = 0.6143$ .

### $k_b$ vs $CF$

Fig 5.32 shows a scatter plot of  $k_b$  as a function of the total  $CF$  for the entire 15 minute dataset. A minimum clearness index  $k_b$  of 0.000028 was recorded mainly when the sky was totally overcast with  $CF = 1$  and the highest clearness index  $k_b$  of 0.66567.

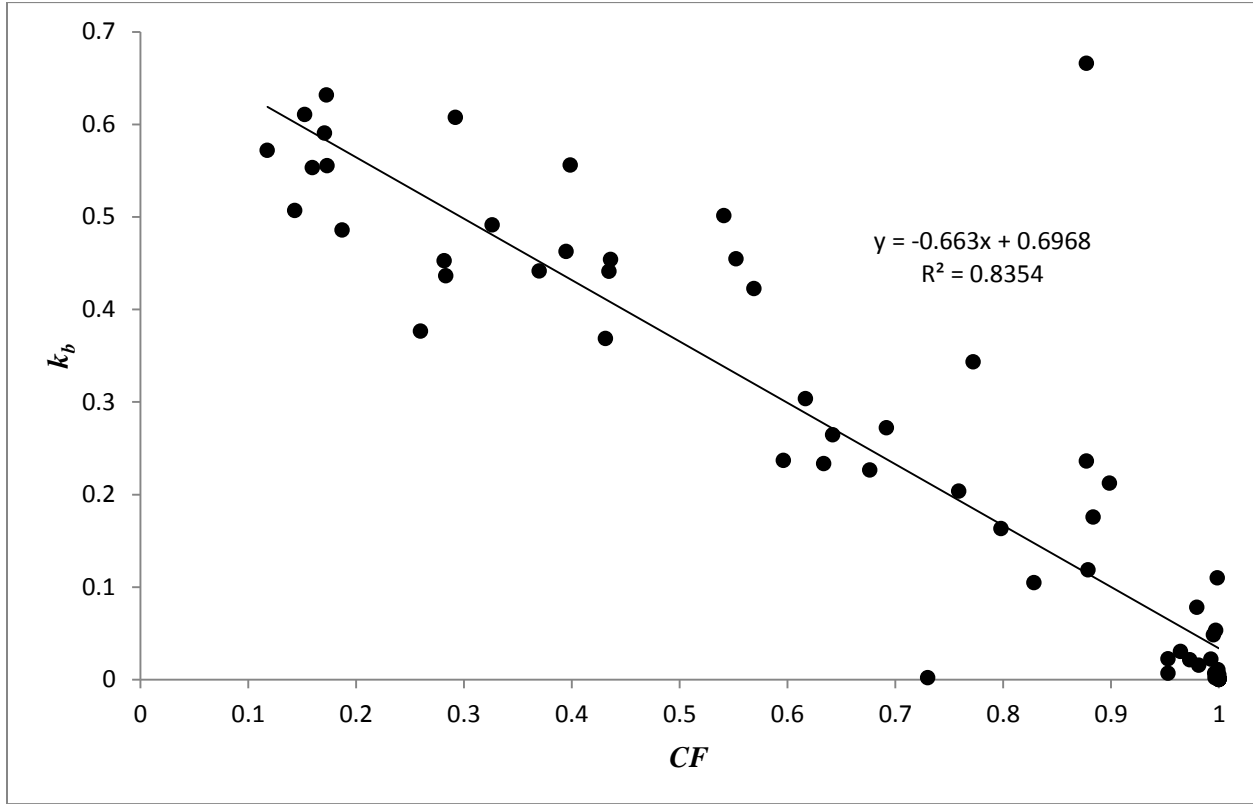


Figure 5.32: Scatter plot of  $k_b$  as a function of the total  $CF$  for the entire dataset.

Linear regression analysis of data was carried out as shown in Fig 5.32 and equation 5.8 was obtained:

$$k_b = 0.6968 - 0.663 \frac{\bar{c}}{100} \quad (5.8)$$

For the whole data points used, the correlation coefficient for  $k_b$  was found to be  $R = -0.9140$  and the coefficient of determination was found to be  $R^2 = 0.8354$ .

### *DNI/DNI<sub>c</sub> vs CF*

Fig 5.33 shows a scatter plot of  $DNI/DNI_c$  as a function of the total  $CF$  for the entire 15 minute dataset. A minimum clearness index  $DNI/DNI_c$  of 0.000043 was also recorded mainly with  $CF = 1.0$  and the highest recorded clearness index  $DNI/DNI_c$  of 1.0278.

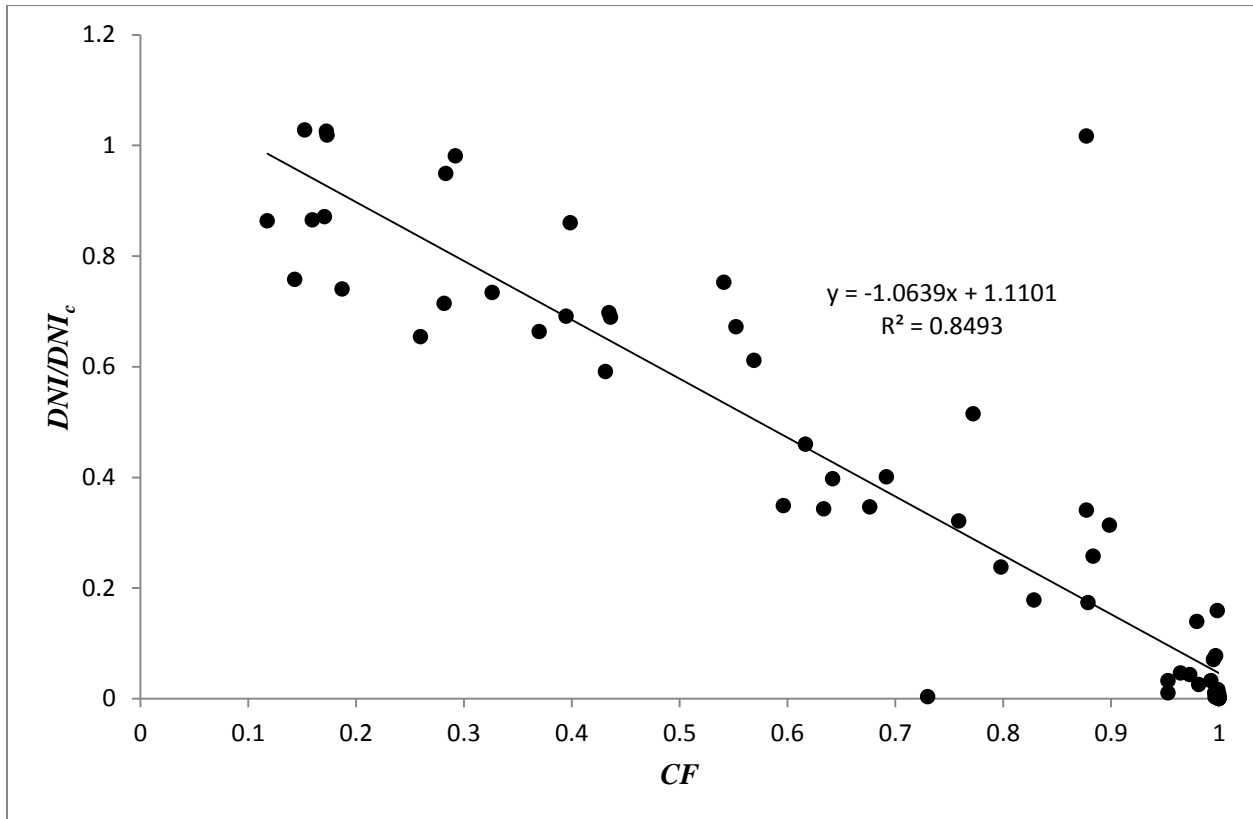


Figure 5.33: Scatter plot of  $DNI/DNI_c$  as a function of the total  $CF$  for the entire dataset.

Linear regression analysis of data was carried out as shown in Fig 5.33 and equation 5.9 was obtained:

$$\frac{DNI}{DNI_c} = 1.1101 - 1.0639 \frac{\bar{c}}{100} \quad (5.9)$$

For the whole data points used, the correlation coefficient for  $DNI/DNI_c$  values was found to be  $R = -0.9216$  and the coefficient of determination was found to be  $R^2 = 0.8493$ .

### *DHI/DHI<sub>c</sub> vs CF*

Fig 5.34 shows a scatter plot of  $DHI/DHI_c$  as a function of the total  $CF$  for the entire 15 minute dataset. A minimum clearness index  $DHI/DHI_c$  of 0.74947 was recorded for a wide range of  $CF$  and the highest  $DHI/DHI_c$  of 6.0094. Statistical analysis of data was carried out and the following equations were obtained:

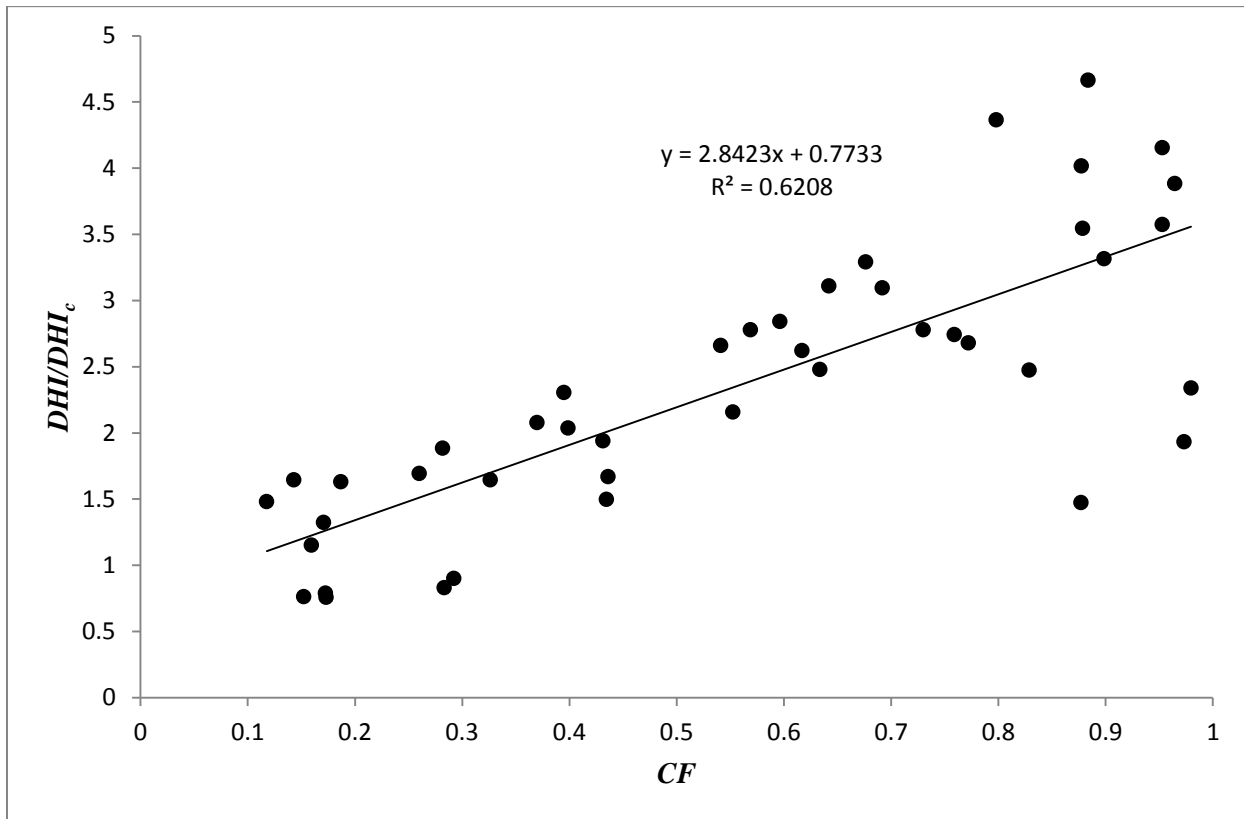


Figure 5.34: Scatter plot of  $DHI/DHI_c$  as a function of the total  $CF$  for the entire dataset.

Linear regression analysis of data was carried out as shown in Fig 5.34 and equation 5.10 was obtained:

$$\frac{DHI}{DHI_c} = 1.2218 + 1.6541 \frac{\bar{c}}{100} \quad (5.10)$$

For the whole data points used, the correlation coefficient for  $DHI/DHI_c$  was found to be  $R = 0.7879$  and the coefficient of determination was found to be  $R^2 = 0.6208$ .

### 5.2.4 Linear regression plots for 4 hours-averaging data.

The total data points that were used for all the clearness indices values of 4 hours averages data are 13. In this data, the lowest  $CF$  of 0.198 was recorded which is about 5 times smaller than the highest  $CF = 1.0$  that was recorded. A linear regression of data was performed between the  $CF$  and a specific clearness index in the next subsections.

#### $k_t$ vs $CF$

Fig 5.35 shows a scatter plot of  $k_t$  as a function of the total  $CF$  for the entire 15 minute dataset. A minimum clearness index  $k_t$  of 0.16631 was recorded mainly when the sky was totally overcast with  $CF = 1.0$  and the highest clearness index of 0.72223.

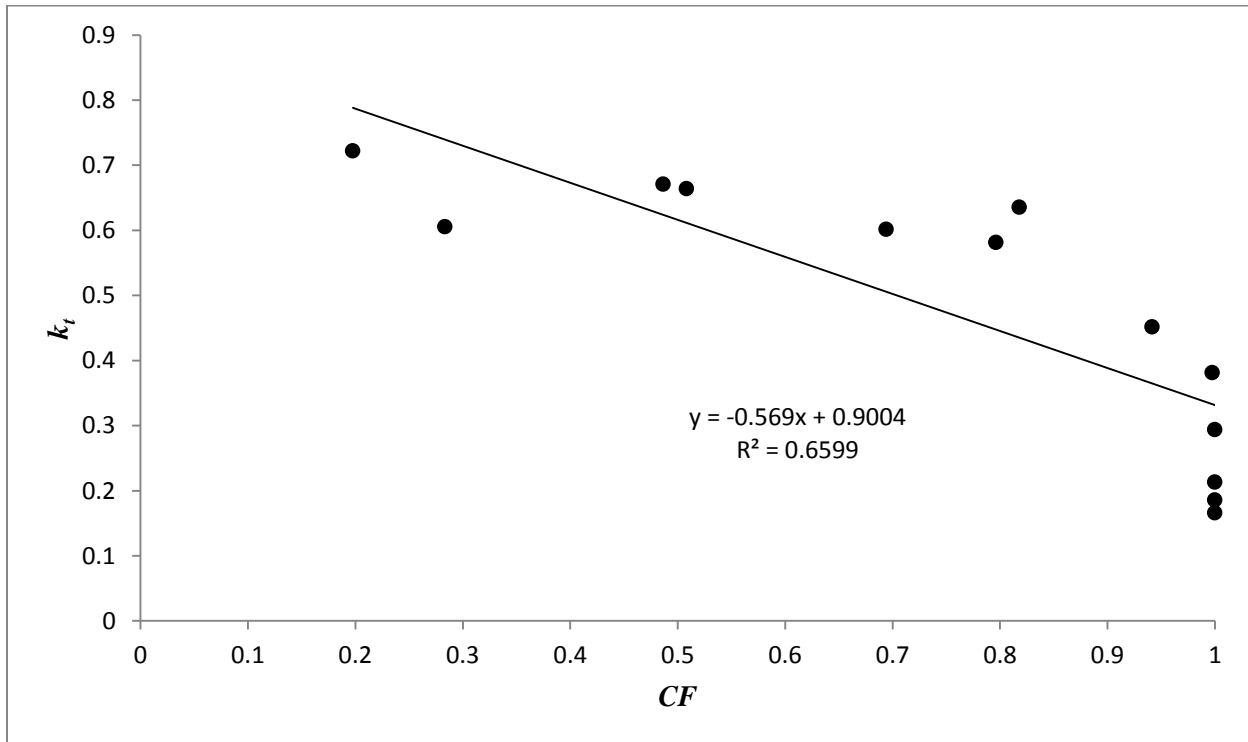


Figure 5.35: Scatter plot of  $k_t$  as a function of the total  $CF$  for the entire dataset.

Linear regression analysis of data was carried out as shown in Fig 5.35 and equation 5.11 was obtained:

$$k_t = 0.9004 - 0.569 \frac{\bar{c}}{100} \quad (5.11)$$

For the whole data points used, the correlation coefficient for  $k_t$  was found to be  $R = -0.8123$  and the coefficient of determination was found to be  $R^2 = 0.6599$ .

### $k_c$ vs $CF$

Fig 5.36 shows a scatter plot of  $k_c$  as a function of the total  $CF$  for the entire 15 minute dataset. A minimum clearness index  $k_c$  of 0.11868 was also recorded mainly with  $CF = 1.0$  and the highest recorded clearness index  $k_c$  of 1.2533.

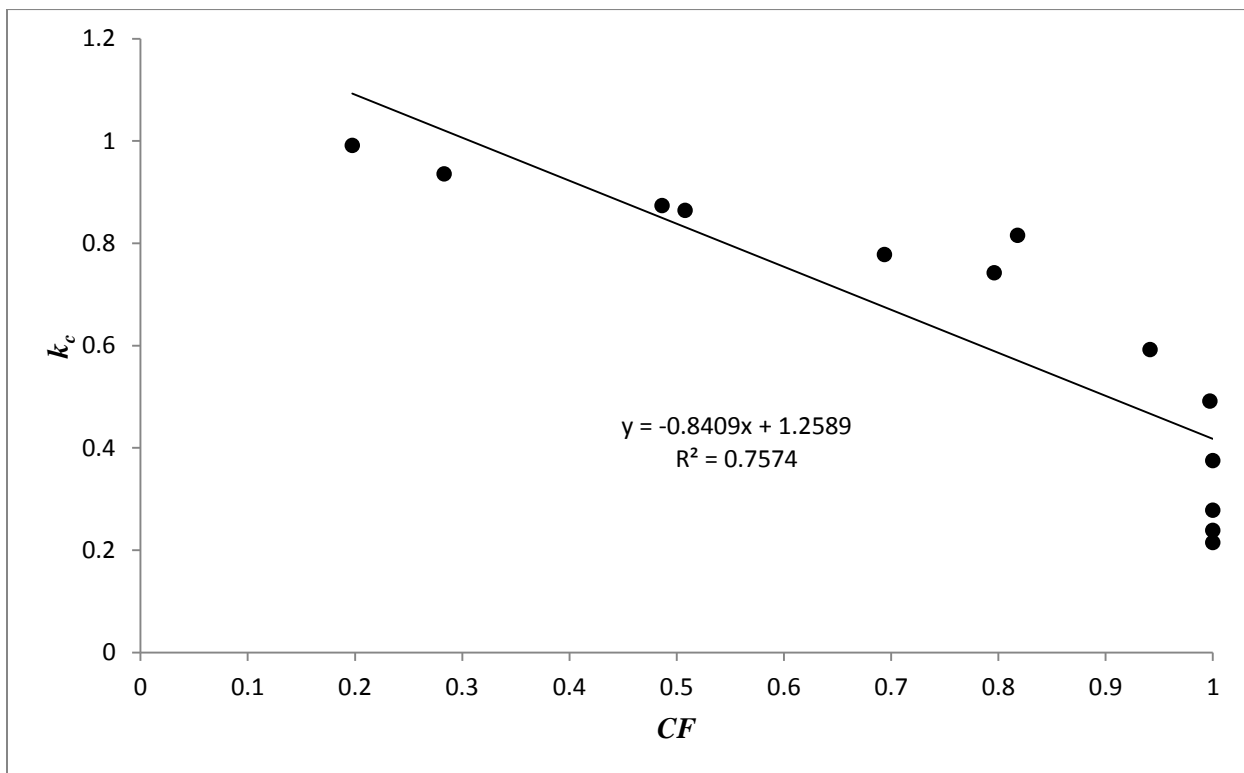


Figure 5.36: Scatter plot of  $k_c$  as a function of the total  $CF$  for the entire dataset.

Linear regression analysis of data was carried out as shown in Fig 5.36 and equation 5.12 was obtained:

$$k_c = 0.9004 - 0.569 \frac{\bar{c}}{100} \quad (5.12)$$

For the whole data points used, the correlation coefficient for  $k_c$  values was found to be  $R = -0.8703$  and the coefficient of determination was found to be  $R^2 = 0.7574$ .

### $k_b$ vs $CF$

Fig 5.37 shows a scatter plot of  $k_b$  as a function of the total  $CF$  for the entire 15 minute dataset. A minimum clearness index  $k_b$  of 0.000366 was recorded mainly when the sky was totally overcast with  $CF = 1.0$  and the highest clearness index  $k_b$  of 0.60111.

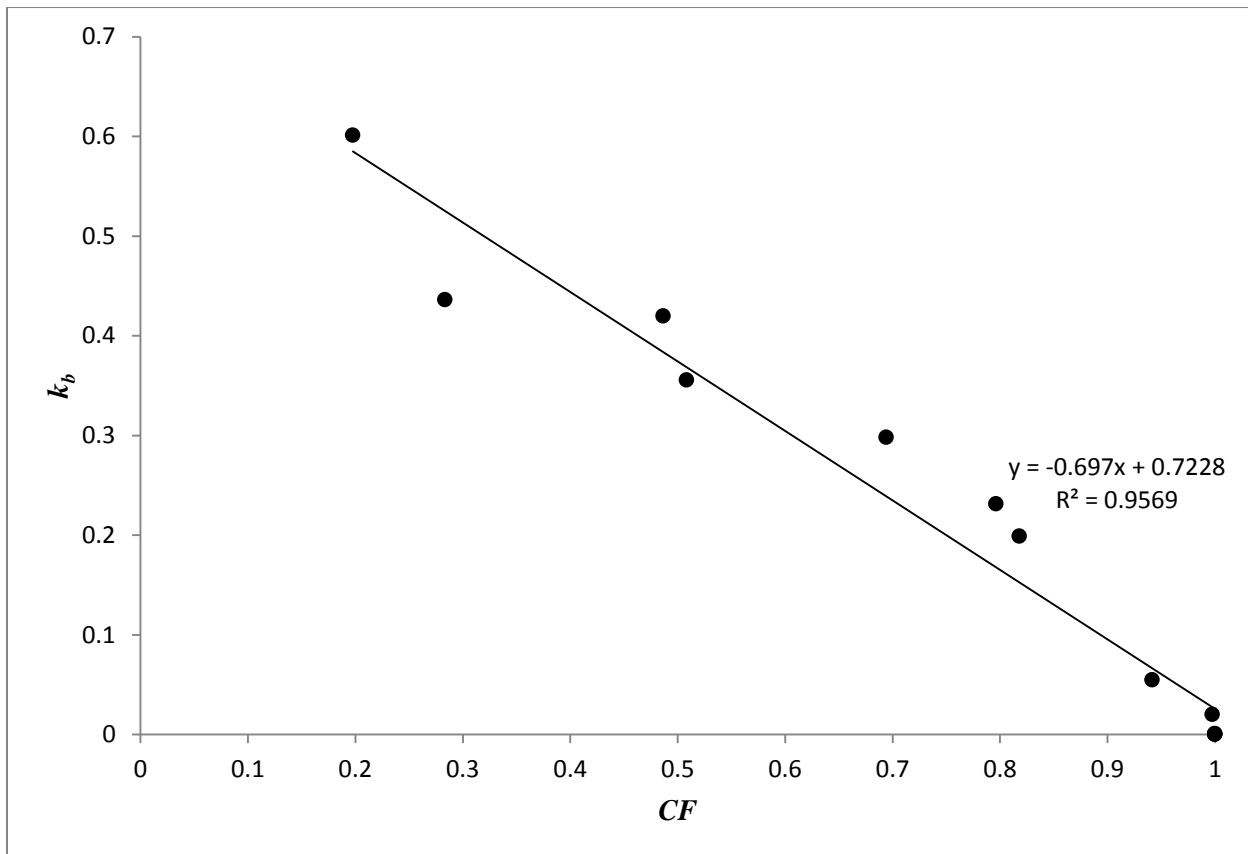


Figure 5.37: Scatter plot of  $k_b$  as a function of the total  $CF$  for the entire dataset.

Linear regression analysis of data was carried out as shown in Fig 5.37 and equation 5.13 was obtained:

$$k_b = 0.7228 - 0.697 \frac{\bar{c}}{100} \quad (5.13)$$

For the whole data points used, the correlation coefficient for  $k_b$  was found to be  $R = -0.9782$  and the coefficient of determination was found to be  $R^2 = 0.9569$ .

### *DNI/DNI<sub>c</sub> vs CF*

Fig 5.38 shows a scatter plot of  $DNI/DNI_c$  as a function of the total  $CF$  for the entire 15 minute dataset. A minimum clearness index  $DNI/DNI_c$  of 0.00054 was also recorded mainly with  $CF = 1.0$  and the highest recorded clearness index  $DNI/DNI_c$  of 1.0132.

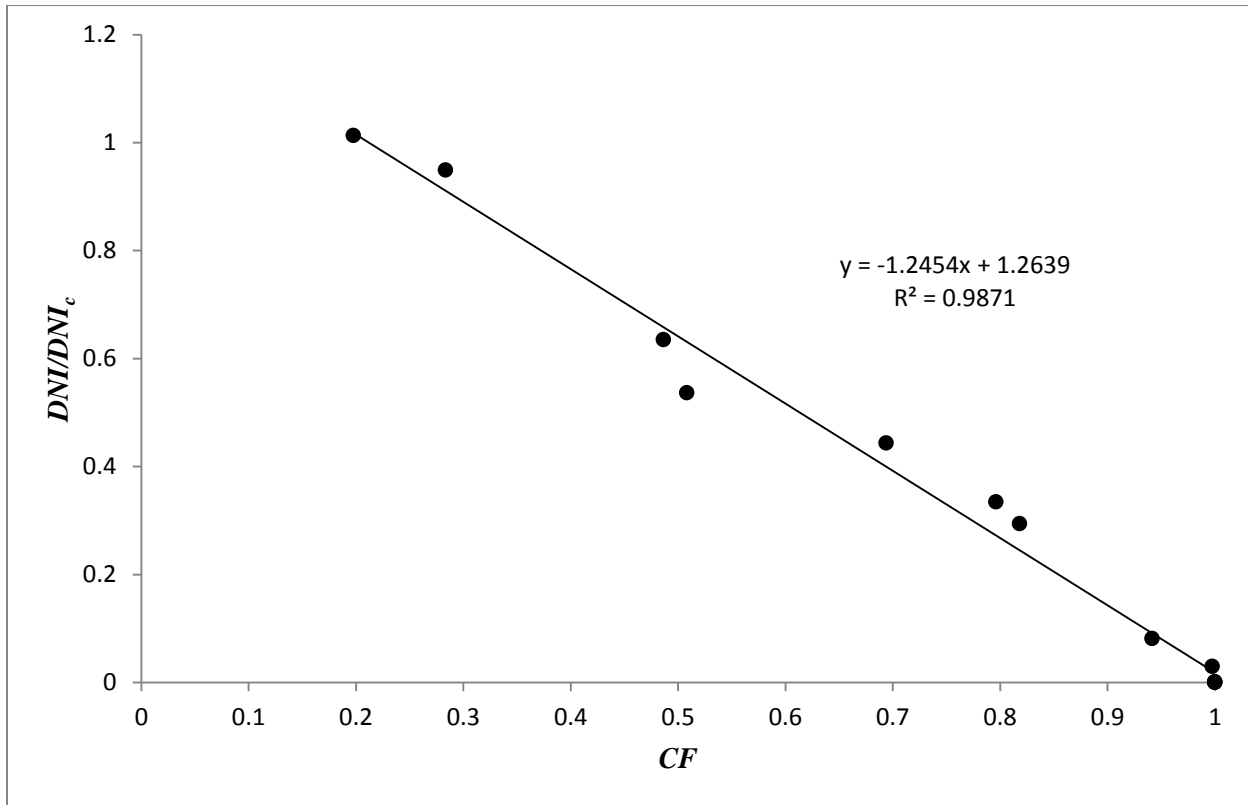


Figure 5.38: Scatter plot of  $DNI/DNI_c$  as a function of the total  $CF$  for the entire dataset.

Linear regression analysis of data was carried out as shown in Fig 5.38 and equation 5.14 was obtained:

$$\frac{DNI}{DNI_c} = 1.2639 - 1.2454 \frac{\bar{c}}{100} \quad (5.14)$$

For the whole data points used, the correlation coefficient for  $DNI/DNI_c$  values was found to be  $R = -0.9935$  and the coefficient of determination was found to be  $R^2 = 0.9871$ .

### ***DHI/DHI<sub>c</sub> vs CF***

Fig 5.39 shows a scatter plot of  $DHI/DHI_c$  as a function of the total  $CF$  for the entire 15 minute dataset. A minimum clearness index  $DHI/DHI_c$  of 0.80271 was recorded for a wide range of  $CF$  and the highest clearness index  $DHI/DHI_c$  of 4.494.

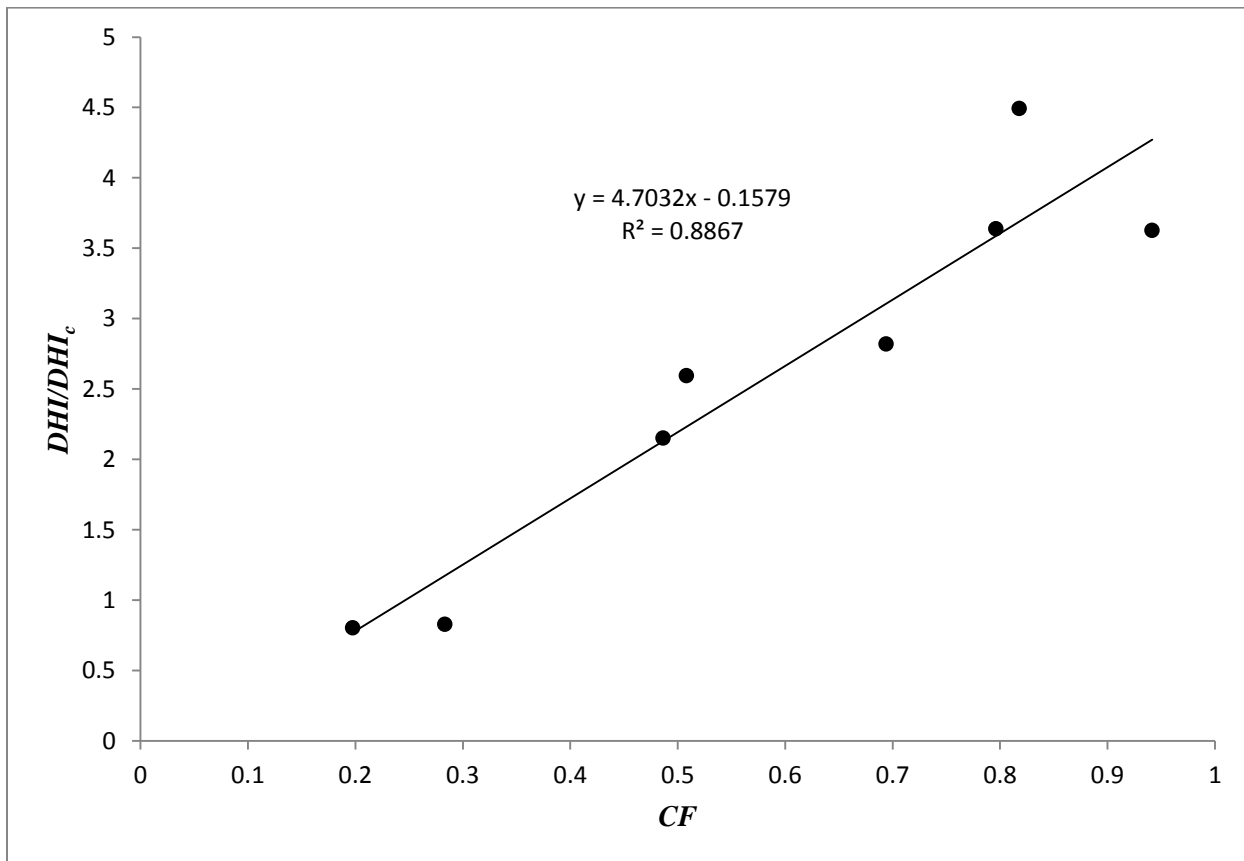


Figure 5.39: Scatter plots of  $DHI/DHI_c$  as a function of the total  $CF$  for the entire dataset.

Statistical analysis of data was carried out and the following equations were obtained:

$$\frac{DHI}{DHI_c} = 0.9756 + 2.1258 \frac{\bar{C}}{100} \quad (5.15)$$

For the whole data points used, the correlation coefficient for  $DHI/DHI_c$  was found to be  $R = 0.9416$  and the coefficient of determination was found to be  $R^2 = 0.8867$ . Also the minimum values of  $CF$  and clearness index-average increase with averaging whilst it is opposite with the maximum clearness index and  $CF$  values. The correlation coefficient for 1 minute data is 0.4774 and 0.5451 for 4 hours average which shows a slight increment. It can be noted that  $R^2$  is generally low for all the entire data averages but it is slightly higher for longer time-averages than for 1 minute data. The overall results found in Durban are in agreement to what Pfister *et al* (2003) found in New Zealand whereby the correlation between  $DHI/DHI_c$  against  $CF$  was very poor.

# Chapter 6

## Discussion of Results

Results presented in chapter 5 are discussed in this chapter. The discussion is done in the subsections following the order in which results were presented in chapter 5. This discussion mainly answers the research question and achieves the aim of this study. Relevant graphs and equations are not reproduced in this chapter but are only referenced.

### 6.1 Radiometric profiles and TSI images to show cloud fraction $CF$

It is expected that with high  $CF$  the beam irradiance,  $DNI$ , will be lowered since there is a higher chance of clouds blocking the sun. However, if there are more clouds in the atmosphere, there will be more scattering of the sun rays leading to high diffuse irradiance,  $DHI$ , being registered on the radiometers. This is evidenced in Fig 5.2 between 11:00 and 13:00 there was an increase in  $CF$  reaching a maximum of 50% and this resulted in  $DNI$  decreasing from just above 850  $W/m^2$  to 650  $W/m^2$  whereas the  $DHI$  increased from just above 50  $W/m^2$  to 100  $W/m^2$ . Between 11:00 and 13:00  $GHI$  decreased from 600  $W/m^2$  to 550  $W/m^2$ . An increase in  $CF$  caused an increase in  $DHI$  between 11:00 and 13:00 but it did not cause an increase in  $DHI$  after 15:00. There is no consistency in the way the change in  $CF$  affects the diffuse irradiance.

Fig 5.5 shows an overcast day and it was noted that the small fluctuations indicated on the graph did not affect the received  $DNI$ . However, there was a noticeable spike at 13:05 even though the  $CF$  was 100% at this time. If the cloud obstructing the sun has a gap in-between, this results in an increase in  $DNI$  received by the radiometer regardless of the  $CF$  being 100%. Fig 5.6b shows a glow in the sunspot area which is a sign of gaps in the cloud obstructing the sun. Between the time 09:30 and 16:00 when the sky was constantly overcast the diffuse irradiance was always fluctuating in the range of 100  $W/m^2$  to 300  $W/m^2$  thus exhibiting the fact that even though the

*CF* may be constantly overcast at 100% the cloud thickness content does not remain the same hence different scattering magnitudes. Different scattering magnitudes will result in different diffuse irradiances resulting in fluctuations. This shows that for the same *CF* we may have different cloud content (cloud optical thickness) leading to different responses on the beam/diffuse irradiance graph thus there is no simple relationship between the *CF* alone (without other cloud properties) and the radiometry measurements.

Fig 5.9 shows that fluctuations in *CF* between 8:15 and 8:30 resulted in fluctuations in the radiometric readings. *GHI*, *DHI* and *DNI* increased with decreasing *CF* between 8:15 and 08:30. Fluctuations in *GHI*, *DNI* and *DHI* between 09:15 and 09:45 could not be conclusively be explained by the change in *CF* since there was little variation in *CF* during this time. A decrease in *CF* between 09:45 and 10:00 resulted in an increase in *GHI*, *DNI* and *DHI*. An image in Fig 5.10 shows that the sun was in the vicinity of clouds, but it was not obstructed by them, hence a higher reading of *GHI*, *DNI* and *DHI*.

According to Fig 5.11, the decrease in *CF* just after 11:00 resulted in an increase in *GHI* and *DNI* but a decrease in *DHI*. *DHI* received by the radiometer was decreased since there was less scattering of radiation taking place due to less amount of clouds which plays a big role in radiation scattering. The increase in *CF* between 11:15 and 11:30 does not concurrently result in a decrease in *DNI* but takes time to affect the *DNI*. A high *CF* of 80% at 12:30 did not result in low beam irradiance but instead a higher beam irradiance of  $DNI = 950 \text{ W/m}^2$  was received by the radiometer. A *CF* of 71% at 11:46 resulted in a very low beam irradiance of  $DNI \sim 0 \text{ W/m}^2$  because the sun was obstructed by the clouds as shown in Fig 5.12.

According to Fig 5.16, a passing cloud with gaps in-between resulted in a sudden increase in the *DNI* as noticed between 10:15 and 10:30. A series of TSI images shown in Fig 5.16 confirms the drifting of the clouds from south east direction. A higher *CF* at 12:30 resulted in a decrease in beam irradiance to  $DNI = 0 \text{ W/m}^2$  whereas the *GHI* and *DHI* did not decrease to  $0 \text{ W/m}^2$  since there is always scattering of radiation even if the *CF* is 100%. However an increase in *CF* towards 11:30 resulted in an increase in *DNI* due to the fact that the sun was not obstructed.

## 6.2 Centred moving average $DNI$ and $I - CF$ vs $t$ for different time-averaging time-scales $\tau$ 10 September 2014

Fig 5.18a shows more responsiveness of the  $DNI$  and  $I - CF$  graphs of 1 minute data with respect to time. A graph of  $DNI$  vs time follows the pattern of the graph of  $I - CF$  vs time graph; however the  $DNI$  vs time graph is lagging behind. Nevertheless, when  $I - CF$  is less than 0.2, the pattern is not simply related as noticed between 11:48 and 12:00 whereby there is a sharp increase in  $DNI$  which resulted from a small change in  $I - CF$ . Also, there were fluctuations in  $DNI$  between 12:00 and 13:36 which could not be attributed to the change in  $CF$ . Fig 5.18b of 15 minutes averaging graphs shows smoothed graphs in which the  $DNI$  vs time graph does not lag much behind the  $I - CF$  vs time graph. Fluctuations in  $DNI$  graph after 12:00 have been smoothed to reduce their responsiveness. Fig 5.18c with 30 minutes averaging graphs show more smoothed graphs of both  $DNI$  vs time and  $I - CF$  vs time, but however the graph of  $DNI$  vs time is still lagging behind more than with 15 minutes averaging. Fig 5.18d show 1 hour averaging graphs of  $DNI$  vs time and  $I - CF$  vs time which are more smoothed than those of 30 minutes averaging but nevertheless the  $DNI$  vs time graph still lags behind the  $I - CF$  vs time graph. Increasing time averaging improves smoothening of the graphs; however the responsiveness of the graphs is reduced.

## 6.3 Centred moving average $DHI$ and $CF$ vs $t$ for different time-averaging time-scales $\tau$ 10 September 2014

Fig 5.19a shows more responsiveness of the  $DHI$  and  $CF$  graphs of 1 minute data with respect to time. The graph of  $DHI$  vs time follows the pattern as that of graph  $CF$  vs time between 10:00 and 11:40 whereby the  $CF$  was varying and not constantly at  $CF = 1$ . Between 12:00 and 13:40, there was a variation in  $DHI$  even though the  $CF$  was constant. In Fig 5.19b shows smoothed 15-minute average graphs of  $DHI$  and  $CF$  vs time, in which it is evident that  $DHI$  follows  $CF$  except where  $CF$  is not at its maximum value of 1. Fig 5.19c shows 30 minutes average graphs of  $DHI$  vs time and  $CF$  vs time which are smoothed and it is evident in this graph that  $DHI$  vs time graph follows the  $CF$  vs time graph if  $CF$  is not at maximum  $CF = 1$  but responsiveness is reduced. Fig 5.19c show 1 hour average graphs of  $DHI$  vs time and  $CF$  vs time which are more smoothed and

*DHI* vs time graph follows the *CF* vs time graph if *CF* is not at maximum  $CF = 1$  but responsiveness is more reduced.

#### **6.4 Linear regression plots for 1 minute data.**

If the clouds cause little or insignificant decrease on the *DNI* component, with increased scattering this increases the received radiation and this is termed enhancements. This phenomenon is normally evidenced for shorter timescales of 1 minute averaged data and the data used for this work is that of 1 minute averaged data for both the radiometers and the TSI. Enhancements were strongly noticed in the graph of  $GHI/GHI_o$  and  $GHI/GHI_c$  against *CF* and weakly in  $DNI/DNI_c$  against *CF*. All scatter plots obtained for 1 minute data did not exhibit a linear relationship between the variables.

#### **6.5 Linear regression plots for 15 minutes, 1 hour and 4 hours average data.**

A discussion of linear regression plots for all averaged data is combined in this section. A straight line of best fit was included for each and every plot to determine if there is a linear relationship between the clearness indices and *CF*. Coefficients of determination,  $R^2$  for each scatter plot are tabulated in Table 6.1. Scatter plots with  $R^2 \geq 0.8$  are written in bold and are regarded as linearly correlated because of their strong coefficient of determination. However, for *DHI*-related scatter plots,  $CF > 98\%$  were not included in the linear regression analysis since it was noted in the moving average graphs that when *CF* is maximised, *DHI* varies much.

According to Table 6.1  $k_t$ ,  $k_c$ ,  $k_b$  and  $DNI/DNI_c$  are negatively correlated to *CF*, whereas  $DHI/DHI_c$  was positively correlated to *CF*. The coefficient of determination for  $k_t$  and  $k_c$  improved with an increase in time-averaging having a maximum of  $R^2 = 0.6599$  and  $R^2 = 0.7574$  for  $k_t$  and  $k_c$  respectively at 4 hour average. Since both  $R^2$  are less than 0.8 it implies that there is no strong linear relationship existing between both  $k_t$  and  $k_c$  with *CF*. All coefficients of determination for both  $k_b$  and  $DNI/DNI_c$  were greater than 0.8 for all time averages and they all strengthened with an increase in time averages. Maximum  $R^2$  at 4 hours average were  $R^2 = 0.9569$  and  $R^2 = 0.9871$  for  $k_b$  and  $DNI/DNI_c$  respectively. Since all  $R^2$  for  $k_t$  and  $DNI/DNI_c$  were greater than 0.8 it implies that a strong linear relationship exists between both  $k_b$  and  $DNI/DNI_c$ . It can be noted that clear sky-related clearness indices had a strong correlation with *CF* as

compared to the extraterrestrial-related clearness indices as stated by Khan *et al* (2012) (Khan & Ahmad, 2012). Coefficient of determination improved by averaging for  $DHI/DHI_c$  having a maximum of  $R^2 = 0.8867$  for 4 hours average. This implies that a strong linear relationship exists for 4 hours average. However, this is only true if we consider  $CF$  that is less than 98%.

Table 6.1: Correlation coefficient and coefficient of determination for clearness indices against  $CF$

Scatter plot	Time average	$R$	$R^2$
$k_t$ vs $CF$	15 minutes average	- 0.7616	0.5801
	1 hour average	- 0.7647	0.5848
	4 hours average	- 0.8123	0.6599
$k_c$ vs $CF$	15 minutes average	- 0.7808	0.6097
	1 hour average	- 0.7838	0.6143
	4 hours average	- 0.8702	0.7574
$k_b$ vs $CF$	15 minutes average	- 0.9228	<b>0.8516</b>
	1 hour average	- 0.9140	<b>0.8354</b>
	4 hours average	- 0.9782	<b>0.9569</b>
$DNI/DNI_c$ vs $CF$	15 minutes average	- 0.9293	<b>0.8636</b>
	1 hour average	- 0.9216	<b>0.8493</b>
	4 hours average	- 0.9935	<b>0.9871</b>
$DHI/DHI_c$ vs $CF$	15 minutes average	0.7947	0.6316
	1 hour average	0.7879	0.6208
	4 hours average	0.9416	<b>0.8867</b>

# Chapter 7

## Conclusion and recommendations

### 7.1 Conclusion

An increase in  $CF$  resulted in a decrease in  $DNI$  since there were more chances of the sun being obstructed by the clouds except for the rare moments when the clouds did not obstruct the sun. Between 12:30 and 12:45 a higher  $CF$  resulted in a bigger  $DNI$  as shown in Fig 5.11 and this can only be explained using information from the TSI images which shows if the sun is obstructed by the clouds or not. The general trend was found that  $DNI$  increased as  $I - CF$  increases, according to the moving average graphs in Fig 5.18. An increase in  $CF$  resulted in an increase in  $DHI$  since more clouds contribute to more scattering of radiation. However, this is only true if the  $CF$  is not overcast. For an overcast sky, there is no simple relationship between the  $CF$  and  $DHI$  since  $DHI$  varies a lot for the same  $CF = 100\%$  as evidenced in Fig 5.5 and Fig 5.19.

Little variation in  $CF$  may cause higher variations in radiometric readings, especially when the clouds in the vicinity of the sun have gaps in-between. Gaps in the clouds cause enhancements in solar radiation because they allow sun rays to pass through and at the same time they also scatter radiation increasing diffuse irradiance and this overall result in a higher global irradiance which is greater than the extraterrestrial or clear sky irradiance. This was evidenced in Fig 5.16 between 10:15 and 10:30. This phenomenon is also reflected in the scatter plots whereby the clearness indices were greater than 1.0. It was also noted that the change in  $CF$  may take some time before it affects the radiometric readings as shown in Fig 5.11 between 11:15 and 11:30 and this may be due to a slowly drifting cloud that passes the TSI and takes some time to reach the radiometers since they are almost 10 m apart. A low beam of  $DNI \sim 0 \text{ W/m}^2$  was not obtained for a  $CF = 100\%$  only, but also for low  $CF$  of 71% as shown in Fig 5.11 at 11:46.

There was no linear relationship observed for all 1 minute data scatter plots. There is a negative correlation for all clearness indices except for  $DHI/DHI_c$ . There were weak linear relationships between  $k_t$  and  $k_c$  with  $CF$ , but however  $R^2$  increased with averaging. A strong linear relationship exists between  $k_b$  and  $DNI/DNI_c$  and  $R^2$  increased with averaging. A strong linear relationship exists for  $DHI/DHI_c$  with  $CF$  at 4 hours average only when  $CF$  less than 98% is considered. A conclusion can be drawn that a strong linear relationship is established when averages for long time-frame are considered. However, there is no simple relationship between  $CF$  and radiometric readings for short time-frames of the order of minutes since more information on cloud intrinsic properties such as optical thickness are required to explain why we get different radiometric readings for the same  $CF$ .

## **7.2 Considerations for future work**

For future work we recommend designing better cloud detection algorithms that give more information on the clouds like their optical thickness and establishing whether these clouds have gaps within them. This will help in getting more relevant and helpful output results that helps in estimating the effects of the  $CF$  on radiometric measurements.

# Bibliography

- (n.d.). Retrieved April 24, 2015, from [http://www.jma.go.jp/jma/jma-eng/jma-center/ric/material/1\\_Lecture\\_Notes/CP7-Sunshine.pdf](http://www.jma.go.jp/jma/jma-eng/jma-center/ric/material/1_Lecture_Notes/CP7-Sunshine.pdf)
- (n.d.). Retrieved August 01, 2016, from <http://www.omniinstruments.co.uk/smp3-smart-pyranometer.html>
- (n.d.). Retrieved August 01, 2016, from [http://www.jma.go.jp/jma/jma-eng/jma-center/ric/material/1\\_Lecture\\_Notes/CP7-Sunshine.pdf](http://www.jma.go.jp/jma/jma-eng/jma-center/ric/material/1_Lecture_Notes/CP7-Sunshine.pdf)
- (n.d.). Retrieved August 01, 2016, from <http://www.calpoly.edu/~gthorncr/ME450/documents/Handout7.MeasuringSolarRadiationandSolarData.pdf>
- Cebecauer, T., Skoczek, A., Betak, J., & Suri, M. (2011). *Site Assessment of Solar Resource*. Bratislava: GeoModel Solar.
- Stoffel, T., Renné, D., Myers, D., Wilcox, S., Sengupta, M., George, R., et al. (2010). *Concentrating solar power*. Springfield: National Renewable Energy Laboratory.
- Urquhart, B., Ghonima, M., Nguyen, D., Kurtz, B., Chow, C. W., & Kleissl, J. (2013). Sky imaging systems for short-term forecasting. In J. Kleissl (Ed.), *Solar Energy Forecasting and Resource Assessment* (pp. 195 - 232). Academic Press.
- Angstrom, A. S. (1924). Solar terrestrial radiation. *Meteorological Society*, 50, 121-126.
- Ashdown, I. (n.d.). *Helios32*. Retrieved September 01, 2014, from [www.helios32.com/Measuring%20Light.pdf](http://www.helios32.com/Measuring%20Light.pdf).
- Augustine, C., & Nnabuchi, M. N. (2009a). Empirical models for the correlation of global solar radiation with meteorological data for Enugu, Nigeria. *The Pacific Journal of Science and Technology*, 10(1), 693-700.

- Augustine, C., & Nnabuchi, M. N. (2009b). Correlation of cloudiness index with clearness index for four selected cities in Nigeria. *The Pacific Journal of Science and Technology*, 10(2), 568-573.
- Babatunde, E. B., & Aro, T. O. (1990). Characteristics variation of total solar radiation at Ilorin, Nigeria. *Nigerian Journal of Solar Energy*, 9, 157-173.
- Bennet, I. (1969). Correlation of daily insolation with daily total cloud cover and percentage of possible sunshine. *Solar Energy*, 12(3), 391-393.
- Boland, J., Huang, J., & Ridley, B. (2013). Decomposing global solar radiation into its direct and diffuse components. *Renewable and Sustainable Energy Reviews*(28), 749-756.
- Buch, K. A., Jr, Sun, C. -H., & Thorne, L. R. (1995). Cloud classification using whole-sky imager data. *symposium on meteorological observations and instrumentation*, (pp. 35-39). Livermore.
- Calbo, J., & Sabburg, J. (2008). Feature extraction from whole-sky ground-based images for cloud-type recognition. *Atmospheric and Oceanic Technology*, 25, 3-14.
- Calbo, J., Pages, D., & Gonzalez, J. A. (2005). Empirical studies of cloud effectson UV radiation : A review. *Geophysics*, 43(2), 1-28.
- Calbo, J., Sabburg, J., Badosa, J., & Gonzalez, J. A. (2008). Cloud effects on uv radiation at two opposing hemispheric sites. *ICCP*, 7-11.
- Carrol, J. J. (1984). Global transmissivity and diffuse fraction of solar radiation for clear and cloudy skies as measured and as predicted by bulk transmissivity models. *Solar Energy*, 35(2), 105-118.
- Carzola, A., Olmo, F. J., & Alados-Arboledas, L. (2008a). Development of a sky imager for cloud cover assessment. *Journal of the Optical Society of America.*, 25(1), 29 - 39.

- Chow, C. W., Urquhart, B., Lave, M., Dominguez, A., Kleissl, J., Shields, J., et al. (2011). Intra-hour forecasting with a total sky imager at the UC San Diego solar energy testbed. *Solar Energy*, 85, 2881–2893.
- Curry, J. A., Rossow, W. B., Randall, D., & Schramm, J. L. (1996). Overview of arctic cloud and radiation characteristics. *Climate*, 9, 1731-1764.
- Duffie, J. A., & Beckman, W. A. (2013). *Solar engineering of thermal processes* (4th ed.). New York: John Wiley and Sons.
- Dye, D. (2012). Looking skyward to study ecosystem carbon dynamics. *Transactions of the American Geophysical Union*, 93(14), 141 - 143.
- Edkins, M., Winkler, H., & Marquard, A. (2009, September). *Large-scale rollout of concentrating solar power*. Retrieved August 19, 2014, from <http://www.erc.uct.ac.za>
- Erlick , C., & Frederick, J. E. (1998). Effects of aerosols on the wavelength dependence of atmospheric transmission in the ultraviolet and visible: 2. Continental and urban aerosols in clear skies. *Geophysics*, 103(18), 23,275-23,285.
- Estupiñán, J. G., Raman, S., Crescenti, G. H., Streicher, J. J., & Barnard, W. F. (1996). Effects of clouds and haze on UV-B radiation. *Geophysics*, 101, 16807-16816.
- Falayi, E. O., & Rabiou, A. B. (2012). Solar radiation models and information for renewable energy applications. In *Solar Radiation* (pp. 111-130). Akure: InTech.
- Falayi, E. O., Adepitan, J. O., & Rabiou, A. B. (2008). Empirical models for the correlation of global solar radiation with meteorological data for Iseyin, Nigeria. *The Pacific Journal of Science and Technology*, 9(2), 583-591.
- Fluri, T. P. (2009). The potential of concentrating solar power in South Africa. *Energy Policy*, 37, 5075-5080.
- Garg, H. P., & Garg, S. N. (1993). Measurement of solar radiation-1.Radiation instruments. *Renewable Energy*, 3(4/5), 321-333.

- Govender, P. (2013). *Construction and analysis of the receiver for a solar thermal cooker system (Master's thesis)*. Master's Thesis, University of KwaZulu Nata, Physics, Durban.
- Gueymard, C. A., & Myers, D. R. (2008). Solar Radiation Measurement: Progress in Radiometry for Improved Modeling. In V. Badescu (Ed.), *Modeling Solar Radiation at the Earth Surface* (pp. 1-27). Heidelberg: Springer.
- Gueymard, C. A., & Thevenard, D. (2009). Monthly average clear-sky broadband irradiance database for worldwide solar heat gain and building cooling load calculations. *Solar Energy*, 83, 1998–2018.
- Harrouni, S. (2008). Fractal classification of typical meteorological days from global solar Irradiance: Application to five sites of different climates. In *Modeling Solar Radiation at the Earth Surface* (pp. 29-54). Heidelberg: Springer.
- Hill, R. (1924). A lens for whole sky photographs. *Quarterly Journal of the Royal Meteorological Society*, 50(211), 227 - 235.
- <http://www.scratchapixel.com/lessons/3d-advanced-lessons/volume-rendering/volume-rendering-for-artists/>. (n.d.). Retrieved October 28, 2014
- Huo, J., & Lu, D. (2009). Cloud determination of all-sky images under low-visibility conditions. *Atmospheric and Oceanic Technology*, 26, 2172-2181.
- Huo, J., & Lu, D. (2012). Comparison of cloud cover from all-sky imager and meteorological observer. *Atmospheric and Oceanic Technology*, 29, 1093-1101.
- Iqbal, M. (1983). *An introduction to solar radiation*. New York: Academy Press.
- Janjai, S., & Tosing, K. (2000). A new model for calculating global radiation from cloud cover data for Thailand. *Proceedings of the first regional conference on energy technology towards a clean environment*. Chiang Mai.

- Josefsson, W., & Landelius, T. (2000). Effect of clouds on UV irradiance: As estimated from cloud amount, cloud type, precipitation, global radiation and sunshine duration. *Geophysics*, *105*, 4927-4935.
- Kalisch, J., & Macke, A. (2008). Estimation of the total cloud cover with high temporal resolution and parametrization of short-term fluctuations of sea surface insolation. *Meteorological*, *17*, 603 - 611.
- Kalogirou, S. A. (2004). Solar thermal collectors and applications. *Progress in Energy and Combustion Science*, *30*(3), 231-295.
- Khan, M. M., & Ahmad, J. M. (2012). Estimation of global solar radiation using clear sky radiation in Yemen. *Engineering Science and Technology Review*, *5*(2), 12-19.
- Krotkov, N. A., Bhartia, P. K., Herman, J. R., Fioletov, V., & Kerr, J. (1998). Satellite estimation of spectral surface UV irradiance in the presence of tropospheric aerosols: 1. Cloud-free case. *Geophysics*, *103*(8), 8779-8793.
- Lanini, F. (2010). *Division of global radiation into direct radiation and diffuse radiation*.
- Li, Q., Lu, W., & Yang, J. (2011). A hybrid thresholding algorithm for cloud detection on ground-based color images. *Atmospheric Ocean Technology*, *28*, 1286–1296.
- Liu, B. Y., & Jordan, R. C. (1960). The interrelationship and characteristic distribution of direct, diffuse and total solar radiation. *Solar Energy*, *4*, 1-19.
- Long, C. N. (2010). Correcting for circumsolar and near-horizon errors in sky cover retrievals from sky images. *Open Atmospheric Science*, *4*, 45-52.
- Long, C. N., & Ackerman, T. P. (2000). Identification of clear skies from broadband pyranometer measurements and calculation of downwelling shortwave cloud effects. *Geophysics*, *105*, 15 609-15 626.

- Long, C. N., & DeLuisi, J. J. (1998). Development of an automated hemispheric sky imager for cloud fraction retrievals. *10th Symp. on Meteorological Observations and Instrumentation*, (pp. 171-174). Phoenix.
- Long, C. N., Sabburg, J. M., Calbo, J., & Pages, D. (2006). Retrieving cloud characteristics from ground-based daytime color all-sky images. *Atmospheric and Oceanic Technology*, *23*, 633-652.
- Long, C. N., Sabburg, J. M., Calbo, J., & Pages, D. (2006). Retrieving cloud characteristics from ground-based daytime color all-sky images. *Atmospheric and oceanic technology*, *23*, 633-652.
- Long, C. N., Slater, D. W., & Tooman, T. (2001). *Total sky imager model 880 status and testing results*. ARM.
- Lu, D., Huo, J., & Lu, Y. (2001). The scientific technologic problems and primitive test of ground-based all-sky imager remote sensing. In *Chinese Remote Sensing-20 year* (pp. 114-120). China Meteorological Press.
- Marquez, R., Gueorgulev, V. G., & Coimbra, C. F. (2011). Forecasting of global horizontal irradiance using sky cover indices. *ASME International Conference on Energy Sustainability*. Washington DC.
- Mateos, D., Bilbao, J., de Miguel, A., & Pérez-Burgos, A. (2010). Dependence of ultraviolet (erythemal and total) radiation and CMF values on total and low cloud covers in Central Spain. *Atmospheric Research*, *98*, 21-27.
- McKenzie, R. L., Johnston, P. V., Smile, D., Bodhaine, B. A., & Madronich, S. (2001). Altitudes effects on UV spectral radiance deduced from measurements at Lauder, New Zealand, and Mauna Loa Observatory, Hawaii. *Geophysics*, *106*, 22,845-22,860.
- Messenger, R. A., & Ventre, J. (2010). *Photovoltaic systems engineering*. Boca Raton: CRC Press.
- Morris, V. (2005). *Total sky imager handbook*. ARM.

- Neto, S. L., von Wangenheim, A., Pereira, E. B., & Comunello, E. (2010). The use of euclidean geometric distance on RGB color space for the classification of sky and cloud patterns. *Atmospheric Ocean Technology*, 27, 1504–1517.
- Newport. (2016, April 08). Retrieved from <https://www.newport.com/t/introduction-to-solar-radiation>
- Nimnuan, P., & Janjai, S. (2012). An approach for estimating average daily global solar radiation from cloud cover in Thailand. *Procedia Engineering*, 32, 399 – 406.
- Norris, D. J. (1968). Correlation of solar radiation with clouds. *Solar Energy*, 12(1), 107-112.
- Orgill, J. F., & Hollands, K. G. (1977). Correlation equation for hourly diffuse radiation on a horizontal surface. *Solar Energy*(19), 357.
- Page, J. K. (1964). The estimation of monthly mean values of daily total short-wave radiation on vertical and inclined surfaces from sunshine records for latitude 40 degrees N – 40 degrees S. *Proceeding UN conference. New Sources of Energy*.
- Parisi, A. V., Sabburg, J., Turner, J., & Dunn, P. K. (2007). *Cloud observations for the statistical evaluation of the UV index at Toowoomba, Australia*. Toowoomba: Faculty of Sciences, University of Southern Queensland.
- Paulescu, M., Paulescu, E., Gravila, P., & Badescu, V. (2013). Solar radiation measurements. In *Weather modeling and forecasting of PV systems operation* (pp. 17-42). London: Springer-Verlag.
- Peng, Z., Yoo, S., Yu, D., Huang, D., Kalb, P., & Heiser, J. (2014). 3D cloud detection and tracking for solar forecast using multiple sky imagers. *SAC*. Gyeongju.
- Pfister, G., McKenzie, R. L., Liley, J. B., Thomas, A., Forgan, B. W., & Long, C. N. (2003). Cloud coverage based on all-sky imaging and its impact on surface solar radiation. *Journal of applied Meteorology*, 42, 1421-1434.
- Pidwirny, M. (2006). *Fundamentals of Physical Geography* (2nd ed.).

- Remote sensing: Fundamental concepts+*. (n.d.). Retrieved June 09, 2016, from <http://remote-sensing.net/concepts.html>
- Renaud, A., Staehelin, J., Fröhlich, C., Philipona, R., & Heimo, A. (2000). Influence of snow and clouds on erythemal UV radiation: Analysis of Swiss measurements and comparison with models. *Geophysics*, *105*, 4961-4969.
- Rudd, T. R. (2011). *Benefits of near-term cloud location forecasting for large solar PV. (Master's thesis)*. Master's thesis.
- Sabburg, J. M., & Long, C. N. (2004). Improved sky imaging for studies of enhanced UV irradiance. *Atmospheric Chemistry and Physics*, *4*, 2543-2552.
- Sabburg, J., & Wong, J. (2000a). The effects of clouds on enhancing UVB irradiance at the Earth's surface: A one year study. *Geophysics*, *27*(20), 3337-3340.
- Sabburg, J., & Wong, J. (2000b). Evaluation of sky/cloud formula for estimating UV-B irradiance under cloudy skies. *Geophysics*, *105*(24), 29,685-29,691.
- Sahin, A. D., & Sen, Z. (2008). Solar irradiance estimation methods from sunshine and cloud cover data. In V. Badescu (Ed.), *Modelling solar radiation at the earth surface*. (pp. 145-173). Berlin: Springer.
- Schafer, J. S., Saxena, V. K., Wenny, B. N., Barnard, W., & DeLuisi, J. J. (1996). Observed influences of clouds on ultraviolet-B radiation. *Geophysics*, *23*(19), 2625–2628.
- Scharmer, K., & Greif, J. (2000). *The European solar radiation atlas*. (Vol. 1). Paris: Les Presses de l'École des Mines.
- Schwander, H., Koepke, P., Kaifel, A., & Seckmeyer, G. (2002). Modification of spectral UV irradiance by clouds. *Geophysics*, *107*(16), 4296.
- Sebag, J., Krabbendam, V. L., Claver, C. F., Andrew, J., Barr, J. D., & Klebe, D. (2008). LSST IR camera for cloud monitoring and observation planning. Ground-based and Airborne Telescopes II. *Proceedings of the International Society of Photonics and Optics.*, 7012.

- Seckmeyer, G., Erb, R., & Albold, A. (1996). Transmittance of a cloud is wavelength-dependent in the UV range. *Geophysics*, 23(20), 2753-2755.
- Shields, J. E., Johnson, R. W., & Koehler, T. L. (1993). Automated whole sky imaging systems for cloud field assessment. *Fourth Symposium on Global Change Studies*.
- Shields, J. E., Karr, M. E., Burden, A. R., Mikuls, V. W., Streeter, J. R., Johnson, R. W., et al. (2010). *Scientific report on whole sky imager characterization of sky obscuration by clouds for the starfire optical range*. Marine Physical Laboratory, Scripps Institution of Oceanography, University of California San Diego.
- Shields, J., Karr, M., Burden, A., Johnson, R., Mikuls, V., Streeter, J., et al. (2009). *Research toward multi-site characterization of sky obscuration by clouds*. Marine Physical Laboratory, Scripps Institution of Oceanography, University of California San Diego.
- Silva, A. A., & Echer, M. P. (2013). Ground-based measurements of local cloud cover. *Meteorology Atmospheric Physics*, 120, 201-212.
- Slater, D. W., Long, C. N., & Tooman, T. P. (2001). Total sky imager/whole sky imager cloud fraction comparison. *Eleventh ARM Science Team Meeting Proceedings*. Atlanta.
- solargis*. (n.d.). Retrieved November 27, 2014, from <http://solargis.info/doc/solar-radiation-maps>
- Souza-Echer, M., Pereira, E. B., Bins, L., & Andrade, M. (2006). A simple method for the assessment of the cloud cover state in high-latitude regions by a ground-based digital camera. *Atmospheric Ocean technology*, 23, 437-447.
- Staiger, H., den Outer, P. N., Bais, A. F., Feister, U., Johnsen, B., & Vuilleumier, L. (2008). Hourly resolved cloud modification factors in the ultraviolet. *Atmospheric Chemistry and Physics*, 8, 2493–2508.
- The Great Soviet Encyclopedia*. (1970-1979). Retrieved August 01, 2016, from <http://www.encyclopedia2.thefreedictionary.com/Pyrheliometer>

- Tooman, T. P. (2003). *Whole sky imager retrieval guide*. Atmospheric Radiation Measurement Program Tech.
- Tovar-Prescador, J. (2008). Modelling the statistical properties of solar radiation and proposal of a technique based on Boltzmann statistics. In V. Badescu (Ed.), *Modelling Solar Radiation at the Earth Surface*. (pp. 55-91). Berlin: Springer.
- Tsubo, M., & Walker, S. (2003). Relationships between diffuse and global solar radiation in southern Africa. *South African Journal of Science*, 360-362.
- Turner, W. D., & Mujahid, A. (1984). The estimation of hourly global solar radiation using a cloud cover model developed at Blytheville, Arkansas. *Journal of Climate and Applied Meteorology*, 23(1), 781-786.
- Vignola, F., Michalsky, J., & Stoffel, T. (2012). *Solar and infrared radiation measurements*. (A. Ghassemi, Ed.) Boca Raton: CRC Press.
- Weihs, P., Webb, A. R., Hutchinson, S. J., & Middleton, G. W. (2000). Measurements of the diffuse UV sky irradiance during broken cloud conditions. *Geophysics*, 105, 4937-4944.
- Wong, L. T., & Chow, W. K. (2001). Solar radiation model. *Applied Energy*, 69, 191-224.
- Yankee Environmental Systems*. (n.d.). Retrieved September 01, 2014, from <http://www.yesinc.com/products/data/tsi440/>

# Appendix A

## Nomenclature

Table A.1: Nomenclature

$A_\lambda$	Absorptivity
$\bar{c}$	Cloud cover percentage
$\bar{C}$	long-term monthly average of daily cloud cover
$\bar{c}$	cloudiness index
$\bar{\bar{C}}$	
$\delta$	declination angle
$G_{sc}$	solar constant
$H$	actual amount of radiation available at the ground
$\bar{H}_m$	measured monthly mean daily global radiation
$H_o$	extraterrestrial radiation
$\bar{H}_0$	monthly mean extraterrestrial solar radiation on horizontal surface
$I$	total global horizontal radiation
$I_b$	hourly beam irradiance on a horizontal surface
$I_{clear}$	clear-sky irradiance
$I_d$	hourly diffuse irradiance on a horizontal surface
$I_{o,h}$	horizontal extraterrestrial radiation
$I_o$	hourly extraterrestrial irradiance
$I_t$	hourly global solar irradiance on a horizontal surface
$k_b$	atmospheric transmittance for beam radiation
$k_d$	diffuse fraction
$k_D$	atmospheric diffuse coefficient
$k_t$	clearness index
$\phi$	latitude of the station
R	relative humidity
$R_\lambda$	monochromatic reflectivity
$t$	time in decimal hours on the 24 hour clock
$T_\lambda$	transmissivity (spectral transmittance)
$\bar{T}_m$	the maximum temperature
$W_s$	sunset hour angle for typical day n of each month in degrees
$z$	solar zenith angle

## Appendix B

# SAURAN Station Details: KZH University of KwaZulu-Natal, Howard College Campus, Durban, South Africa

The SAURAN KZH station is located on the Howard College campus of the University of KwaZulu-Natal, in Durban, South Africa. The instruments are positioned on the roof of the Desmond Clarence science building with very good solar exposure. The eastern, northern and southern horizons are largely unobscured while the low western horizon is partially obscured by a stairwell parapet and telecommunications antenna. The station was first commissioned in 2009 with Eppley radiometers. In April 2012 it underwent a refurbishment with the addition of new Kipp and Zonen instruments and an automated SOLYS tracker.

SAURAN station code: KZH		University of KwaZulu-Natal, Howard College Campus, Durban, South Africa		Latitude: -29.87098° (E) Longitude: 30.97695° (S) Elevation: 150 m AMSL	
Database notation:	Measurement:	Instrument:	Serial number:	Last calibration:	Sensitivity factor:
GHI_CMP11	Global horizontal irradiance in [W/m <sup>2</sup> ]	Kipp & Zonen CMP11 unshaded	126312	11 Jan 2012	10.34 μV/W/m <sup>2</sup>
GHI_SPN1		Global horizontal irradiance in [W/m <sup>2</sup> ]		Thermopile Delta-T SPN1 pyranometer	
DNI_CHP1	Direct normal	Kipp &	120791	30 Jan 2012	8.50

	irradiance in [W/m <sup>2</sup> ]	Zonen CHP1 on a SOLYS tracker			μV/W/m <sup>2</sup>
DHI_CMP11	Diffuse horizontal irradiance in [W/m <sup>2</sup> ]	Kipp & Zonen CMP11 under a shading ball on a SOLYS tracker	126311	11 Jan 2012	9.23 μV/W/m <sup>2</sup>
DHI_SPN1	Diffuse horizontal irradiance in [W/m <sup>2</sup> ]		Thermopile Delta-T SPN1 pyranometer		
UV_CUV5	Total ultra violet radiation in [W/m <sup>2</sup> ] in the wavelength range of 299 to 384 nm	Kipp & Zonen CUV5 radiometer	110204	24 Nov 2011	318 μV/W/m <sup>2</sup>
PB_PSP	Global horizontal irradiance and Diffuse horizontal irradiance in [W/m <sup>2</sup> ]	Perforated shadow band with Eppley PSP pyranometer	35663		9.18 μV/W/m <sup>2</sup>
Air_Temp	Air temperature in [°C]	Campbell Scientific CS215 sensor	E9565		
BP	Barometric pressure in [mbar]	Vaisala PTB110 sensor	0.240		
RH	Relative humidity in	Campbell Scientific	E9565		

	[%]	CS215 sensor			
Rain_Tot	Total rainfall in [mm]	Texas sensor	TE525	52479	0.254
WS	Wind speed in [m/s]	R.M.Young sensor	03001	0.75	
WD	Wind direction in [°]	R.M.Young sensor	03001	355	
WD_SD	Standard deviation of the wind direction in [°]	R.M.Young 03001 sensor			
SPN1_Presence	Indication if direct beam exceeds threshold value of 120 W/m <sup>2</sup>	Thermopile Delta-T SPN1 pyranometer			
WS_Max	Maximum wind speed in [m/s]	R.M.Young 03001 sensor			

Figure B.1: KZH station details.

# Appendix C

## Matlab code for averaging

```
N = t;
tail = mod(numel(A), N);
A_avg = mean(reshape(A(1:numel(A) - tail), N, []));
A_avg(end + 1) = mean(A(end - tail + 1:end));
A_avg = A_avg';
tail = mod(numel(B), N);
B_avg = mean(reshape(B(1:numel(B) - tail), N, []));
B_avg(end + 1) = mean(B(end - tail + 1:end));
B_avg = B_avg';
tail = mod(numel(C), N);
C_avg = mean(reshape(C(1:numel(C) - tail), N, []));
C_avg(end + 1) = mean(C(end - tail + 1:end));
C_avg = C_avg';
tail = mod(numel(D), N);
D_avg = mean(reshape(D(1:numel(D) - tail), N, []));
D_avg(end + 1) = mean(D(end - tail + 1:end));
D_avg = D_avg';
tail = mod(numel(E), N);
E_avg = mean(reshape(E(1:numel(E) - tail), N, []));
E_avg(end + 1) = mean(E(end - tail + 1:end));
E_avg = E_avg';
tail = mod(numel(F), N);
F_avg = mean(reshape(F(1:numel(F) - tail), N, []));
F_avg(end + 1) = mean(F(end - tail + 1:end));
F_avg = F_avg';
Y= [A_avg';B_avg';C_avg';D_avg';E_avg';F_avg'];
Y=Y';
```

%  $A = GHI/GHI_o$ ,  $B = GHI/GHI_c$ ,  $C = DNI/DNI_o$ ,  $D = DNI/DNI_c$ ,  $E = DHI/DHI_c$ ,  $F = DHI/GHI$   
and Y is the vector output of all the variables and t is the time average point.

# Appendix D

## Additional figures not used in the main text

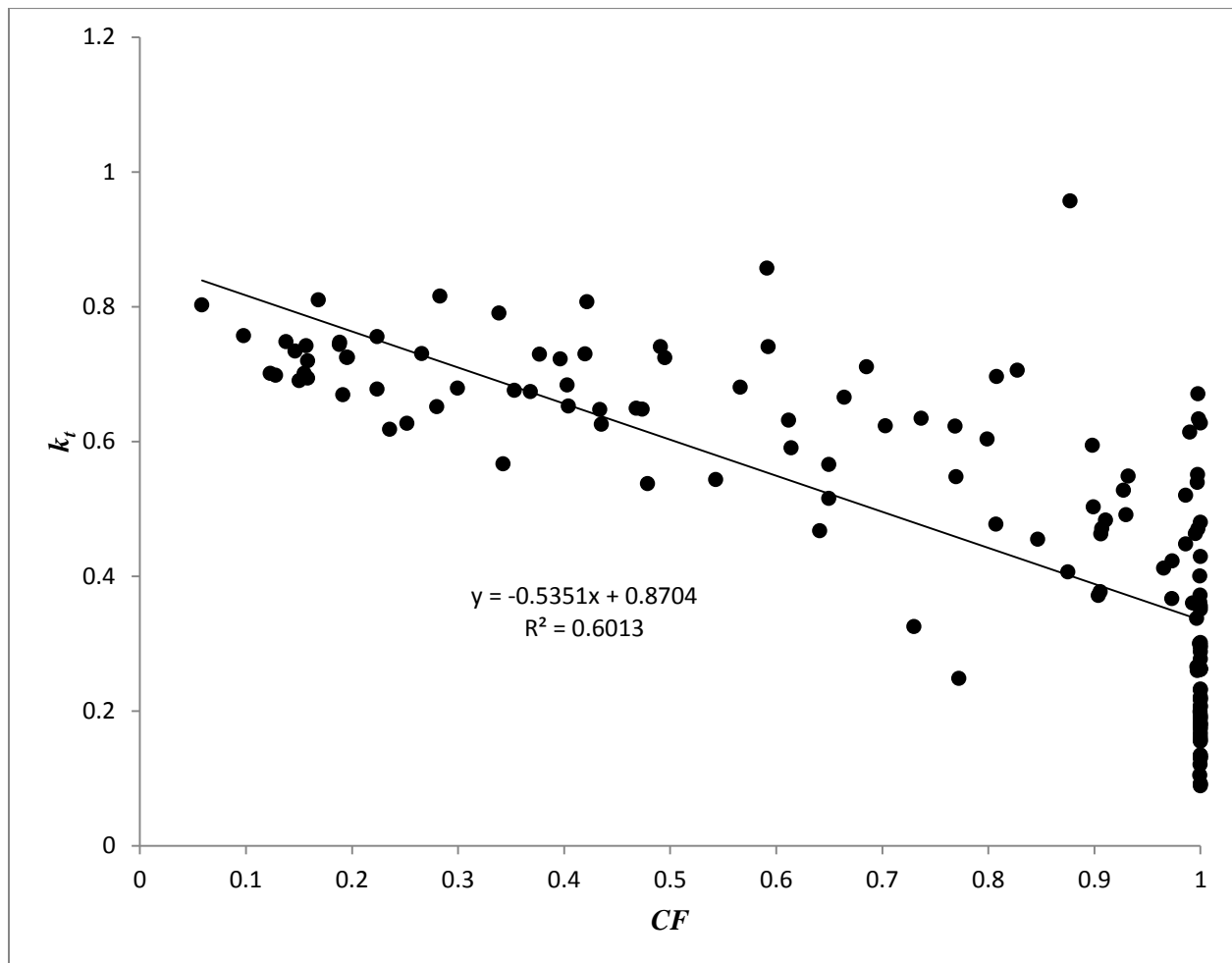


Figure D.1: Scatter plot of  $k_t$  function of the total  $CF$  for the entire dataset for 30 minutes average.

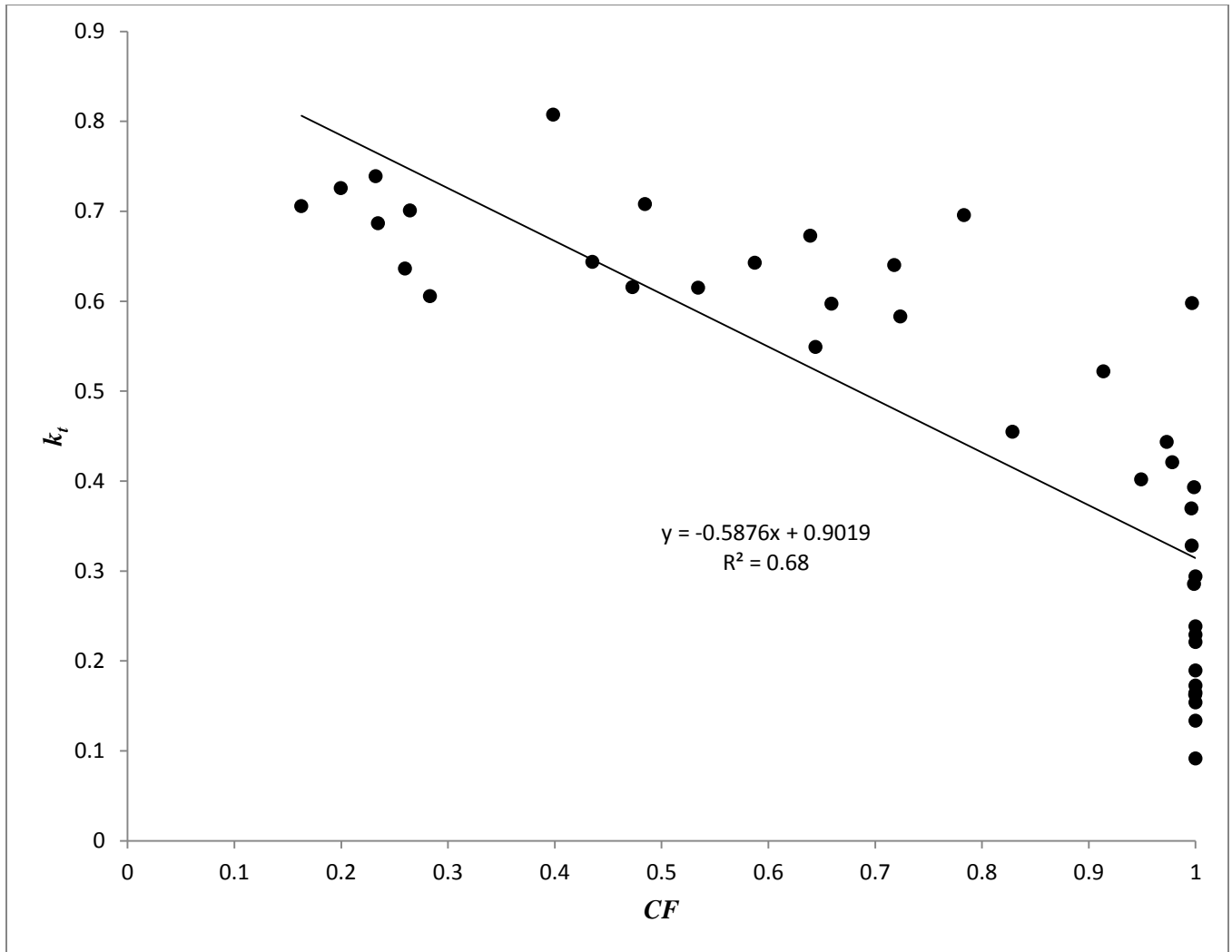


Figure D.2: Scatter plot of  $k_t$  function of the total  $CF$  for the entire dataset for 2 hours average.

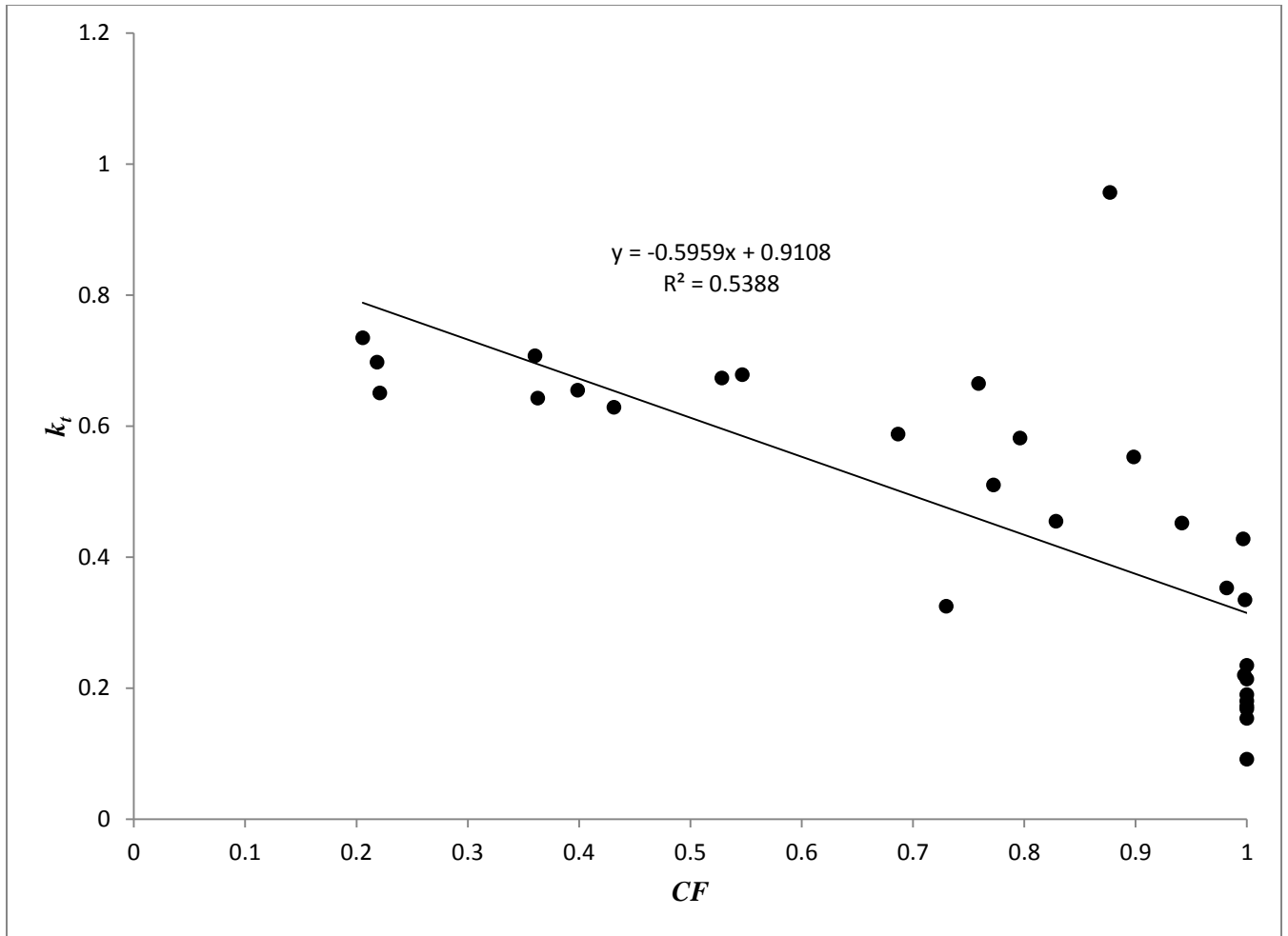


Figure D.3: Scatter plot of  $k_t$  function of the total  $CF$  for the entire dataset for 3 hours average.